الجمهورية الجزائرية الديمقراطية الشعبية
People's Democratic Republic of Algeria
وزارة التعليم العالي والبحث العلمي
Ministry of Higher Education and Scientific Research

جامعة زيان عاشور بالجلفة
Ziane Achour University of Djelfa

كلية العلوم و التكنولوجيا
Faculty of Science and Technology

Department: Mechanical Engineering

Order N° : 009/2024

Defense authorization N° 087/2024

DOCTORAL THESIS

3rd Cycle Doctoral (D-LMD)

Presented by

Siham HAMMID

With a view to obtaining the doctoral diploma in 3rd Cycle Doctoral (D-LMD)

Branch: Mechanical

Specialty: Energetic

Topic

Advanced Thermal Lattice Boltzmann Modelling of Rarefied Flows: Enhancing Microchannel Efficiency with Obstacles and Nanofluids

---

Supported, on 12/06 / 2024, before the jury composed of:

Last and first name	Grade	Institution of affiliation	Designation
Mr Abdelkader ROUIBAH	MCA	University of Djelfa	President
Mr Khatir NAIMA	Professeur	University Center of Naama	Supervisor
Mr Cheikh KEZRANE	Professeur	University of Djelfa	Co-Supervisor
Mr Yahia LASBAT	Professeur	University of Djelfa	Examiner
Mr Noureddine KAID	MCA	University Center of Naama	Examiner
Mr Taibi HADI	MCA	University of Djelfa	Examiner

Djelfa University, FST - 2024

Acknowledgements

First and foremost, I express my sincerest gratitude to Allah, the source of strength and fortitude whose divine blessings have enabled me to undertake this endeavor successfully.

I extend my deepest appreciation to my esteemed supervisor, Pr. NAIMA Khatir, whose invaluable guidance, unwavering support, and meticulous assistance have been instrumental in shaping my research trajectory and the course of my broader academic journey.

Furthermore, I gratefully seize this opportunity to extend my utmost appreciation and sincere gratitude to Pr KEZRANE Cheikh for his invaluable assistance and unwavering support. His guidance and backing have been of immense significance throughout this undertaking.

We also extend our highest expressions of thanks and greetings of appreciation and respect to Pr.Abdelkrim LIAZID for his tireless efforts and consistent support, which played an effective role in shaping the course of our research. His invaluable guidance has been an essential pillar of our journey. We are truly fortunate to have had such a dedicated mentor like him by our side.

I would also like to extend my gratitude to the esteemed Dr.Younes Menni, Dr.Mezali Farouk, and professors in the field of mechanical engineering, whose profound knowledge and expertise have significantly contributed to my growth and development as a scholar.

I wish to express my profound gratitude to the jury for their willingness to review and evaluate this thesis. I genuinely appreciate each member for dedicating their valuable time to assess and provide feedback on this research work.

Moreover, I would like to sincerely acknowledge and appreciate all those individuals who have contributed to the progress and achievement of this work. Their valuable inputs, whether ideas, resources, or support, have played a pivotal role in bringing work to fruition.

Dedication

I humbly dedicate this work to my esteemed parents, beloved brothers, sisters,

And all whose unwavering support has guided me throughout the arduous journey of this work.

Furthermore, I extend my heartfelt dedication to the individuals who have served as a wellspring of motivation by illuminating the path toward completion with profound gratitude.

Thanks!

Siham HAMMID.

Abstract

The Thermal lattice Boltzmann method with a double distribution function is used to study rarefied fluid flow and heat transfer in microchannels. The first part of the thesis studies obstacles inside the microchannel to understand their presence and impact on fluid flow characteristics and overall channel performance. Then, in the second part, the location of obstacles inside the microchannel walls is examined in more detail. This section aims to identify optimal locations for these obstacles. The third part of the study explores the enhancement of the thermophysical properties of the fluid in a microchannel by introducing a nanofluid composed of water mixed with copper nanoparticles. Slip velocity and temperature jump are taken into account in the microchannel and obstacle walls. The study explored the influence of obstacles and nanofluid application on temperature, velocity profiles, Nusselt number and skin friction coefficients, as well as slip velocity and temperature jump along the microchannel walls. In particular, the study highlighted the significant impact of the rarefaction effect on velocity and temperature distribution. The results indicate that a microchannel configuration incorporating nine obstacles led to a deceleration and subsequent flow acceleration at the main outlet. Our study indicates that placing obstacles at the top or along the sides of a rectangular microchannel can effectively reduce outlet temperatures, depending on whether cooling is required on both sides or only at the top, which also helps reduce material consumption.

Key words: *Rarefied Flow, LBM, microchannel, Knudsen number.*

Résumé

La méthode thermique de Boltzmann sur réseau avec une double fonction de distribution est utilisée pour étudier l'écoulement des fluides raréfiés et le transfert de chaleur dans les microcanaux. La première partie de la thèse étudie les obstacles à l'intérieur du microcanal afin de comprendre leur présence et leur impact sur les caractéristiques de l'écoulement des fluides et les performances globales du canal. Ensuite, dans la deuxième partie, l'emplacement des obstacles à l'intérieur des parois du microcanal est examiné plus en détail. Cette section vise à identifier les emplacements optimaux de ces obstacles. La troisième partie de l'étude explore l'amélioration des propriétés thermophysiques du fluide dans un microcanal en introduisant un nanofluide composé d'eau mélangée à des nanoparticules de cuivre. La vitesse de glissement et le saut de température sont pris en compte dans le microcanal et les parois des obstacles. L'étude a exploré l'influence des obstacles et de l'application de nanofluides sur la température, les profils de vitesse, le nombre de Nusselt et de coefficient de frottement , ainsi que la vitesse de glissement et le saut de température le long des parois du microcanal. L'étude a notamment mis en évidence l'impact significatif de l'effet de raréfaction sur la distribution de la vitesse et de la température. Les résultats indiquent qu'une configuration de microcanal incorporant neuf obstacles a conduit à une décélération et à une accélération subséquente du flux à la sortie principale. Notre étude indique que le fait de placer des obstacles au sommet ou sur les côtés d'un microcanal rectangulaire peut réduire efficacement les températures de sortie, selon que le refroidissement est requis des deux côtés ou uniquement au sommet, ce qui contribue également à réduire la consommation de matériaux.
Mots clés : *Ecoulement raréfié, LBM, microcanal, Nombre de Knudsen.*

ملخص

يتم استخدام الطريقة الحرارية لشبكة بولتزمان مع وظيفة التوزيع المزدوجة لدراسة تدفق السوائل المتخلخلة وانتقال الحرارة في القنوات الدقيقة. يدرس الجزء الأول من الأطروحة العوائق الموجودة داخل القناة الدقيقة لفهم وجودها وتأثيرها على خصائص تدفق السوائل والأداء العام للقناة. ثم، في الجزء الثاني، يتم فحص موقع العوائق داخل جدران القنوات الدقيقة بمزيد من التفصيل. ويهدف هذا القسم إلى تحديد المواقع الأمثل لهذه العوائق. يستكشف الجزء الثالث من الدراسة تعزيز الخواص الفيزيائية الحرارية للسائل في قناة صغيرة عن طريق إدخال سائل نانوي يتكون من الماء الممزوج بجزيئات النحاس النانوية. يتم أخذ سرعة الانزلاق والقفز في درجة الحرارة في الاعتبار في الجدران الدقيقة والعوائق. استكشفت الدراسة تأثير العوائق وتطبيق الموائع النانوية على درجة الحرارة، وملامح السرعة، ومعاملات نسلت ومعامل الاحتكاك، بالإضافة إلى سرعة الانزلاق وقفز درجة الحرارة على طول جدران القنوات الدقيقة. وعلى وجه الخصوص، سلطت الدراسة الضوء على التأثير الكبير لتأثير التخلخل على السرعة وتوزيع درجة الحرارة. تشير النتائج إلى أن تكوين القناة الدقيقة الذي يشتمل على تسع عوائق أدى إلى تباطؤ التدفق ثم تسارعه عند المخرج الرئيسي. تشير دراستنا إلى أن وضع العوائق في الجزء العلوي أو على طول جوانب قناة صغيرة مستطيلة يمكن أن يقلل بشكل فعال من درجات حرارة المخرج، اعتمادا على ما إذا كان التبريد مطلوبا على كلا الجانبين أو في الجزء العلوي فقط، مما يساعد أيضاً في تقليل استهلاك المواد.

كلمات مفتاحية: التدفق النادر، طريقة بولتزمان، القناة الصغيرة، رقم كنودسن.

Contents

A Appendix A

List of Figures

List of Tables

List of Abbreviations

Symbols Latin Letters

f Density momentum distribution function

g The internal energy distribution function

T_{in} Inlet temperature, K

T_w Wall temperature, K

u_{in} Inlet velocity

H Non-dimensional height of microchannel

L Non-dimensional length of microchannel

P Pressure

C_{jump} Temperature jump coefficient

T_{bulk} Bulk temperature

K Thermal conductivity $(\text{W}/\text{m} \cdot \text{K})$

r Position (m)

c Velocity (m/s)

A_1, A_2 Slip coefficients

Kn Knudsen number

Re Reynolds number

Pr Prandtl number

Nu Nusselt number

Ma Mach number

C_f Skin friction coefficient

B Non-dimensional parameter

l Non-dimensional length

a Acceleration

F External force

k_{nf} Nanofluid thermal conductivity

Greek Symbols (Letters)

Ω Collision operator

ε Internal energy

ρ Density ($\mathrm{kg/m^3}$)

τ_f Relaxation time for velocity

τ_g Relaxation time for temperature

v Kinematic viscosity

α Thermal diffusivity ($\mathrm{m^2/s^-1}$)

μ Viscosity ($\mathrm{kg/(m^-1 \cdot s^-1)}$)

ω Weight factor

γ Specific heat ratio

σ Tangential-momentum-accommodation coefficient

φ Nanoparticle volume fraction

μ_{nf} Nanofluid dynamic viscosity

Super and Subscript

i Lattice direction

eq Equilibrium

x Position

t Time

in Inlet

n Outlet

w Wall

bf Base fluid

s Solid nanofluid

nf Nanofluid

φ Nanoparticle volume fraction

Abbreviations

LBM Lattice Boltzmann method

LBE Lattice Boltzmann equation

LB Lattice Boltzmann

LGA Lattice Gas Automata

TLBM Thermal lattice Boltzmann method

DDF Double-population distribution function

TLBE Thermal lattice Boltzmann equation

MEMS Microelectromechanical systems

MC Microchannel

MC's Microchannels

2D Two-dimensional

CFD Computational Fluid Dynamics

MD Molecular dynamics

DSMC Direct Simulation Monte-Carlo

BGK Bhatnagar-Gross-Krook

MRT Multi-relaxation time

SRT Single relaxation time

LBGK Lattice Boltzmann BGK

BCs Boundary conditions

Cu-Water Copper water nanofluid

General introduction

Rarefied gas dynamics is a branch of fluid mechanics that aims to derive macroscopic properties from the microscopic behavior of gaseous particles. The rarefied gas behavior characterized by intermolecular collisions and gas-surface interactions. The field examines gas movement in scenarios where the average spacing between successive molecule collisions, known as the mean free path, is significant compared to a characteristic length of the flow structure. Consequently, rarefied gas dynamics relies on statistical concepts and principles typical of gas kinetic theory. A crucial component in various systems, rarefied gas dynamics has gained significant attention due to its potential in technological domains such as aeronautics, astronautics, vacuum-based plasma material processing, micro-electronic etching, chemical industries, heat transfer, and nanotechnology. Recently, its application has extended to micro-electronic mechanical systems (MEMS).

Enhancing channel thermal performance and improving fluid thermal conductivity can be achieved by adding obstacles and using nanofluids instead of conventional liquids. These innovative solutions address heat transfer issues, enhance energy efficiency, and improve heat transmission in thermal systems. Their large specific surface area and strong thermal conductivity make them attractive for engineering applications.

At the microscale, the gas mean free path approaches the typical channel dimension, making rarefaction effects more prominent and requiring consideration. Several physical phenomena neglected at the macroscale significantly impact heat transfer and fluid flow at the microscale. Since the continuum hypothesis is no longer valid, gas flow exhibits non-continuum phenomena such as velocity slip and temperature jump at the channel walls. The slip phenomenon can control the nature of the microchannel geometry due to the rarefaction effect characterized by the Knudsen number.

The Knudsen number is referred to as the ratio $Kn = \lambda/L$. When $kn>$ 0.01, classical descriptions of macroscopic hydrodynamics, such as the Navier-Stokes equations and the Fourier heat conduction equation, lose their significance and are no longer applicable for use. As a result, a trend has emerged to use new techniques such as the whole Boltzmann Equa-

tion (B.E.), and particle-based approaches such as molecular dynamics (M.D.) and Direct Simulation Monte Carlo (DSMC) must be employed for numerical investigations.
Due to its kinetic nature and computational effectiveness, the Lattice Boltzmann Method (LBM) has demonstrated superiority in describing rarefied gas flow. The LBM's kinetic nature sets it apart from other numerical techniques, particularly its suitability for parallel algorithms, simple structure, and ease of handling complex boundary conditions. The LBM approach can address complex and irregular forms and efficient numerical simulations. Additionally, its performance is higher than conventional CFD approaches on microscales. The LBM has been applied to various fluid flow issues and engineering problems, including complex flows, turbulent flows, microflows, seepage flow, magnetic fluid dynamics, combustion, heat transfer, and microfluidics. It accurately captures microscopic interactions and is a promising technique for simulating microflows based on mesoscale features.

This thesis aims to apply the thermal lattice Boltzmann method (TLBM) with a double distribution function to simulate rarefied fluid flow and heat transfer in a microchannel, both with and without obstacles and with nanofluid. To achieve this, a calculation program developed in Python incorporates selected boundary conditions, considering the differences between heat transfer and fluid flow mechanisms from the microscale to the macroscale, characterized by the rarefied effect defined by Knudsen numbers. The study examines fluid flow across a diverse range of Knudsen numbers. The study is divided into three main sections, each addressing different aspects of microchannel analysis. The first part focuses on the presence and impact of obstacles within the microchannel, aiming to understand how obstacles affect fluid flow characteristics and channel performance. The second part examines the precise placement of baffles within microchannel walls, aiming to determine the optimal locations for these obstacles and their influence on fluid flow and channel performance. The third section concentrates on enhancing the thermophysical properties of the fluid within the microchannel by introducing nanofluids to improve the thermal conductivity coefficient, thereby enhancing heat transfer capabilities without modifying the channel's geometric structure.
The thesis is organized into three chapters. Chapter 1 discusses Micro-Electro-Mechanical Systems and heat transfer in microchannels, exploring methods to enhance heat transfer and classifying rarefied flow based on Knudsen numbers. Additionally, the chapter covers the theory and history of the lattice Boltzmann method for simulating flows, addressing the fundamental theory and governing equations. The chapter introduces the simulation workflow

that connects rarefied flow and microchannels using the Thermal Lattice Boltzmann Model, focusing on heat transfer simulation in rarefied flows and highlighting numerical methods and analysis techniques. It emphasizes TLBM models, particularly the DDF model. It provides a comprehensive analysis of boundary conditions, specifically, slip and temperature jump boundary conditions, which are crucial for understanding the simulation process and its relevance in studying rarefied flow and heat transfer phenomena in microchannels. It concludes with a literature review summarizing critical studies and previous research, providing valuable knowledge for future investigations. Chapter 2 delves into the thermal lattice Boltzmann method, thoroughly explaining all the boundary conditions selected for the current study, outlining the algorithm formulation, and detailing the numerical implementation of necessary boundary conditions for simulating forced convection in the microchannel. Chapter 3 presents the study results and includes a discussion section for all research sections. The thesis concludes with an overview of potential areas for future research and offers insights and recommendations for further exploration in the field.

Chapter 1

General overview of rarefied flow

Microfluidic devices offer numerous advantages such as high separation efficiency, minimized reagent usage, and lower power consumption costs [48]. Microchannels, a critical element of these devices, serve various functions including the separation of physical particles, integration into infrared detectors, inkjet print heads, compact gas chromatographs, diode lasers, aerospace technologies, and cooling systems for computer chips [12]. One of the common uses for microchannels is used as a heat sink. Notably, microchannels are frequently employed as heat sinks. Their use in cooling systems has garnered increasing attention in recent research [24, 49].

Microchannels are widely utilized for their excellent properties: higher heat transfer performance, volume per heat load, and smaller geometrical dimensions. Moreover, they necessitate less coolant and cheaper operational costs[11].

As Micro-Electro-Mechanical Systems (MEMS) devices become smaller, the molecular mean free path becomes comparable in length scale. As a result, the Navier-Stokes equations, which rely on the hypothesis of continuous flow, are no longer applicable. Rarefaction effects become essential at this point, and using flow and heat transfer models based on kinetic theory principles becomes necessary according to microscopic and mesoscopic scales[50]. Molecular Dynamics (MD), Direct Simulation Monte Carlo (DSMC)[51, 52], and LBM[32] are commonly used to simulate rarefied gas movement. The computational effort of MD and DSMC is often substantial since regardless of the Knudsen number's apparent validity, they focus on tracking the mobility and interaction of a significant number of molecular particles in a system. On the other hand, there are a lot of lesser particles that are addressed in the LBM computational field. As a result, the method is computationally more effective[5] due to reduced computational costs[11, 53] and satisfactory results[46]. Understanding the fundamental properties of fluid flow and heat transfer in microchannels are crucial for efficiently optimizing microchannel heat sinks[12].

1.1 Micro-Electro-Mechanical Systems (MEMS)

MEMS refers to micro-electro-mechanical systems scaled down to the micrometer level, combining mechanical and electrical items to accomplish tasks usually performed by superior systems. MEMS devices offer various advantages, particularly given their small size and features like ease of integration, lightweight, small power consumption, and high vibration frequency[54]. The application of microflow technology is increasingly common across various industries, including the cooling of medical devices, electric vehicle batteries, and solar panels. It is essential to cool the parts of both mechanical and electrical systems. Consequently, there is an increasing trend in using MEMS and nano-electromechanical systems (NEMS) for various purposes [54], such as cooling microelectronic devices [55]; this includes applications such as cooling microturbines, supercomputers, and micropumps within intelligent integrated systems. It is essential to remove substantial heat flux from the cross-section of microchannels in integrated circuits like microprocessors[46].

1.1.0.1 Heat transfer in microchannel

To improve heat transfer for cooling electronic devices, Tuckerman and Pease [11, 56, 57] identified the flow and heat transfer properties in microchannel heat sinks for the first time in 1981[58] to address heat accumulation challenges in high-power density devices [56]. Microchannel heat sinks have a substantially greater heat transfer rate than macroscale heat sinks [29]. Its remarkable characteristics include high heat loading per volume and compact size [40, 59], exceptional heat dissipation rate, and low operational costs [60]. Its unprecedented heat transfer rate and large area-to-volume ratio[12, 58, 61] further add to its appeal, along with a significant heat transfer coefficient and a smaller size[40, 62]. Furthermore, its low mass and volume and high convective heat transfer coefficient make it an incredibly versatile and efficient choice for various sectors[12].

Microchannel heat sinks are employed in various industries, notably electronics, refrigeration, chemical, aerospace, and bioengineering[58]. Furthermore, the oil and gas industry uses microchannels to model multiphase flow transmission[47]. Microchannels are an essential component in MEMS[6].

Conduction and convection are the two mechanisms used in microchannels to transfer heat. The heat is first conducted into the heat sink, typically constructed of a material with high thermal conductivity. The heat absorbed was then released by the coolant, generally liquid, through forced convection. As a result, conjugate heat transfer is typically prominent in the MCHS heat transfer analysis [29]. Using roughened surfaces like ribs, grooves, and obstacles to disrupt the fluid flow and create vortices can improve forced convection heat transfer in a channel [63]. Microchannels exhibit superior thermal performance compared to conventional channels due to the reduction in hydrodynamic diameter, which results in an enhanced heat transfer coefficient [49]and helps improve heat transmission performance [61]. Furthermore, microchannels possess favorable thermal efficiency and appropriate dimensions [49]. Due to microchannels' comparatively small hydraulic diameters, most cases are laminar [29, 15], according to heat transfer principles, fluid flow parameters, and microchannel solving techniques. Figure 1.1 represents the various study categories [29].

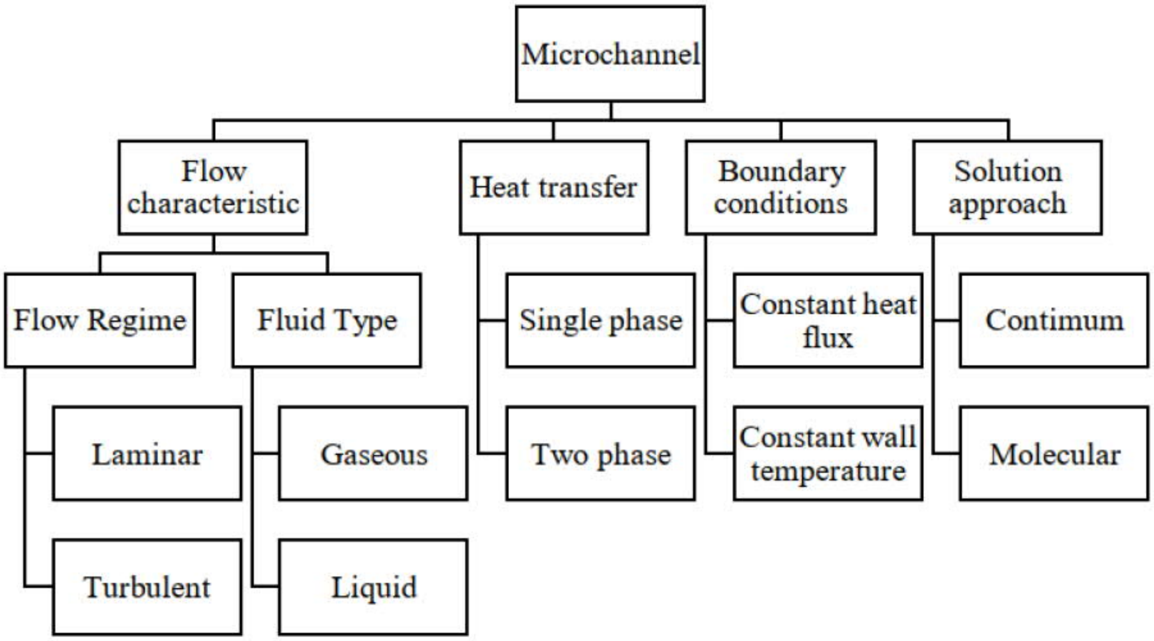

Figure 1.1: The different approaches to the study of microchannels[29]

1.1.1 Microchannel heat transfer enhancement

Convective heat transfer plays a vital role in various heat transfer applications. Enhancing this transfer requires adjustments to both the fluid properties and the surface structure of the heat transfer system. In the following section, we will examine several methods employed to enhance convective heat transfer and improve its effectiveness in microchannels[64].

1.1.1.1 Active method

An external power source is necessary to increase the heat transfer rate in active method. Electrical power or mechanical pumps are two examples of this external input source. Heat transfer has been successfully accelerated using mechanical mixing, surface vibration, fluid vibration, and the inclusion of an external electrostatic or magnetic field that needs an additional energy input[55].

1.1.1.2 Passive method

Passive techniques aimed at enhancing heat transfer encompass a range of methods. These include inducing flow disruption, altering the shape or curvature of the channel, introducing secondary flows, implementing three-dimensional mixing, creating channel roughness, incorporating attachments to increase surface area and promote turbulence, and modifying fluid properties by adding nanoparticles or other fluid additives. Such approaches effectively improve heat transfer without needing external energy input[55].

1.1.2 Nanofluid application in microchannels

The limited thermal conductivity of traditional working fluids like water, ethylene glycol, and oil poses a significant limitation to the thermal efficiency of thermal devices. To overcome this limitation, a revolutionary passive technique involves dispersing metallic nanoparticles, varying in size from 1 to 100 nm, in the base liquids. This dispersion significantly improves the thermal conductivity and enhances the heat transfer performance of the fluids, thereby addressing the thermal conductivity deficiency in thermal devices. Researchers have made significant contributions to exploring the hydrothermal properties of nanofluids in various applications. These nanofluids exhibit remarkable dynamic and thermomechanical characteristics, making them suitable for use in various fields, including microbial fuel cells, thermal storage systems, heat exchangers, biomedical applications, and industrial cooling systems [65].

1.1.3 Classification of rarefied flow in the function of Knudsen numbers

The Knudsen number, established in 1909 to describe the degree of rarefaction [33], is calculated as the molecular mean free path ratio to the characteristic length of the flow [7, 66, 67].

In 1857, Rudolf Clausius introduced the mean free path concept, defined as the average distance a molecule travels between two consecutive collisions in a gas[68] In comparison to gases, liquids have a lower mean free path[7]. The Knudsen number Kn offers fluid flow classification at the micro-scale into four separate categories, each with distinctive characteristics. The categories are continuum flow, which applies to Kn numbers below 0.001; slip flow, which applies to Kn numbers ranged from 0.001 return to 0.1; transition flow, which applies to Kn numbers ranging from 0.01 to 10; and free- molecular flow, which applies to Kn numbers above10[4, 5, 7, 69]. The conventional Navier- Stokes equations are insufficient for non-continuum flows, and certain mesoscopic methods rely on the gas kinetic theory, such as DSMC [4] and LBM, which are necessary for use[70].

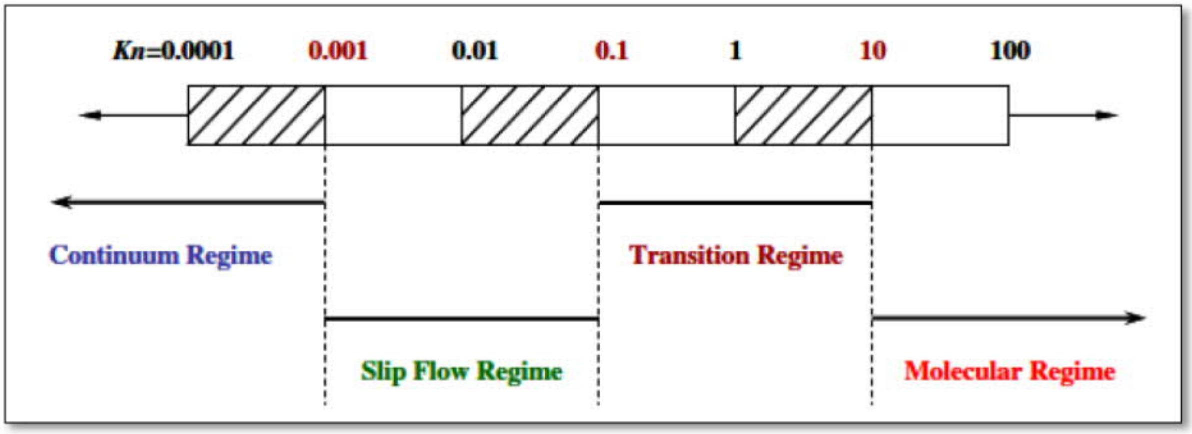

Figure 1.2: Flow regime classification in the function of Knudsen number[74]

According to Knudsen numbers can classify fluid regimes from macroscopic to microscopic fluid, as continuous models based on the Navier-Stokes and Euler equations are generally valid when $Kn < 0,01$ and can be extended to the slip flow regime($0.01 < Kn < 0.1$) by appropriate treatment of boundary conditions. Although, the particle model discrete systems founded on the Boltzmann Equation governs almost all regimes' flow rate ($Kn < 100$) [71, 72].

The slip flow regime is categorized when Kn ranges from 0.001 *to* 0.1. In this range, the continuum hypothesis stands true due to the apparent significance of the rarefaction effect. The Navier-Stokes formulas can achieve the same goal when the slip boundary conditions are applied at the interface between the fluid and solid zones. Furthermore, the slip regime should be used in these cases because the slip boundary strongly influences microflow's flow and thermal behaviors and cannot be neglected [40]. The Navier-Stokes and energy equations and the no-slip boundary condition based on the continuum hypothesis are still valid for liquid flow in MC's and can be employed to predict flow and heat transfer properties with appropriate precision[73].

1.2 Fundamental And Theory of Lattice Boltzmann Method

In computational fluid dynamics, the Navier-Stokes equations are commonly used as the governing equations. However, from the perspective of statistical mechanics, the fluid is understood to be composed of discrete entities like atoms and molecules. The mesoscopic state acts as an intermediary between the macroscopic and microscopic scales, enabling the derivation of macroscopic properties. In this context, employing numerical methods considering discrete particles, such as the Lattice Boltzmann Method (LBM), is essential for accurately describing the fluid.[74].The Lattice Boltzmann Method (LBM) is a computational fluid dynamics technique based on the Boltzmann transport equation and kinetic theory. It is highly efficient for simulating complex physical and chemical phenomena in fluid mechanics. LBM excels in computational effectiveness compared to traditional CFD methods, such as the finite volume method, particularly in handling complex geometries. It has become a valuable and powerful tool in the field of fluid dynamics.

The Boltzmann equation also referred to as the Boltzmann transport equation, offers a statistical representation of the particle distribution within a fluid. It serves as an equation governing the temporal changes of the particle distribution function in the phase space. The phase space encompasses coordinates of states, considering both position and momentum vectors at a specific moment in time. The Boltzmann equation provides a fundamental framework for studying the behavior and dynamics of particles within a fluid system [75].

1.2.1 Historical background

The Lattice Boltzmann Method (LBM) was developed based on the Lattice Gas Automata approach (LGA) [76]. The term 'lattice' in LGA refers to a d-dimensional, regular lattice, while 'gas' denotes the movement of gas particles across the lattice. These particles are typically represented as Boolean values (0 or 1). The dynamics of the gas are governed by a set of rules defined as 'automata.' In the LGA model, space, time, and particle velocities are all discrete [75]. The first LGA model, known as the HPP model, was developed by Hardy, Pomeau, and de Pazzis in 1973 [75]. This model employs a 2D square lattice where gas particles at a node can move to any of the four nearest neighbouring nodes along the lattice lines. The collision model of the HPP follows the "head-on" rule, meaning that if two particles with opposite velocities move to the same node, their speeds rotate 90° after the collision. In all other cases, no collision occurs, and the particle speeds remain invariant[77].

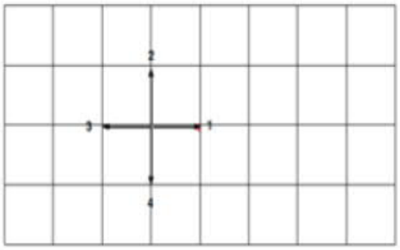

Figure 1.3: The lattice and discrete speed HPP model

The HPP model was created as a microfluid rather than a hydrodynamic flow computational method. However, despite its original purpose, the HPP model's basic concept has provided a valuable additional pathway for flow computations[77]

Frisch, Hasslacher, and Pomeau introduced their hexagonal LGA, now known as the FHP model in 1986, which led to the discovery of the lattice. A triangular lattice is used in this model, and each node has six nearest neighbors[77], as seen in the 1.4a:

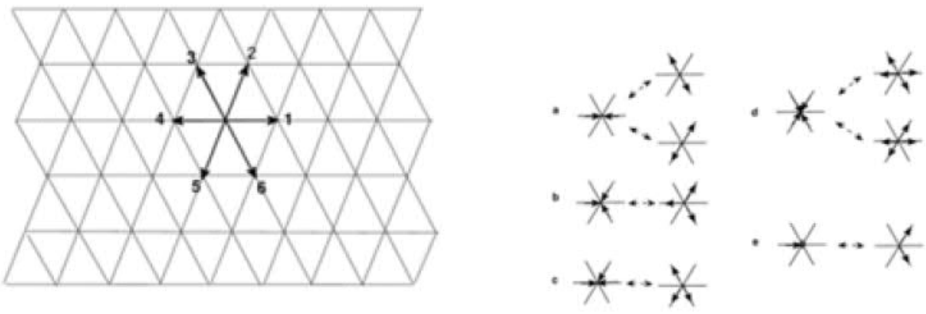

(a) FHP model

(b) collision rule

Figure 1.4: FHP model and collision rule

Implementing an LGA model is simple, and the computation is unconditionally stable and each node's state update is entirely local. The LGA method has limitations, such as statistical noise caused by boolean variables, violation of galilean invariance, and pressure velocity dependence. Historically, these unexpected characteristics prompted the progress of LBM[2]. The LGA is affected by the velocity-dependent pressure does not result in the galilean invariance system of lattice gases, and the density-dependent factor is considered in the nonlinear advection term. LBM converted the boolean variable in LGA to resolve these undesired issues by a single particle distribution function[74, 23]. The statistical noise in LGA was eliminated using a single-particle distribution function. LBM adopted it to replace the boolean variable in LGA and the single-particle distribution function f_i was defined as the particle occupation variable's ensemble average($f_i = n_i$) [74].

The LBE originally arose in a study of the LGA model's hydrodynamic behaviors, founded in 1872 by Austrian scientist Ludwig Boltzmann. In 1988 McNamara and Zanetti were the first to propose employing LBE as a calculation method. The basic idea is to replace the boolean occupation numbers with the associated ensemble averaged population to avoid the statistical noise problem[78]. As a result, it produces smooth macroscopic behaviors by simulating the movement and interaction of ensemble-average particle density distribution function of fluid through the solution of a velocity-discrete Boltzmann equation[79]. The focus is on considering only binary collisions while disregarding collisions involving three or more particles, and molecular chaos in which we deal with a statistical distribution of gaseous particles can be regarded as assumptions. In terms of external forces, there are two types: gravitational forces and inertial forces[1].

1.2.2 Boltzmann Transport Equation

Statistically, the system is determined by the distribution function that can describe at time t as the number of molecules positioned between r and $r + dr$ with velocities between c and $c+dc$. The distribution function f is an essential factor in explaining the action of molecules. And defined as the proportion of molecules in a given container's location with velocities in a specific range at a given time[1]. The Boltzmann equation depends on local movement of particles and collision. Consequently, the equation considers two-particle collisions with hard spherical particle assumptions. The distances between particles interact are very small to free molecular path and proportional to particle diameters. Since intermolecular forces are insignificant in comparison to dynamic forces. Compared to dynamic forces, they are ignored. An external force F causes convection and a change in particle velocity acting on the mass of the gas molecules m [46].

$$f(r + cdt, c + Fdt, t + dt)drdc - f(r, c, t)drdc = \Omega(f)drdcdt \tag{1.1}$$

The collision operator Ω is defined as the rate of change between final and initial state of distribution function [80, 46].

Dividing (1.1) by $dtdrdc$ and taking $dt \to 0$

$$\frac{df}{dt} = \Omega(f) \tag{1.2}$$

The distribution function f is a function of r, c, t the total rate of change and can be developed as follows:

$$df = \frac{\partial f}{\partial r}dr + \frac{\partial f}{\partial c}dc + \frac{\partial f}{\partial t}dt \tag{1.3}$$

The equation (1.3) became by dividing by dt :

$$\begin{aligned}\frac{df}{dt} &= \frac{\partial f}{\partial r}\frac{dr}{\partial t} + \frac{\partial f}{\partial c}\frac{dc}{dt} + \frac{\partial f}{\partial t}\\ \frac{df}{dt} &= \frac{\partial f}{\partial r}c + \frac{\partial f}{dc}a + \frac{\partial f}{\partial t}\end{aligned} \tag{1.4}$$

Where a represent the acceleration and related to the force$F$ by Newton's second law :

$$a = \frac{F}{m} \tag{1.5}$$

The Boltzmann equation can be expressed as below:

$$\frac{\partial f}{\partial t} + c \cdot \frac{\partial f}{\partial r} + \frac{F}{m} \cdot \frac{\partial f}{\partial c} = \Omega \tag{1.6}$$

The Boltzmann Equation can be simplified for a system without an external force as follows:

$$\frac{\partial f}{\partial t} + c.\nabla f = \Omega \tag{1.7}$$

1.2.3 The LBM and its Lattice Models: A Brief Overview

LBM divides the computational domain into lattice nodes [81] linked to nearby lattice nodes by lattice linkages from a central lattice node. Different lattice models are introduced with variable numbers of lattice speeds, denoted by the notationD_nQ_m, where "D" stands for the problem's size and "Q" for the number of lattice links [82]. The following figures display some lattice models:

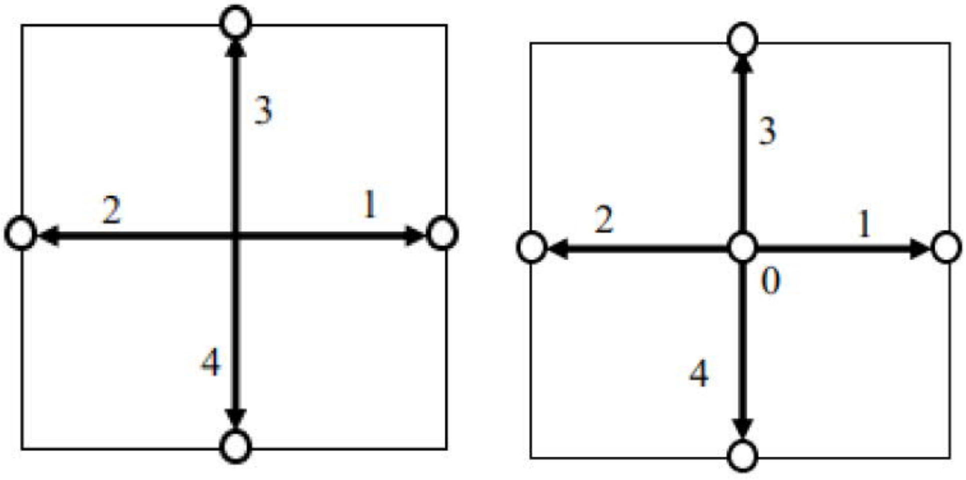

(a) (b)

Figure 1.5: LB model :a) D2Q4 model and b) D2Q5 model [92]

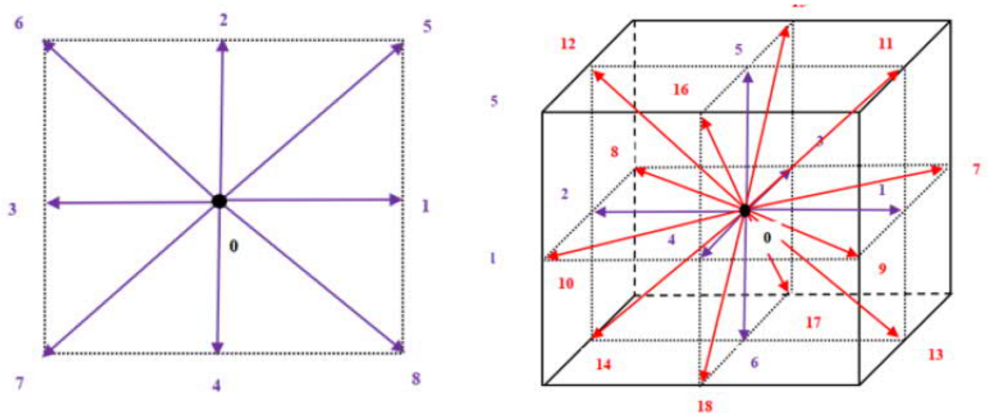

(a)

Figure 1.6: LB model :a) D2Q9 model and b) D3Q19model[94]

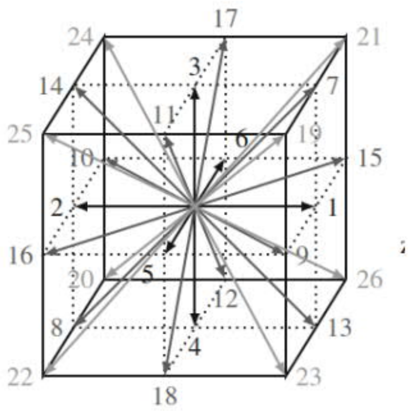

Figure 1.7: LB model: D3Q27 model [93]

1.2.4 The BGK(Bhatnagar-Gross-Krook) approximation

The application of the Boltzmann Equation presented significant challenges due to the highly intricate nature of the collision term. Qian et al. [83] suggested a linearization of the collision operator by using the relaxation parameter introduced in 1954 by Bhatnagar, Gross, and Krook (BGK) as a simplified version of the collision operator. It is viable to approximate the collision operator using a straightforward operator without introducing considerable error into the solution result [84]. They proposed that the change in the velocity distribution function is proportional to its deviation from the local Maxwellian [1]. They showed that the distribution function f is located near to a local equilibrium distribution function f^{eq} and declines in the direction of this equilibrium with a characteristic time τ [85]. Consequently, the given expression replaces the exact collision integral [80]:

$$\Omega = \frac{1}{\tau}\left(f^{eq} - f\right) = \omega\left(f^{eq} - f\right) \tag{1.8}$$

Which Ω called collision frequency[80].

The Boltzmann Equation, in the absence of external forces, can be formulated by employing the BGK approximation as follows:

$$\frac{\partial f}{\partial t} + c \cdot \nabla f = \frac{1}{\tau}\left(f^{eq} - f\right) \tag{1.9}$$

1.2.5 Multiple Relaxation Time collision

The collision operator is represented as a matrix in the LBM evolution equation with the Multiple Relaxation Time (MRT) model. The phase space's distribution function,fi , is decomposed into a moment space of q dimensions. The collision matrix in 1.10 to the $q \times q$ matrix, where q represents the total number of velocities in the set [86].

$$f_i(x + c\Delta t, t + \Delta t) - f_i(x, t) = -\Omega \left[f_i(x, t) - f_i^{eq}(x, t) \right] \tag{1.10}$$

$$f_i(x + c\Delta t, t + \Delta t) - f_i(x, t) = -M^{-1} S \left[m(x, t) - m^{eq}(x, t) \right] \tag{1.11}$$

The $m(x, t)$ and m^{eq} are moments vectors, and S is a diagonal matrix called the relaxation matrix [87].

1.2.6 Equilibrium Distribution Function

James Clerk Maxwell recognized in 1859 that a model accounting for many molecules is challenging to formulate [84]. Maxwell believed that knowing the speed and position of each molecule at every moment was unnecessary [84].

In 1866, James Clerk Maxwell formulated a precise technique based on the so-called transfer equations. According to these equations, he proposed an evolution equation for the distribution, which was accepted. Maxwell introduced and developed the distribution theory, but Boltzmann's contribution cannot be forgotten. The equation is frequently known as the Boltzmann Equation, and it is also known as the Maxwell–Boltzmann equation [1] The Maxwell distribution function can write for particles moving with macroscopic velocity u as [80]:

$$f^{eq} = \frac{\rho}{(2\pi RT)^{D/2}} \exp\left(-\frac{(\vec{c} - \vec{u})^2}{2RT} \right) \tag{1.12}$$

$$= \frac{\rho}{(2\pi RT)^{D/2}} \exp\left(-\frac{\vec{c} \cdot \vec{c} - 2\vec{c} \cdot \vec{u} + \vec{u} \cdot \vec{u}}{2RT} \right) \tag{1.13}$$

$$= \frac{\rho}{(2\pi RT)^{D/2}} \exp\left(-\frac{\vec{c} \cdot \vec{c}}{2RT} \right) \exp\left(-\frac{-2\vec{c} \cdot \vec{u} + \vec{u} \cdot \vec{u}}{2RT} \right), \tag{1.14}$$

where D represent the problem dimension, in the case of two-dimensional problems$D = 2$ With employed a Taylor series, can be expanded the exponential function as:

$$\exp(x) = 1 + x + \frac{x^2}{2!} + \frac{x^3}{3!} + \ldots\ldots \tag{1.15}$$

The equation becomes:

$$f^{eq} = \frac{\rho}{(2\pi RT)^{D/2}} \exp\left(-\frac{\vec{c}\cdot\vec{c}}{2RT}\right)\left(1 - \frac{-2\vec{c}\cdot\vec{u}+\vec{u}\cdot\vec{u}}{2RT} + \frac{(-2\vec{c}\cdot\vec{u}+\vec{u}\cdot\vec{u})^2}{4R^2T^2} + \ldots\ldots..\right). \tag{1.16}$$

Can approximate the equilibrium distribution function by disregarding terms of order $O(u^3)$ and higher:

$$f^{eq} = \frac{\rho}{(2\pi RT)^{D/2}} \exp\left(-\frac{\vec{c}\cdot\vec{c}}{2RT}\right)\left[1 - \frac{-2\vec{c}\cdot\vec{u}+\vec{u}\cdot\vec{u}}{2RT} + \frac{(\vec{c}\cdot\vec{u})^2}{2R^2T^2}\right] \tag{1.17}$$

The known distribution function can be regenerated by applying the following two substitutions:

$$RT = c_s^2 \quad \text{and} \quad W(\vec{c}) = \exp\left(-\frac{\vec{c}\cdot\vec{c}}{2RT}\right)(2\pi RT)^{-D/2} \tag{1.18}$$

$$f^{eq} = \rho W(\vec{c})\left(1 + \frac{2\vec{c}\cdot\vec{u}-\vec{u}\cdot\vec{u}}{2c_s^2} + \frac{(\vec{c}\cdot\vec{u})^2}{2c_s^4}\right) \tag{1.19}$$

The equilibrium distribution function can be discretized in terms of velocity direction as follows [84] :

$$f_i^{eq} = \rho\omega_i\left(1 + \frac{2\vec{c}\cdot\vec{u}-\vec{u}\cdot\vec{u}}{2c_s^2} + \frac{(\vec{c}\cdot\vec{u})^2}{2c_s^4}\right) + o\left(u^2\right)\Big) \tag{1.20}$$

1.2.7 Boltzmann equation discretization

The Boltzmann equation evolution under the McNamara and Zanetti model can be formulated as follows:

$$f_i\left(x + c_i\Delta t, t + \Delta t\right) - f_i(x,t) = \Omega_i(f(x,t)) \tag{1.21}$$

The collision operator in the model is still quite complicated by the non-linearity. Higuera and Jimenez suggested a modified H.J. model in 1989, built on the hypothesis that the collision operator can be estimated linearized by supposing it is near equilibrium [77].

$$f_i = f_i^{eq} + f_i^{neq} \tag{1.22}$$

Where f_i^{neq} is the none equilibrium part

One of the most fundamental and widely used methods in LBM is the LBE with a linearized collision operator based on BGK (LBM-SRT) collision model. When the Mach number is low, it is possible to derive the governing continuity and momentum equations using a Chapman-Enskog analysis [75].

Unlike the Navier-Stokes equations, which have a nonlinear advection term in the macroscopic approach, the LBM replaces it with a linear streaming process. Additionally, both collision and streaming processes are localized in the LBM. The LBM is considered an explicit method, with second-order accuracy in space and time and unconditional linear stability, while the consistency is conditioned to low Mach numbers [78]. The Chapman-Enskog expansion successfully recovers the LBGK model to the Navier-Stokes equation, and as a result, it has been used in numerous fluid research [79]. The kinetic equation for the distribution function through the lattice linkage, the distribution function streams with velocity $c_i = \frac{\Delta x}{\Delta t}$ Can be written the kinetic L.B. equation with the BGK approximation as:

$$f_i(x+\Delta x, t+\Delta t) - f_i(x,t) = -\frac{\Delta t}{\tau}\left[f_i(x,t) - f_i^{eq}(x,t)\right] \tag{1.23}$$

The equation can be simplified to[92]:

$$f_i\left(x+c_i\Delta t, t+\Delta t\right) = f_i(x,t) + \frac{\Delta t}{\tau} f_i^{eq}(x,t) - f_i(x,t) \tag{1.24}$$

The equation (1.23) describes how particle distribution functions change due to collision and streaming. The density distribution function is represented by f and is modeled based on assumptions that the collision involves two particles only, no external force is present, and the velocity of a particle after the collision is unaffected by its velocity before the collision [88].

Most LBE simulations can solve equations in two steps. The particles distribution function for each direction are relaxed toward quasi-equilibrium distributions in the collision step, and then the distributions move to neighbor nodes in the streaming step [89]. The solution domain must discretize into lattices in LBM. The particles stream (move) to the nearby nodes in the specified directions. The lattices' isotropy must be preserved for choosing a weighting factor for each lattice direction [84].

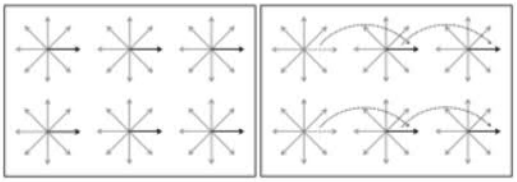

Figure 1.8: Streaming Process[101]

1.2.8 Lattice Boltzmann method Algorithm

Lattice units

In the simulation, it is crucial to transform a system from physical units into non-dimensional or lattice units to make all parameters in lattice units. LBM utilizes particular nondimensional parameters, unlike traditional fluid mechanics [81].

Initialization

The flow needs an initial state at the beginning of the simulation. Although it is a common practice to initialize it in a rest state (zero velocity), the choice of the initial condition can impact the simulation's output.

Collision

The local distribution functions can be utilized to calculate macroscopic moments such as velocity and density at each node. Afterward, a local equilibrium is determined based on these moments, and the distribution functions are subsequently relaxed towards it using either BGK or MRT methods[85]. The collisions step can be discretized [90]:

$$f_i(x, t + \Delta t) = f_i(x, t)[1 - \Omega] + \Omega f_i^{eq}(x, t) \tag{1.25}$$

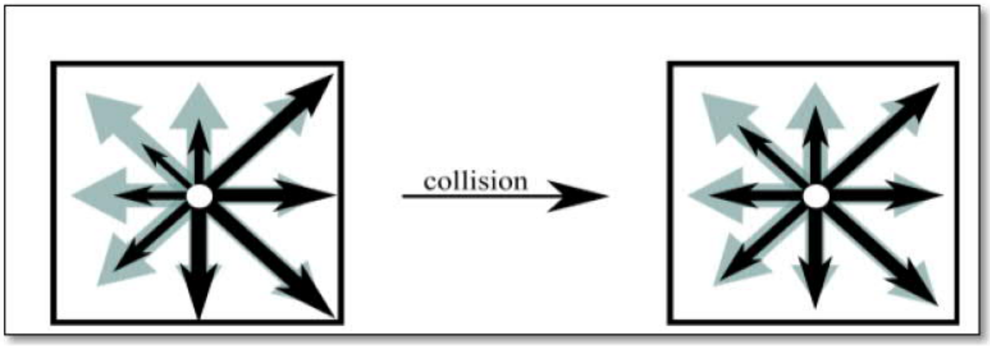

Figure 1.9: The collision for D_2Q_9 case[97]

Streaming

Each lattice link obtains a stream of velocity distribution functions. This operation allows information to be propagated from one node to another. It can be considered the advection term's equivalent in the Navier-Stokes equation [85].

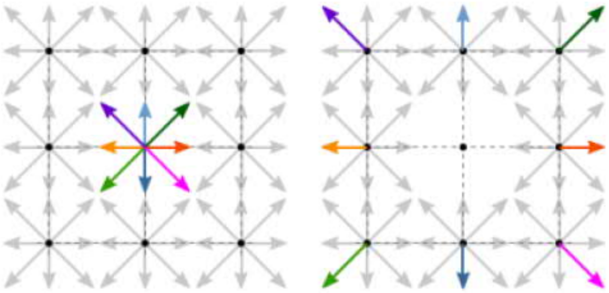

Figure 1.10: streaming process

The streaming step can be discretized as [90]:

$$f_i(x + \Delta x, t + \Delta t) = f_i(x, t + \Delta t) \tag{1.26}$$

Boundary condition

The primary purpose of boundary conditions is to provide an appropriate definition for the distribution functions at the boundaries of the simulation field, considering the various distribution functions that enter or exit the simulation domain. This is essential for determining the macroscopic quantities returned by the simulation [85]

1.3 Rarefied flow and heat transfer

Microelectromechanical systems (MEMS) have attracted growing research attention in recent decades owing to their compact structural characteristics, large heat exchange area per unit volume, high heat exchange efficiency, and low heat transfer driving force[40]. The MEMS devices have found various academic and industrial applications, including micro-engines, micro-sensors, and electronics cooling [50]. Due to its fundamental nature and numerous applications in aerodynamics, nanotechnologies, microelectromechanical systems, heat transfer, and shale gas, studies on rarefied gaseous flow in microchannels have gained significant interest over recent years [5]. The rapid development of micro- and nano-devices over the last decade has further heightened interest in fluid flow and heat transfer [59, 91, 92]. Conventional continuous gas dynamics methods become inapplicable when the density diminishes beyond a certain point. Discrete molecular gas dynamics or rarefied gas dynamics methods are necessary when the mean free path of the gas molecules is significant relative to the characteristic length of the flow [4]. The continuum assumption fails for rarefied gases; thus, The discrete nature of gas molecules is significant and cannot be disregarded. To characterize this rarefaction effect, the Knudsen number, *Kn*, was developed refers to the ratio of the mean free to the characteristic length of flow paths[5].

1.3.1 Simulation of Heat Transfer in Rarefied Flows: Numerical Methods and Analysis

Flow and heat transfer in microdevices differ from flow and heat transmission in macro devices due to the molecules' mean free path near the flow domain's characteristic length[93]. The continuum flow model (Navier Stokes equations) fails, and the Knudsen number is more efficient [7, 93]. By increasing the Knudsen number, the gas would experience more pronounced rarefaction effects, leading to noticeable slip velocity and temperature jumps at the boundaries. A slip flow condition may also arise when dealing with liquid flow in microchannels with hydrophobic surfaces. The concept of slip phenomenon in fluids was initially introduced by Navier, who postulated that a component of the fluid velocity at the surface is directly proportional to the tangential stress, with a proportionality constant referred to as the "slip length" [6]. The M.D and DSMC methods have progressed in microfluidic flow simulation. Still, even so, they are frequently regarded as too computationally expensive for most practical applications [91, 93] cause they are attempting to monitor the movements and interaction of many molecular particles in the system [5]. The methods necessitate exceedingly high storage and computation time requirements [2]. In addition, there are requirements for the use of supercomputers[94].

Unlike MD and DSMC schemes, LBM is more intuitively efficient in computation due its computational cost is comparable to Navier-Stokes solvers, which are only suited for simulation in slip regions even with higher-order slip boundary conditions [91]. The LBM method has been an excellent choice for simulating micro-flow dynamic issues involving microscopic and macroscopic behavior[21, 91, 92]. Due to its kinetic origin, the LBE has been presented as a practical approach for microflow simulations [37, 91, 92, 94]. In addition, the LBM can be considered an explicit method since it does not demand solving simultaneous equations at every time step. Hence, LBM can easily be implemented in parallel computing techniques[95].

1.3.2 Thermal Lattice Boltzmann Model

The thermal lattice Boltzmann method (TLBM) is a computational fluid dynamics approach that has been developed in recent years. It has been extensively applied in various practical fields, including heat transfer, fluid flow, and porous media. Additionally, it has been used to model complex industrial problems, such as fuel cells, which are relevant to related fields [84]. The development of TLBM for thermal transport issues has garnered interest and effort due to the advantages of the LBE. In addition, it can be classified into four distinct groups: passive scalar, multispeed, hybrid, and double-population distribution function (DDF) techniques [42]. The passive-scalar-based TLBE model treats temperature as a passive scalar generated by the velocity field and adheres to the convection-diffusion equation. A primary limitation of this model is that temperature does not affect the flow field; instead, the flow velocity determines the temperature field. In the multispeed approach, only the velocity distribution function is utilised as a straightforward extension of the athermal LBE model, and to reach the macroscopic temperature, additional discrete speeds and higher-order velocity expansion are required to approximate the Maxwell-Boltzmann equilibrium distribution. In the hybrid approach, the advection-diffusion equation for temperature is individually solved using the finite-difference or other traditional numerical methods. In contrast, the mass and momentum conservation equations are evaluated by using the athermal LBE model. Two distribution functions are utilised in the DDF approach; the first is performed as the density distribution function for velocity in the flow field, and the second as the density distribution function for energy in the thermal area[42, 82].

The TLBM uses previously different approaches to simulate conductive and convective heat transfer [74]. The TLBM needs less calculation time than other computational fluid dynamics techniques that are based on the discrete and numerical resolution of the Navier-Stokes equations, such as the finite difference approach, finite volume method, and finite element method [84].

1.3.3 Double Distribution Function(DDF) model

In 1998 He et al. introduced the TLBM with a double-distribution function (DDF) for simulating microflows that involve heat transfer by incorporating an extra internal energy density distribution function. This technique employs kinetic theory to model the temperature field [96]. And they are using two separate distribution functions, one for momentum and the other for energy. The model produced high stability. The relaxation parameters for heat transfer and momentum were also differentiated [97]. Subsequently, the model has been further developed by many others.. As usual, the velocity distribution function describes the macroscopic density and momentum, while an internal energy distribution function governs the changes in the temperature field [98]. One benefit of the DDF approach is that it retains other LBM systems' ease of development and parallelizability. Furthermore, this technique provides flexibility in handling flow and heat fields, allowing for a choice between separate collision operators for each or the same operator to control both [98].

1.3.4 Boundary Conditions in Rarefied Flow: A Comprehensive Analysis

The research on gas flow in microchannels had already demonstrated that the theoretical predictions made using Navier-Stokes equations and the boundary condition of no-slip velocity at the wall underpredicted the experimental mass flow rates. As a result, The Maxwellian slip velocity boundary condition is commonly used [99]. In kinetic theory, gas molecules leave the wall at the Maxwell equilibrium distribution function speed, defined by the equilibrium distribution function (f_i^{eq}) and (g_i^{eq}). However, this behavior differs in the case of rarefied gas flow. The distribution function at the wall is not at equilibrium because the gas molecules do not entirely obey the diffusive reflection rule. As a result, the non-equilibrium part ($f_i - f_i^{eq}$) and ($g_i - g_i^{eq}$) approximated by a first-order extrapolation of the distribution's non-equilibrium function at the neighboring fluid node should add to the expression [91].

Besides the Knudsen raising, the gas's rarefaction increases, leading to slip velocity and temperature jump at the surfaces. Additionally, when microchannels feature hydrophobic surfaces, the liquid flow exhibits a slip flow regime. Navier was the first to propose the slip phenomenon in fluids, stating that the tangential component of fluid velocity at the surface is proportional to the tangential stress, with a proportionality constant referred to as the "slip length." [6]

The slip length in this linear slip model is determined by dividing the slip velocity by the absolute value of the velocity gradient [47].

1.3.5 Slip boundary condition

Navier proposed the slip condition, and Maxwell later developed it; the walls and fluid velocities along the channel wall differ at slip boundary conditions [100]. The physical mechanism of boundary slip differs significantly between liquid and gas flows. The rarefied effect causes the gas flow slip phenomenon. The continuum assumption can refuse with a small Kn for the micro gas flow. The slip phenomenon of liquid flow is induced by roughness and microbubble. The Knudsen numbers are minimal, but the continuum hypothesis can still be confident [37]. In LBM, there are two types of slip boundary conditions. The first approach uses Navier's slip model to construct the slip velocity directly. Tian et al. employed a second-order implicit scheme to calculate the first-order derivative of slip velocity at the boundary [91] , while Zheng et al. coupled the momentum and energy equations with LBM to obtain the slip velocity, thus avoiding the challenge of computing the second-order derivative of slip velocity [5]. Tian et al. and Zheng et al. utilized the nonequilibrium extrapolation scheme for slip boundary conditions, neglecting the numerical slip velocity produced by the velocity boundary conditions [47]. The second type of slip boundary conditions involves treating the unknown distribution functions, where the slip velocity is calculated based on these distribution functions. Nie et al.[94] utilized the bounce-back boundary condition to capture the slip velocity in micro- electromechanical systems. However, He et al. discovered that the slip velocity is generated by the discrete effects of the bounce-back scheme, and alternative schemes would produce a nonzero numerical slip velocity [47].

1.3.5.1 First-order slip boundary condition

Tian developed the Maxwell first-order slip boundary condition. The slip boundary condition is given in non-dimensional form as follows [97]:

$$v_{y=0}^{slip} = v_{x,y=0} - v_{x,w} = \sigma Kn \left(\frac{\partial u}{\partial y}\right)_{y=0} \tag{1.27}$$

$$v_{y=H}^{slip} = v_{x,w} - v_{x,y=H} = \sigma Kn \left(\frac{\partial u}{\partial y}\right)_{y=H} \tag{1.28}$$

σ epresent the tangential-momentum-accommodation coefficient, describes the fluid molecules' interaction with the wall. The coefficients range from nearly zero to unity for specular and diffuse reflections, with their values varying depending on the gas type, solid, surface roughness, gas temperature, gas pressure, etc. Experimental findings have revealed a consistent trend among gas-solid couples frequently utilized in engineering applications, indicating that their accommodation coefficient values are close to unity [8].

1.3.5.2 Second-order slip boundary condition

The second-order slip boundary condition was suggested to describe the higher slip velocity in the rarefied flow to address the shortcomings of Maxwell's first-order slip boundary [5] and is commonly expressed as :

$$u_s = A_1 Kn \frac{\partial u}{\partial n}\bigg|_{\text{wall}} - A_2 Kn \frac{\partial^2 u}{\partial n^2}\bigg|_{\text{wall}} \tag{1.29}$$

A_1 and .A_2 are slip coefficients and $\frac{\partial u}{\partial n}_{\text{wall}}$, $\frac{\partial^2 u}{\partial n^2}_{\text{wall}}$ represent the first and second derivatives of the tangential velocity at the wall in the normal direction [5].

1.3.6 Temperature Jump Boundary Condition

Tian has explained the procedure to establish a boundary condition for temperature jump as [91]:

$$\phi_{y=0}^{jump} = \phi_{y=0} - \phi_w = \alpha \left(\frac{2\gamma}{\gamma+1}\right)\left(\frac{Kn}{\Pr}\right)\left(\frac{\partial\phi}{\partial y}\right)_{y=0} \tag{1.30}$$

$$\phi_{y=H}^{jump} = \phi_w - \phi_{y=H} = \alpha \left(\frac{2\gamma}{\gamma+1}\right)\left(\frac{Kn}{\Pr}\right)\left(\frac{\partial\phi}{\partial y}\right)_{y=H} \tag{1.31}$$

α is the thermal-accommodation coefficient, usually equal to unity, indicating that the wall boundary is a completely diffuse reflection. And γ represents the specific heat ratio [91]. The so-called velocity slip and temperature jump boundary conditions can be considered in the rarefied flow by commonly utilized modeling microfluidics and gas flow in vacuum systems, etc.[1].

1.3.7 Literature review

Numerous studies have been dedicated to investigating fluid flow and heat transfer processes within MC's using LBM. In the subsequent section, we will delve into a comprehensive literature review highlighting relevant studies and previous research conducted in this field. Drawing upon these works, we aim to build upon the existing knowledge and shed light on the advancements made in understanding fluid flow and heat transfer phenomena in MC's using LBM approach.

Karimipour et al. (2015) studied numerically forced convection heat transfer of *water-Ag*, *water-Cu* , and *water-*AL_2O_3 nanofluid in a MC using the TLBM. The results show slip velocity, temperature jump, velocity, and temperature curves; the Nusselt number decreases, and the slip velocity and temperature jump increase as the slip coefficient increases [101].

Yuan and Rahman (2016) utilized an MRT-LB model with a general second-order slip boundary condition to analyze gas flow behavior MC's across a wide range of Kn. The model is very effective in obtaining the flow behavior of rarefied gas withKn up to 10, including the flow rate, velocity profile, and pressure distribution. In addition, findings revealed that the Knudsen layer effect on velocity is important for flow inside the intermediate range of Kn but negligible for continuum flow[5].

Akbari et al. (2016) Studied laminar forced convection heat transfer of *water-*AL_2O_3 nanofluids within a rectangular ribbed MC were investigated by varying Re from 10 to 100. The result shows that raising the heat transfer surface (rib height) and the volumetric percentage of nanoparticles enhances the heat transfer rate. Additionally, decreasing rib height and raising the *Re* both produce a decrease in the average friction factor. The findings also demonstrate that the average *Nusselt* number, friction coefficient, and heat transfer rate of the ribbed MC generally increase with increasing rib heights and nanoparticle volume fractions[14].

Ghadirzadeh et al. (2017) analyzed the laminar forced convection heat transfer of water-alumina nanofluid flow within a circular MC in the slip flow regime with LBM. Uniform velocity and temperature profiles are imposed at the entrance to the micro annulus.The outer wall is heated with a constant heat flux, and the interior wall is insulated. The result shows the augmentation of the slip factor raises slip velocity and takes more significant values close to the flow's entrance zone, where the velocity gradient is greater. Furthermore, it is found that the velocity profile's highest value at fully developed regions. And friction factor was reduced. The volume proportion of nanoparticles enhances the temperature jump and thermal performance, although it has no impact on slip velocity[6].

Zarita et al. (2018) analyzed numerical heat transfer in a MC using *water-Ag* nanofluid by using LBM with the BGK approximation with the first-order velocity slip boundary and temperature jump boundary conditions; it was deduced that velocity slip was unaffected by changes in nanoparticle volume proportions. Although the temperature jump was dominated, the results show that the rising of *Kn* resulted in decreasing *Nu* and skin friction coefficient [67] .

Taassob et al. (2018) studied the inflence of MC sharp variation on hydrodynamic properties and rarefied thermal flow; with exercise sharp bends and curved corners on MC configuration. In addition, the DSMC is used in simulation with pressure-driven boundary conditions. The results showed that implementing curvatures of different radii increases the mass flow rate. Furthermore, by the radius augmentation, the slip velocity rises, and as *Kn* values rise, the wall's temperature jump increases [50].

Kmiotek and Kucaba-Piętal (2018) analyzed fluid flow and heat transfer characteristics of laminar flow in a 2D rectangular MC with slim obstacles applied on lower wall. Two obstacle shapes, triangular and rectangular, were considered in the simulations. The results revealed that the rectangular obstacles induced larger vortices at higher *Re* than the triangular case. The presence of obstacles in the MCs led to augmented heat transfer in contrast to smooth channels. Also, heat transmission is accelerated by an increase in obstacle height. Furthermore, the local *Nu* was higher for rectangular obstacles than triangular ones, based on the aspect ratio of the obstacle height[16].

Xu et al. (2018) studied laminar forced convective flow in an MC partially filled with a porous medium with using analytical modeling. The slip velocity and the porous-fluid interfaces were considered at the boundary level. The results show velocity increasing in the nonporous area with increasing of Kn numbers as well the boundary velocity also rises. Furthermore, increases in the dimensionless porous thickness, the Darcy number, and reduced in Kn numbers lead to an augmentation flow heterogeneity coefficient [102].

Mozaffari et al. (2019) utilized LBM to study the mixed convection heat transfer in a 2D slip flow regime in an inclined MC with constant heat flux. As an external force, gravity impacted particle interactions and led to mixed convection inside the MC. The results demonstrated that as the inclination angle increased, the velocity variation also increased. Since the buoyancy force is vertical and upward, velocity rises with Kn numbers values increasing and additional fluid dilution; hence at high Kn numbers, the hydrodynamic amplitude is more affected by a variation in inclination angle [46].

Ahangar et al. (2019) applied the LBM to visualize the rarefied gas flow in an MC with a backward-facing step, with two relaxation times in slip and transient flow regimes in inlet and outlet geometry sections. The results indicated that decreasing the Kn number raises the center velocity of vertical wall due to pressure reduction, and the maximum speeds in the slip and transient regimes occur at the MC's end [34].

Orazio et al. (2019) investigated numerically mixed convection heat transport of air in 2D MC using the TLBM-BGK with a microchannel aspect ratio 10. and constant heat flux imposed at the horizontal walls with continuous heat flow. The result shows that the slip velocity peaks at the entrance region and declines along the walls until it achieves a constant value. In addition, the slip velocity increased with the augmentation of Kn numbers values. Also, the Nu numbers decrease and reach a higher value with a lower Kn number value[53].

Duan et al. (2019) investigated laminar slip flow in MC plate-fin heat sinks semi-analytically and numerically. The momentum system is given with the first-order velocity slip boundary conditions at the channel walls to obtain the semi-analytical model for the pressure drop of MC plate-fin heat sinks. The results demonstrate the model's capability to simulate gas slip flow in microchannel heat sinks or implied liquid slip over hydrophobic and superhydrophobic surfaces. Furthermore, it is also helpful in forecasting the pressure drop of slip flow in MC plate-fin heat sinks. The pressure gradient for a slip flow is lower than a no-slip flow, according to the significant impact of developing regions in the MC plate-fin heat sinks state [12].

Shujit et al.(2019) employed the LBM to numerically simulate forced convection laminar fluid flow in a 2D channel having three obstacles across backward and forward-facing steps.

The solid surfaces of the channel and obstacles are maintained at a lower constant temperature, and heated fluid has impinged to flow through them. The results demonstrated that increasing of *Re* and *Pr* numbers increases heat transfer and that obstacle height also plays an important function in the development of vortex [103].

Mohebbi et al.(2019) used the TLBM to analyze the 2D forced convection heat transfer numerically in laminar flow of non-Newtonian fluid flow among two parallel plates filled with partially porous media. The porous media creates by the setting of circular obstacles. The findings demonstrate that using obstacles as porous media in the computational domain improves average *Nu* and thermal performance relative to a channel without obstructions. Furthermore, the *Nu* reduced as the Re decreased [84].

Zhang et al. (2020) investigated the hydrodynamic and thermal properties of mixed convective flow in slip regime for horizontal MC and steady laminar flow, as well as selecting an incompressible newtonian fluid using the LBM. The results indicate that the thermal conversion strength in the inlet regime is susceptible to changes, particularly on the upper wall. In addition, the asymmetric wall heat fluxes significantly impact the temperature field uniformity in the entrance region. Also, the distribution of the local *Nu* becomes extremely sensitive as *Kn* increases, and the location of the heat transfer improvement for the entrance regime transitions from the cold wall [40].

Bahrami et al. (2020) investigated the forced convection heat transfer of an AL_2O_3-*water* nanofluid in a rectangular MC with three injections. The MC bottom wall is insulated, while its upper wall maintains a constant temperature. The findings indicated that heat transfer increased with rib height. In addition, the heat transfer is improved by 46.4% when injectable ribs are present, and heat transmission is further improved by raising the height of injectable ribs [9].

Li et al. (2020) investigated numerically the heat transfer and fluid flow of MC's with solid and porous ribs. The findings indicate that all MC with solid ribs has more significant pressure drops and friction factors than porous ones. Morover, The cases with porous ribs exhibit a higher *Nu* than those with solid ribs. Additional convective heat transfer takes place in porous regions. Furthermore, heat dissipation is enhanced [56].

Zhu et al. (2021) studied MC's with different shapes, rectangular, diamond, and hexagonal, to investigate the influence of the rib shapes on the MC's performance. The results showed that rib shape, size, and configuration are crucial elements that influence performance and heat transfer efficiency. Furthermore, the maximum pressure drop occurs, and the highest*Nu* is obtained when the ribs have rectangular geometry. Furthermore, in the case of the ribs having an elliptic shape with a maximum *Re*, the best effective performance factor is attained. Also, due to the insertion of numerous heat-dissipating ribs into the channel walls, which reduces the surface temperature, particularly at low *Re*, the MC's, including both cavities and ribs, provide improved heat transmission properties [104].

Javaherdeh et al. (2021) studied numerically the fluid flow and heat transfer in a microchannel with four heat sources on the top and lower walls symmetrically concerning the centerline by employing the LBM to solve fluid flow and temperature equations for air, the *Re* ranges from 0.1to 10, and the *Kn* number ranges from 0 to 0.1, with a *Pr* number of 0.71, the slip velocity and temperature jump boundary conditions are used as boundary conditions for microchannels. At the same time, the bounce-back boundary conditions were chosen for the heat sources. It is observed that the velocity increases with *Re* increasing, and the *Re* effect is more prominent in middle region compared to near the walls. Additionally, the temperature rises with an increase in *Kn* due to temperature jump augmentation, which is shifted to the front side and related to temperature jump rising [105].

Ma et al.(2021) simulated forced convective heat transfer properties of laminar flow in three- dimensional rectangular MC with aspect ratios of 0.11 and *Re* of 5400. The results show that the *Re* has significantly influenced the local *Nu* in the thermal zone, particularly at lower *Re*. In addition to the influence of aspect ratio on fluid flow and heat transfer performance, the local *Nu* is also observed to rise with decreasing aspect ratio [58].

Shams et al. (2021) examined the 2D flow over a square cylinder positioned in parallel plates with LBM at low *Re*; solid rectangular blocks of varying lengths obstruct both plates. The findings reveal that spacing ratios significantly impact the cylinder's hydrodynamic forces [106].

Aghamiri et al.(2021) examined the forced convection of nanofluid flow in MC having rotating cylinders in different geometries. The findings suggest that raising the velocity of rotating cylinders, as well as the *Re* and volume fraction of nanoparticles, enhanced heat transfer. As well, the heat transmission is accelerated by raising the *Re*. Additionally, the base fluid's thermophysical characteristics are enhanced by the employment of nanoparticles, and reducing the friction factor is caused by increasing the *Re* [107].

Lobasov et al. (2022) examined the effects of various variables on heat transfer in MC in connection with applying the velocity slip conditions and temperature jump on the walls. The findings indicate that compared to the no-slip condition, it was demonstrated that as the slip length increased, the average heat transfer coefficient increased by about 50%. The heat flux density increased by about 40%. Consequently, there was a considerable reduction in the pressure drop. Considering a temperature jump at the wall resulted in a slight increase in the pressure drop, but it enhanced the heat transfer coefficient [10].

Rostami et al. (2022) studied MC with porous ribs; the MC with a constant heat flow boundary condition imposed on channel walls, while the inlet and exit of the MC the periodic boundary condition was employed. The results indicate that, in comparison to simple channels, ribs increase the rate of heat transmission and pressure drop. In addition, the *Nu* rises with augmentation of the *Re* increases, as well as increases with increasing rib heights [108].

Wang et al. (2022) simulated heat transfer in the MC with porous ribs with TLBM in DDF and the porous media properties. The results show the porous rib generates less pressure and increases *Nu* less than a full-height porous one. Also, due to the porous media's increased heat conductivity, considerably higher temperatures are obtained close to the wall and inside the porous rib [109].

Lori et al. (2022) investigated numerically the fluid flow and heat transfer in MC with periodic vertical porous and solid ribs in various geometrical shapes on MC walls as elliptical, backward triangular and forward triangular, isosceles triangular and rectangular. The results show the pressure in the solid ribs MC is significantly higher than in the porous case; the rectangular ribs case among the MC's with solid ribs has the highest pressure decrease related to the rapid cross- sectional changes at the beginning and end of the ribs. In addition, at lower *Re*, the *Nu* rapidly increases for both solid and porous ribs. MC with porous ribs has greater *Nu* at low *Re*than solid ribs [110].

Su et al. (2022) numerically studied the rarefaction flow in parallel plate and circular MC. The effects of temperature jump, axial heat conduction, and velocity slip are considered. The findings show the velocity gradient and temperature gradient drop as *Kn* increases and *Nu* number reduces. In addition, the *Kn* numbers have a significant effect on reduced friction loss [28].

Shao et al. (2022) analyzed the fluid flow and heat convection in rectangular MC exchangers employing LBM and multiple relaxation collision. In addition, the impact of structured surfaces was also investigated by selected rectangular, hemispherical, and triangular micro-bulge shapes. The results illustrate that the heat transmission improves by the structured heat transfer, with the optimum performance resulting from a surface with rectangular micro-bulges. Furthermore, the *Re* reduces with augmentation of the micro-bulge height [64].

Liu et al. (2022) simulated the fluid flow and heat transfer in an MC heat sink with double- layered. The results show an increasing temperature with *Re* augmentation, the *Nu* increase also while the average friction factor decrease. The results also illustrated that the MC heat sink with double-layered has lower thermal resistances with a higher *Nu* and a higher friction factor [59].

Murali et al. (2022) studied forced convection heat transfer in a rectangular MC by introducing a $CuAl_2O_2$-*water* hybrid nanofluid. The results demonstrated an enhancement in heat transfer rate with volume fraction augmentation. However, there was a slight increase in the pressure drop. In addition, the results show an augmentation in Nusselt number values [60].

Ferhi, M.,and Djebali,R. (2022) investigated flows and heat transfers in MC filled with *Cu-water* under the slip flow regime with LBM. The findings indicate that the nanoparticles volume fraction, *Re*, and *Kn* augmentation enhance the heat transfer rate, except at high *Re* values. Additionally, the slip velocity and temperature jump increase with *Kn* rising [66].

Shao et al.(2023) investigated the fluid flow and convective heat transfer in an MC exchanger using the LBM and MRT models. The impact of a structured surface with triangular, hexagonal, and rectangular micro-bulges on fluid flow and heat transmission are being investigated. The simulation results indicate that using a structured heat transfer surface can significantly improve heat transfer efficiency, with the surface featuring rectangular micro-bulges exhibiting the highest performance. Additionally, as the height of the micro-bulges increases, the *Re* [21]

Chapter 2

Simulation workflow

2.1 Simulation workflow

The microscale level presents unique challenges for CFD techniques. The LBM has developed as a favorable alternative owing to its simplicity and capability to manage complex microstructures [40]. In particular, the TLBM has become increasingly popular for addressing heat transfer and fluid flow issues due to its recent development and numerous potential applications [84]. The DDF approach, which uses two distribution functions to represent the velocity and temperature fields, respectively, is particularly useful in this context [42, 82]. This study underscores the potential of using TLBM to enhance heat transmission and fluid flow in microscale systems. Furthermore, it is a promising tool with the potential to significantly contribute to the progress of fluid mechanics and heat transfer research.

2.2 Thermal lattice Boltzmann method

The present study investigates fluid flow and heat transfer using the TLBM with a DDF and BGK model. The discrete equations 2.1 and 2.2 [67] are utilized to represent the mathematical framework.

$$f_i(x + c_i\Delta t, t + \Delta t) - f_i(x,t) = -\frac{1}{\tau_f}\left[f_i(x,t) - f_i^{eq}(x,t)\right] \tag{2.1}$$

$$g_i(x + c_i\Delta t, t + \Delta t) - g_i(x,t) = -\frac{1}{\tau_g}\left[g_i(x,t) - g_i^{eq}(x,t)\right] \tag{2.2}$$

Where the f_i, g_i are the velocity distribution for density and internal distribution function and f_i^{eq} ,g_i^{eq} their distribution function at the equilibrium. The terms τ_f and τ_g correspond to the momentum relaxation time and internal energy relaxation time, respectively.

This study employs a two-dimensional D_2Q_9 lattice model connected by eight links, as Figure 2.1 shows. The model features a central node connected to eight neighboring nodes, and momentum and energy are transferred between them through distribution functions during a streaming-collision process [82].

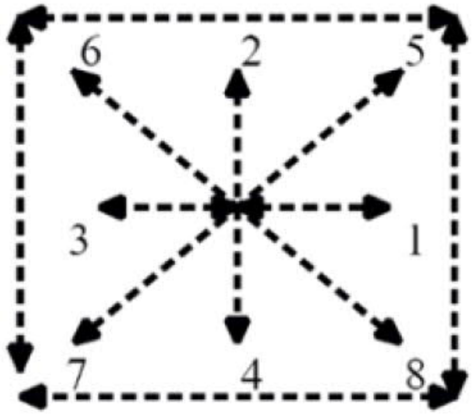

Figure 2.1: D_2Q_9 square lattice model.

The equilibrium function f_i^{eq} and g_i^{eq} be written for a D2Q9 square lattice as follows [84, 111]:

$$f_i^{eq} = \omega_i \rho \left[1 + \frac{3c_i u}{c^2} + \frac{9c_i u^2}{2c^4} - \frac{3(u \cdot u)}{2c^2} \right] \tag{2.3}$$

$$g_0^{eq} = -\omega_0 \rho \varepsilon \frac{3(u \cdot u)}{2c^2} \tag{2.4}$$

$$g_{1,2,3,4}^{eq} = \omega_{1,2,3,4} \rho \varepsilon \left[1.5 + \frac{3c_i \cdot u}{2c^2} + \frac{9c_i \cdot u^2}{2c^4} - \frac{3(u \cdot u)}{2c^2} \right] \tag{2.5}$$

$$g_{5,6,7,8}^{eq} = \omega_{5,6,7,8} \rho \varepsilon \left[3 + \frac{6c_i \cdot u}{c^2} + \frac{9c_i \cdot u^2}{2c^4} - \frac{3(u \cdot u)}{2c^2} \right] \tag{2.6}$$

The lattice velocity is determined by $c = \Delta x / \Delta t$, where $\Delta x, \Delta t$ denoted, respectively, the space grid and time step.

$$\begin{array}{ll} c_i = (0,0) & (i=0) \\ c_i = \left[\cos \frac{(i-1)\pi}{2}, \sin \frac{(i-1)\pi}{2} \right] c & (i = 1-4) \\ c_i = \sqrt{2} \left[\cos \frac{(i-1)\pi}{4}, \sin \frac{(i-1)\pi}{4} \right] c & (i = 5-8) \end{array} \tag{2.7}$$

In D2Q9, the weighting coefficient is presented by ω_i [89, 111]

$$\begin{aligned} \omega_i &= 4/9 && \text{for } i = 0 \\ \omega_i &= 1/9 && \text{for } i = 1, 2, 3, \text{ and } 4 \\ \omega_i &= 1/36 && \text{for } i = 5, 6, 7, \text{ and } 8 \end{aligned} \tag{2.8}$$

In the thermal model, the thermal diffusivity χ and the kinematic viscosity v are the key parameters in the simulation of a flow with heat transfer terms and can be expressed as below:

$$\chi = \left(\tau_f - \frac{1}{2}\right) c_s^2 \delta t$$

The kinematic viscosity is given by

$$v = c_s^2 \left(\tau_g - \frac{1}{2}\right) \delta t$$

In LBM simulation, the pressure is considered an output variable and can be determined using an equation of state [74, 112] :

$$p = c_s^2 \rho \tag{2.9}$$

For the D_2Q_9 , the sound speed c_s equal to $c_s = c/\sqrt{3}$.

The Prandtl number can be correlated to the relaxation time as [94] :

$$\mathrm{Pr} = \frac{\tau_f}{\tau_g} \tag{2.10}$$

2.3 Relationship between the Knudsen number and relaxation times

In the LBM, the relaxation times can be linked to the Knudsen number [94]:

$$\begin{aligned} \tau_f &= \sqrt{\frac{6}{\pi \gamma}} H.kn \approx H.kn \\ \tau_g &= \frac{H.kn}{\mathrm{Pr}} \end{aligned} \tag{2.11}$$

The macroscopic variables, namely density, velocity, and temperature, can be obtained as functions of the distribution function [98]:

$$\begin{aligned} \rho &= \sum_i f_i \\ \rho u &= \sum_i f_i c_i \\ T &= \sum_i g_i \end{aligned} \tag{2.12}$$

2.4 Boundary Conditions

2.4.1 Flow boundary conditions

The input velocity is known for the inlet boundary condition, but the density is unknown and necessitates determination. Zou and He correlations can be utilized to assess inlet density and unknown distribution functions. The unknown distribution functions on the left boundary of MC and the density can be expressed in [67, 112].
The outlet velocity is unknown. Extrapolation is commonly used to calculate unknown distribution functions at the east boundary[113, 114] .
In the slip flow regime, the fluid velocity near the wall differs from the wall velocity. The slip boundary condition for a bottom and top wall is provided in [6]:

2.4.2 Temperature boundary conditions

The inlet temperature distribution function are given as [67]:

$$\begin{aligned} g_1 &= \frac{1}{9} T_{in}(3 + 6u_x^2) - g_3 \\ g_5 &= \frac{1}{36} T_{in}(6 + 6u_x^2) - g_7 \\ g_8 &= \frac{1}{36} T_{in}(6 + 6u_x^2) - g_6 \end{aligned} \tag{2.13}$$

The outlet temperature boundary condition can be determined by employing an extrapolation method [113, 114]:

For a top wall, the equations of temperature jump are given as below [67]:

$$\begin{aligned} T_{y=H} &= \frac{C_{\text{jump}}\left(4T_{H-1} - T_{H-2}\right) + 2T_w}{\left(2 + 3C_{\text{jump}}\right)} \\ g_4 &= 1.5T_{y=H}(\omega(2) + \omega(4)) - g_2 \\ g_7 &= 3T_{y=H}(\omega(5) + \omega(7)) - g_5 \\ g_8 &= 3T_{y=H}(\omega(6) + \omega(8)) - g_6 \end{aligned} \tag{2.14}$$

The local friction coefficient $C_f(x)$ and Nusselt number (Nu) are expressed [67], and Reynolds number in [115] :

$$\begin{aligned} C_f(x) &= \left.\frac{\mu(\partial u/\partial y)}{(1/2)\rho u_{bulk}^2}\right|_w \\ Nu(x) &= \left.\frac{k2H}{K\left(T_w - T_{bulk}\right)} \frac{\partial T}{\partial y}\right|_w \\ \mathrm{Re} &= \frac{UH}{\nu} \end{aligned} \tag{2.15}$$

For detailed discussions regarding the boundary conditions, refer to Appendix A.

2.5 Thermophysical properties of nanofluids (Cu-Water Nanofluid)

The thermophysical properties of nanofluids are required to evaluate their performance in microchannels in the third section. This can be achieved by referring to previously published literature. In particular, the density of nanofluids can be determined using [57, 116]. While the heat capacitance can be obtained in [67]:

$$\rho_{nf} = \rho_s \varphi + \rho_{bf}(1-\varphi) \tag{2.16}$$

$$(\rho C_p)_{nf} = \varphi(\rho C_p)_s + (1-\varphi)(\rho C_p)_{bf} \tag{2.17}$$

bf, s, n_f, φ are subscripts referring to the base fluid, solid nanoparticles, nanofluid, and nanoparticle volume fraction, respectively.

It is essential to note that all third study's section use these previously mentioned nanofluid subscripts.

Additionally, Yu and Choi suggested a thermal conductivity model for spherical particle nanofluids [57, 117].

$$k_{nf} = \frac{k_s + 2k_{bf} + 2\varphi(k_s - k_{bf})}{k_s + 2k_{bf} + \varphi(k_{bf} - k_s)} k_{bf} \tag{2.18}$$

The thermal conductivity and the nanoparticle volume fraction, respectively, are depicted by k_{nf}, φ.

The dynamic viscosity of nanofluids is determined as [67]:

$$\mu_{nf} = \frac{\mu_{bf}}{(1-\varphi)^{2.5}} \tag{2.19}$$

2.5.1 Nanofluid properties of copper and water

The thermophysical characteristics of copper(as nanoparticles) and water (as the base fluid) are displayed in table 2.1. The thermophysical properties of the nanofluid can be established by considering the properties of both the nanoparticles and the base fluid [118].

Table 2.1: Thermophysical properties of water and copper [115]

	$\rho\,(\mathrm{Kg}\cdot m^3)$	$k\,(W\cdot m^{-1}\cdot K^{-1})$	$C_p\left(J\cdot \mathrm{Kg}^{-1}\cdot K^{-1}\right)$	μ(Pa.s)
Water	997.1	0.613	4179	0.000891
Copper (Cu)	8933	400	385	

2.6 Grid independency

Table 2.2 depicts the outcomes of a research study that analyzed the effect of mesh resolution on numerical simulations at a specific section of $x = 0.5.L$. The study employed different mesh resolutions to assess their effect on the accuracy and stability of the simulations at a Knudsen number of 0.015 .

Table 2.2: Mesh independency

Mesh size	105*15	110*20	115*25	120*30	125*30	$130 * 40$
Normalized Velocity (u/u_{in})	0.0930	0.0925	0.0912	0.0887	0.0882	0.0886
Normalized Temperature (T/T_{in})	9.8502	9.8377	9.8205	9.8096	9.8093	9.8095

According to the findings presented in Table 2.2 , a (120×30) mesh resolution was identified as the most appropriate for the current investigation.

2.7 Numerical method and validation

To ensure the accuracy of the simulation results, a comparison was conducted between the velocity profiles obtained via LBM and those acquired through DSMC by Roohi et al.[119]. The comparison showed that the velocity profiles obtained from DSMC and LBM were in good agreement, as demonstrated. in Figure 2.2. The comparison also revealed a significant agreement between the findings produced by the two approaches.

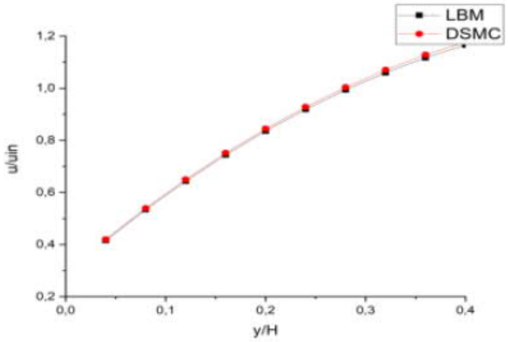

Figure 2.2: Comparison of velocity curves with those acquired by Roohi et al.[116] for Kn = 0.113.

The present study was conducted in Python to simulate heat transfer and fluid flow in an MC. The results were compared with those [67]. Velocity and temperature have, without obstacles have been validated at (Kn)= 0.015 and 0.03. From Figures [2.3, 2.4] the results show a good agreement.

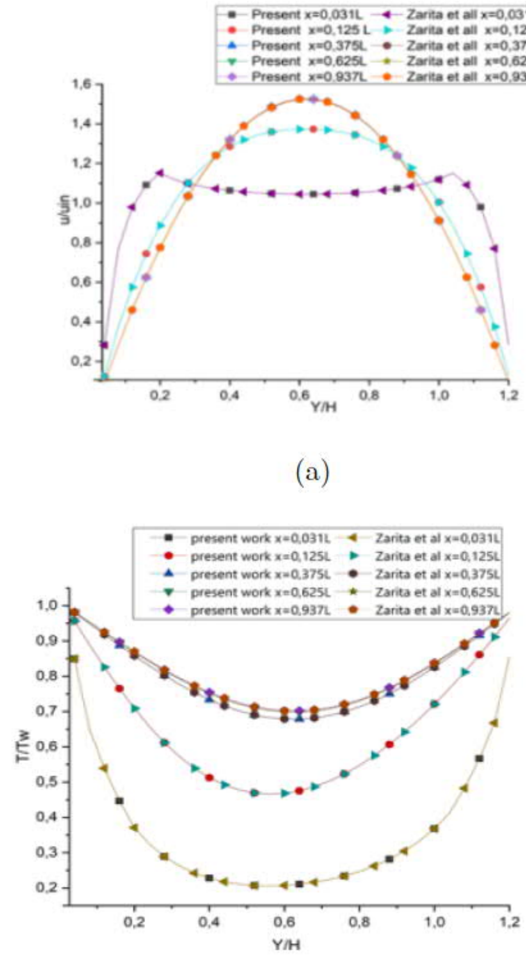

(a)

(b)

Figure 2.3: Comparison of temperature and velocity profiles for Kn=0.015 with [67] (a) Velocity, and (b) Temperature.

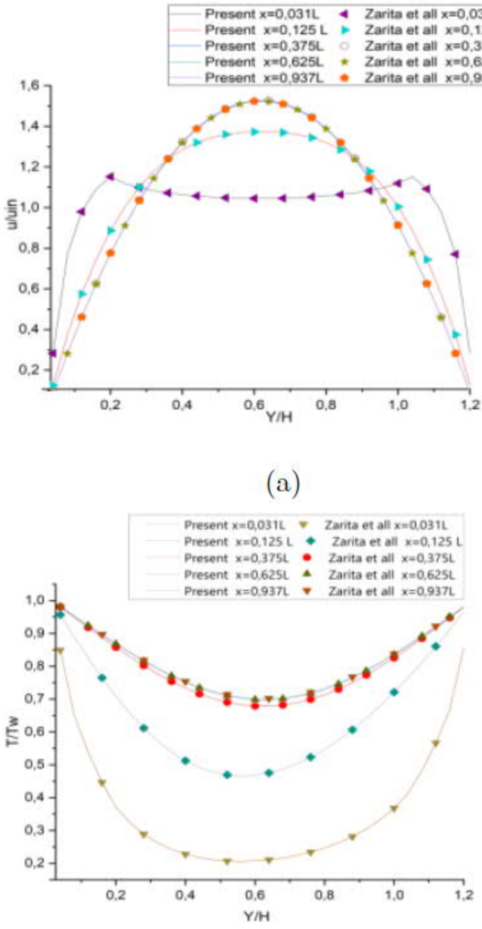

(a)

(b)

Figure 2.4: Comparison of temperature and velocity profiles for Kn=0.03 with [67]
a) Velocity, and (b) Temperature

The Nusselt number also shows a suitable agreement with various Kn numbers, as indicated in Figure 2.5. The figures display the desired accuracy for employment developed code for the following simulation.

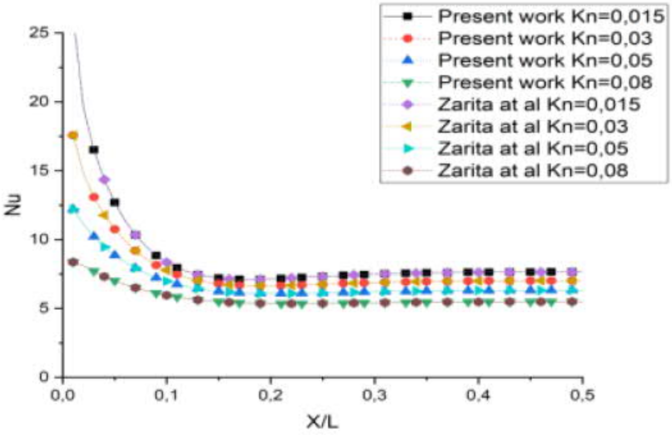

Figure 2.5: Comparison of Nusselt number for different Kn numbers with Ref [67]

The figures clearly show that the code has achieved the desired accuracy for the simulation used in the study. These figures provide concrete evidence, confirming the code's effectiveness and reliability in creating an accurate and robust simulation environment

2.8 Implementation of the TLBM

This section provides a comprehensive overview of the practical steps required to effectively implement the TLBM on a computer system. By following the guidelines presented here, researchers will be equipped with the knowledge and insights required to harness the potential of TLBM effectively. This knowledge facilitates and fosters advancements in computational fluid dynamics and related disciplines.

The initial section presented the geometric data as the size of the mesh. We also set up the distribution function and its equilibrium distribution, along with various parameters such as weight factors, discrete velocities, and relaxation rates, which are all relevant to the study. Furthermore, the simulation requires setting up the fluid parameters and their relationship. Afterward, the macroscopic variables, exemplified by density and velocity, are computed, along with the calculation of their corresponding equilibrium functions.

Once the collision and streaming processes for the hydrodynamic field are completed, the velocity boundary condition is set up. The same procedure is repeated for the temperature field by computing the temperature and distribution function. The temperature boundary condition is then established after the collision and streaming operations of the thermal field. The simulation then starts a new loop until it meets a specified criterion, such as the maximum number of iterations. Finally, the desired results are displayed.

The computational flowchart (2.6) illustrates these steps. In terms of coding, we utilized Python engineering software to develop our calculation codes by implementing the algorithm discussed in the research topic. Specifically, we simulated the rarefied flow in a MC with the thermal lattice Boltzmann method with a double distribution function via a single relaxation time BGK approach.

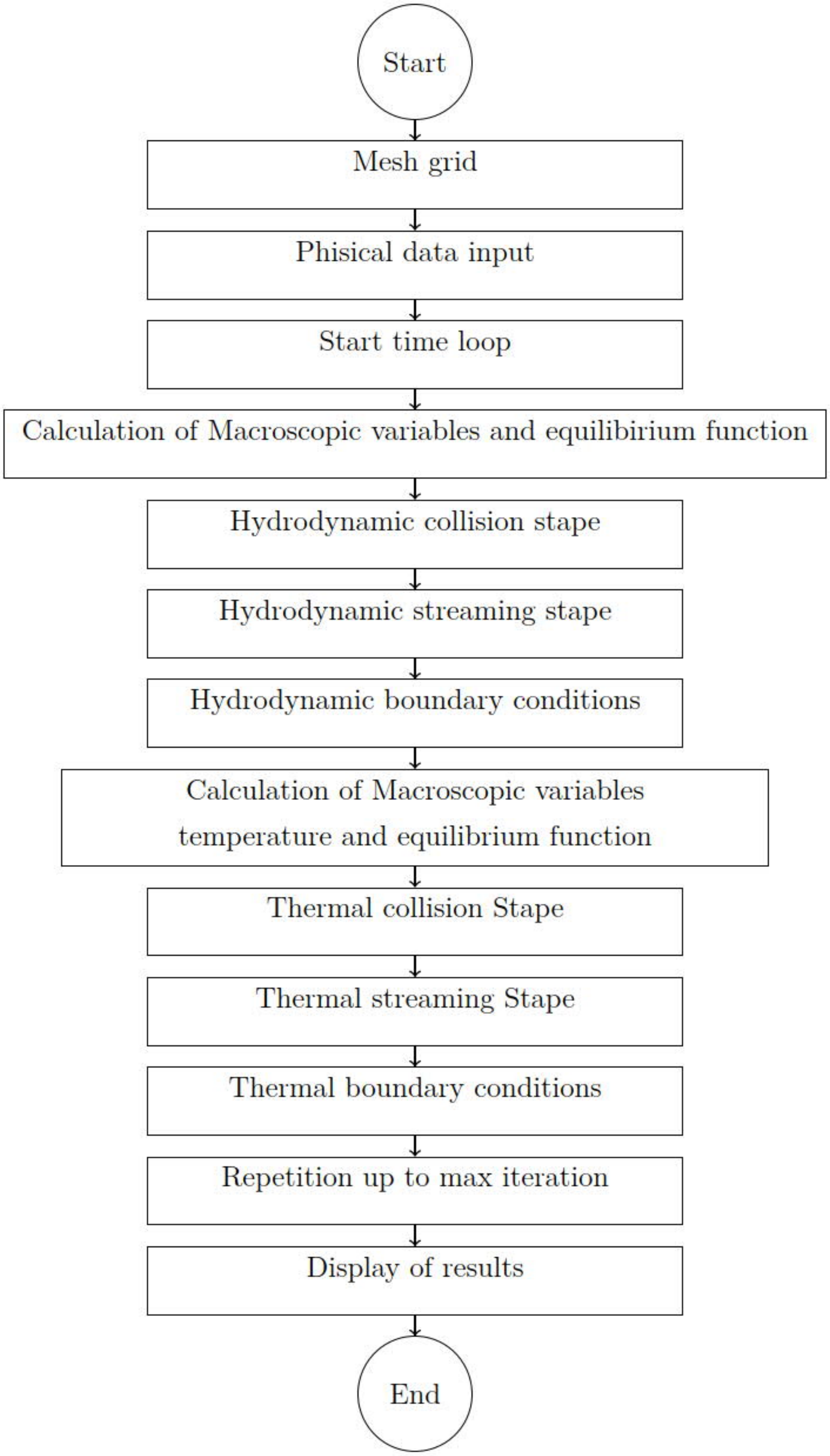

Figure 2.6: Program flowchart

Chapter 3

Results and Discussion

3.1 Introduction: Result and Discussion

Nowadays, as technology advances, electronic components are getting smaller in size. They generate a lot of heat flow, which can harm these parts. Consequently, these components are cooled using MC's that are incorporated into them[108]. In various industrial applications, the utilization of MC heat sinks is rising. As a result, the analysis of MC heat sinks has grown in significance as research interest in the flow and heat transmission in MC's [12]. Heat transfer is a natural phenomenon arising from differences in temperature either between two separate objects or within a single object. Due to its extensive use in manufacturing processes and industrial fields, the heat transfer phenomenon has drawn scientists and engineers' interest[22]. The application of passive methods to increase the MC heat sink efficiency to obtain more excellent heat dissipation in smaller sizes with lower costs has recently received much attention[13, 110] . Various strategies are used to increase heat transfer efficiency through MC's, including using nanofluid as the coolant, optimizing the geometry of MC's, using wavy microchannels, and employing double layers of microchannels. The most common choice for enhancing heat transfer performance among these strategies is the geometry optimization of microchannels [56] , and modifying the microchannel's design leads to an enhanced heat transfer rate[55, 108].

3.2 First section

3.2.1 Problem statement

In the first numerical investigation section, the laminar fluid flow through the 2D rectangular MCs without and with alternating obstacles is studied with the TLBM to analyze the convection heat transfer and fluid flow. A unit length L of the MC is considered. In the initial case, the MC is without any obstacles. In the second case, three obstacles are introduced, with two placed at the top and one at the bottom of the MC. The third case involves six obstacles positioned at the top and three at the bottom, as depicted in Figure [3.1]. The inlet velocity and flow temperature remain consistent at the MC inlet while the MC walls remain stationary. Moreover, the wall's temperature is maintained the same and equal $T_w = 10T_{in}$. The dimensions L_0 and L_1 correspond to the length of the obstacle in the second and third cases, respectively. In addition, H is the width of MC and W_0 is the obstacle width. The dimension d_0 indicates the distance between the two obstacles in the second case that are positioned in the top wall as well as the obstacle distance from the inlet on the lower wall, and d_1 represents the distance separating obstacles in the third case. Figure [3.1] shows the MC's configurations.

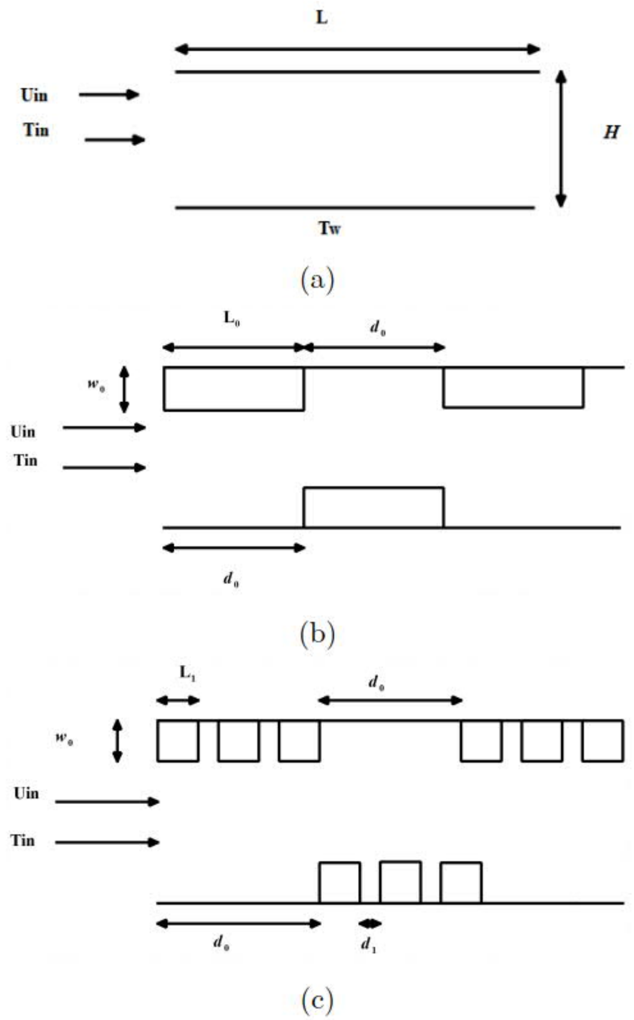

Figure 3.1: Microchannel configuration; a: without obstacles, b: with three obstacles, c: with nine obstacles

3.2.2 Velocity distribution

Figures [3.2, 3.3,3.4] represent the MC's velocity distribution for $Kn = 0.012 - 0.02$ and $Kn = 0.05$. In the absence of obstacles, the velocity decreases with the increase of Kn numbers. In case of obstacles, the velocity drops as the Kn number values grow, and the velocity values increase in the case of obstacle implementation. The velocity profiles demonstrate that the performance of obstacles plays a crucial role in enhancing velocity. Notably, the impact of obstacles on velocity distribution is most pronounced in the case of three obstacles with low Kn numbers. However, the results emphasize the significance of the rarefaction effect on velocity distribution, particularly observing that its influence is more substantial in the middle of the MC compared to the regions near the walls.

Nonetheless, the results highlight the significance of the velocity distribution concerning the rarefaction effect. As previously suggested by an earlier study, it is noteworthy that this effect is more pronounced in the MC middle than in proximity to the walls [13]. Our analysis clearly suggests that the presence of obstacles significantly impacted velocity augmentation.

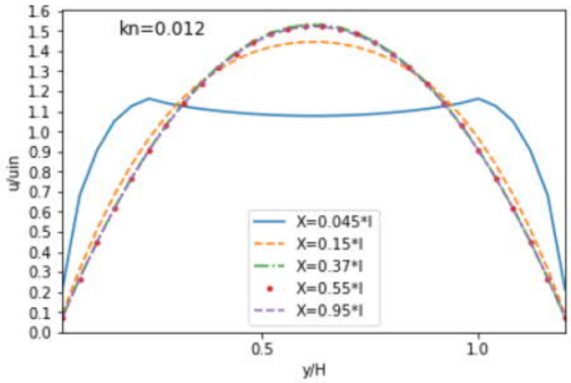

(a) $Kn = 0.012$

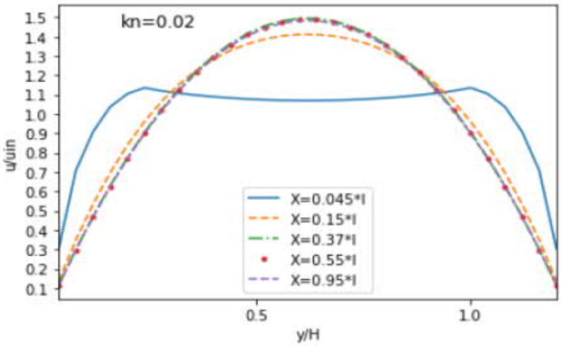

(b) $Kn = 0.02$

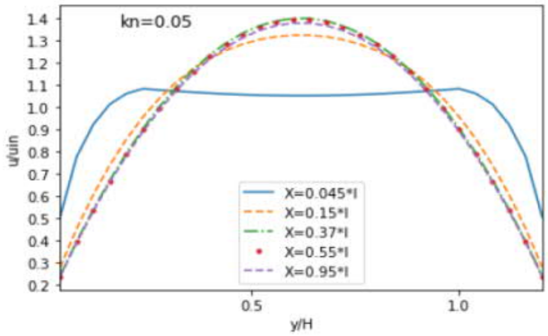

(c) $Kn = 0.05$

Figure 3.2: Velocity without obstacles for different Kn numbers.

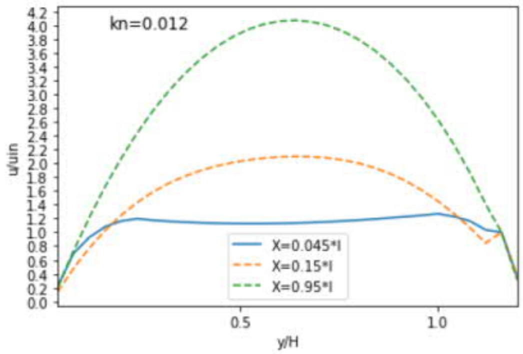

(a) $Kn = 0.012$

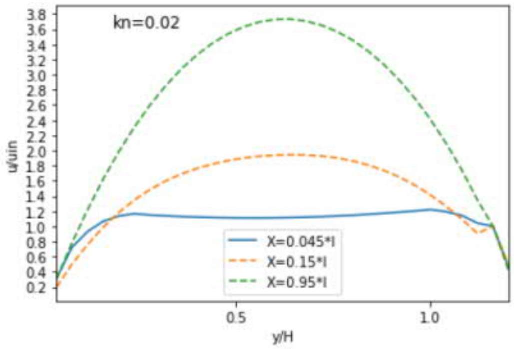

(b) $Kn = 0.02$

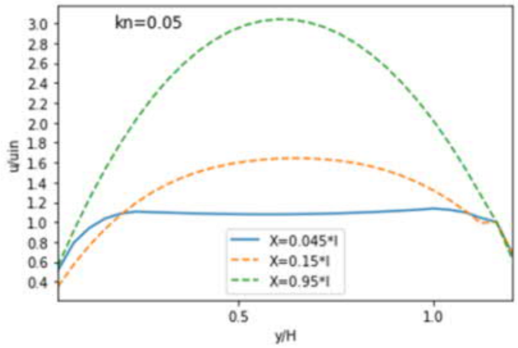

(c) $Kn = 0.05$

Figure 3.3: Velocity with three obstacles for different Kn numbers

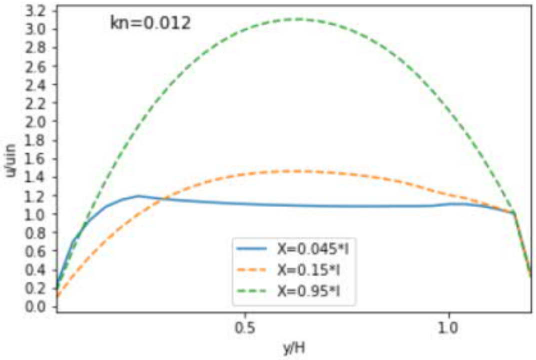

(a) $Kn = 0.012$

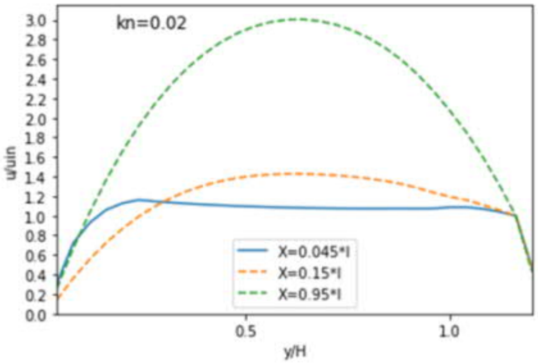

(b) $Kn = 0.02$

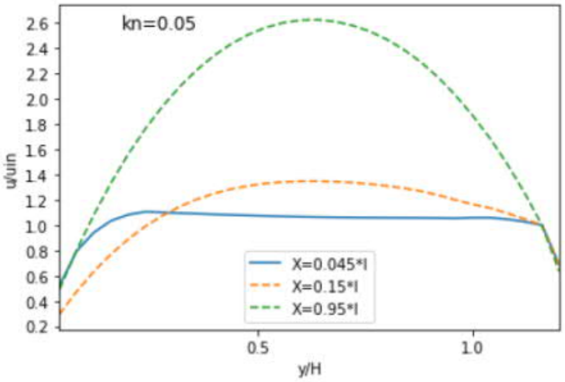

(c) $Kn = 0.05$

Figure 3.4: Velocity with nine obstacles for different Kn numbers.

Figure 3.5 shows the velocity streamlines in various cases with $Kn = 0.05$. In the developing region, the velocity field exhibited a rapid and substantial increase until it reached a maximum at the center of the MC, as illustrated by the streamlined structures without obstacles in Figure 3.5a. Also, the fluid close to the wall maintains a minimum velocity. In the cases of obstacles, the velocity field rises slowly due to obstacles but with a high value compared to the first case. Additionally, in the third scenario, considerable deceleration was observed in the developing region. The rarefied flow's velocity reached its peak value upon exiting the MC, which was higher than the velocity observed in the first scenario with no obstacles. These results clearly demonstrate that the presence of obstacles significantly impacted accelerating the velocity of the rarefied flow within the MC.

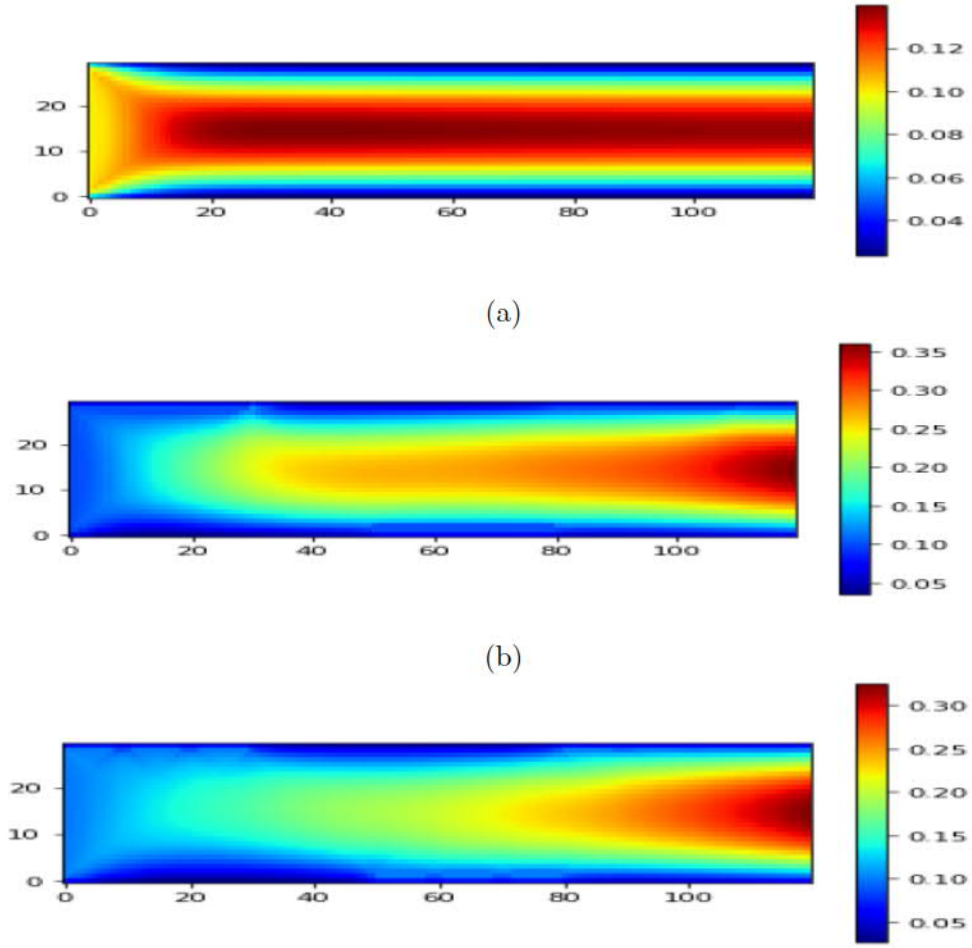

(a)

(b)

(c)

Figure 3.5: Velocity streamline for $Kn = 0.05$ a: with no obstacle, b: three obstacles; c: nine obstacles

Figure 3.6 illustrates the velocity contours for different cases with $Kn = 0.05$ along the MC. In the absence of obstacles, in Figure 3.6a, it can be seen that the velocity contours are parallel and increase symmetrically from the top and bottom walls of the MC to reach their maximum values at the MC center. In the other cases, Figures 3.6b and 3.6c, the velocity contours are distorted around the obstacles, and they increase slowly from the developing region with higher values than in the previous case. It can be noticed that in the case with nine obstacles, Figure 3.6c shows that the fluid flows slowly through the MC but accelerates as it exits. Analyzing these findings is crucial in evaluating the effectiveness of the obstacles installed in the MC with velocity slip and temperature jump. Moreover, examining the changes induced by the obstacles in the velocity contours of the microchannel contributes to improving the flow acceleration.

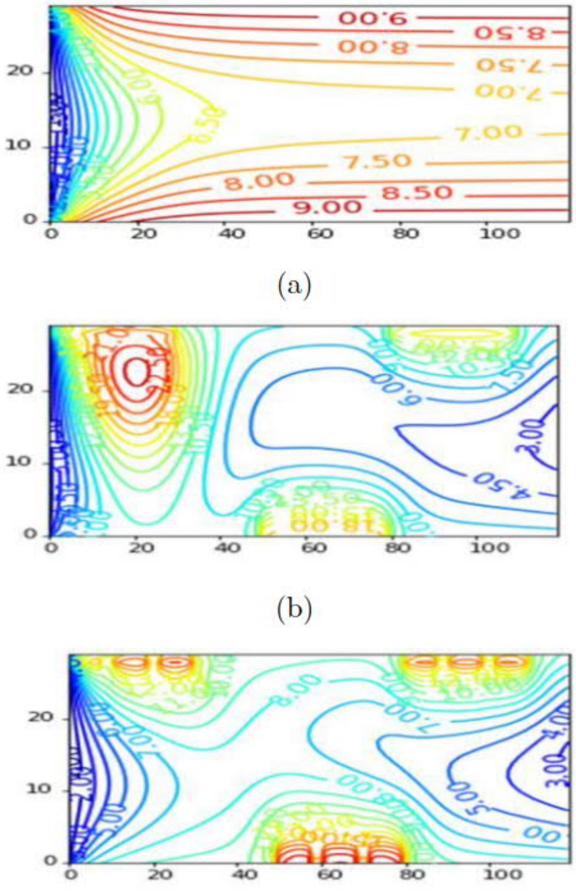

(a)

(b)

(c)

Figure 3.6: Velocity contour for $Kn = 0.05$;a: with no obstacle, b: with three obstacles; c: with nine obstacle

3.2.3 Temperature distributions

Figures 3.7,3.8, and 3.9 depict the temperature distribution along MC for three scenarios with Kn values ranging from 0.012 to 0.05. In the absence of obstacles in the first case, there was a decrease in temperature with an increase in the Kn number, as depicted in Figure 3.7.

These results suggest that the fluid's temperature rises as the dimensionless axial distance increases [58].

Even when adding obstacles, the temperature continues to decrease. The temperature reduction is noticeable when nine obstacles are added, as seen in Figures 3.7a and 3.9a. Moreover, the impact of rarefaction in the middle region is more prominent compared to the region close to the wall. This is attributed to the substantial temperature difference observed near the wall, which arises due to the rapid establishment of hydrodynamic and thermal boundary layers in the entrance area, as illustrated in Figure 3.10. To sum it up, the MC with obstacles exhibits superior heat transfer enhancement compared to a smooth MC. In summary, the MC with obstacles shows superior heat transfer improvement compared to a smooth MC.

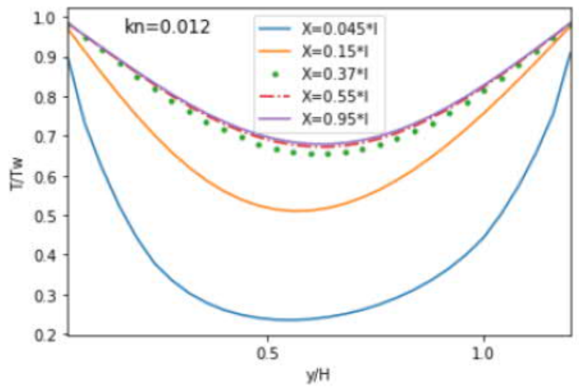

(a) $Kn = 0.012$

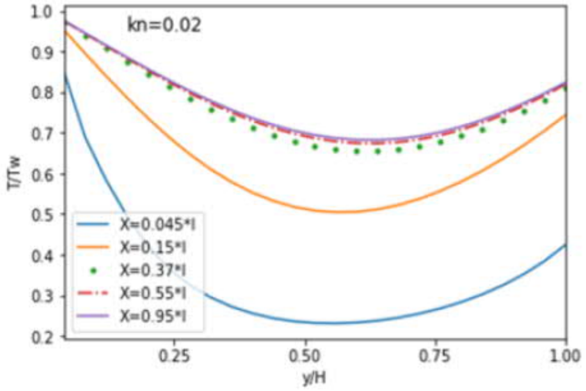

(b) $Kn = 0.02$

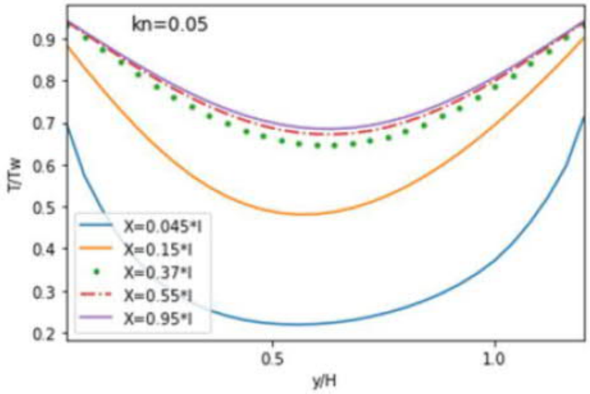

(c) $Kn = 0.05$

Figure 3.7: Evolution of the T according to different Kn numbers: Case with no obstacles.

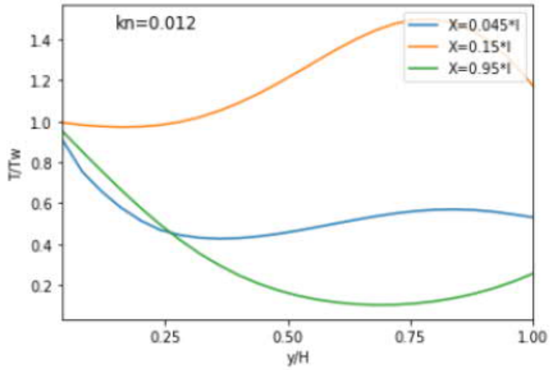

(a) $Kn = 0.012$

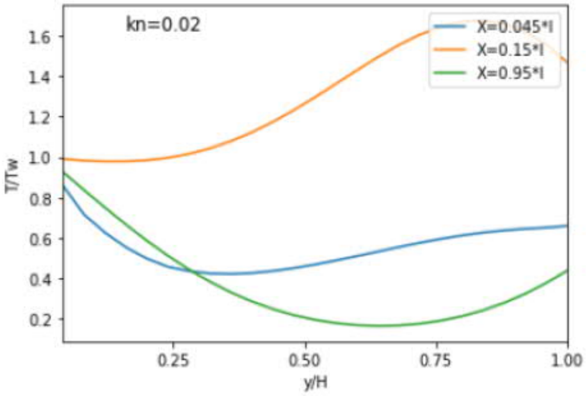

(b) $Kn = 0.02$

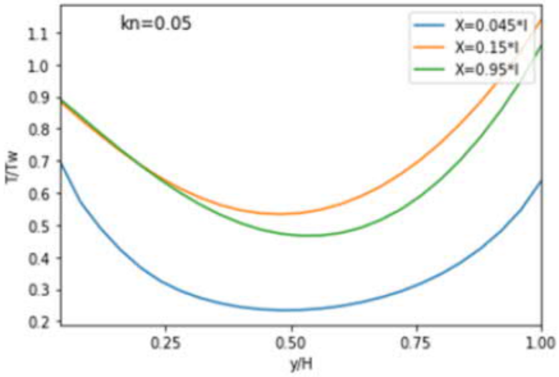

(c) $Kn = 0.05$

Figure 3.8: Evolution of the temperature according to different Kn numbers: Case with three obstacles.

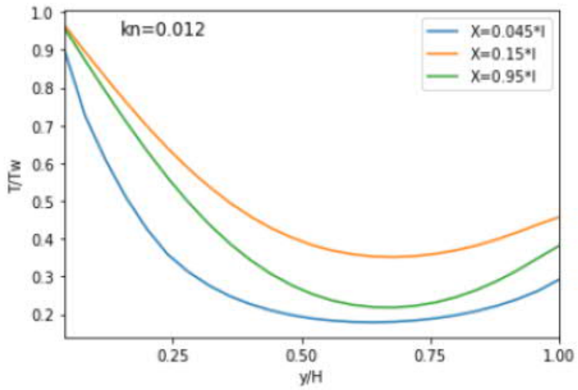

(a) $Kn = 0.012$

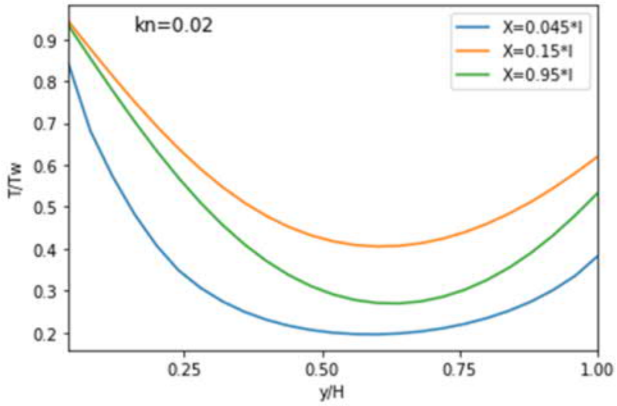

(b) $Kn = 0.02$

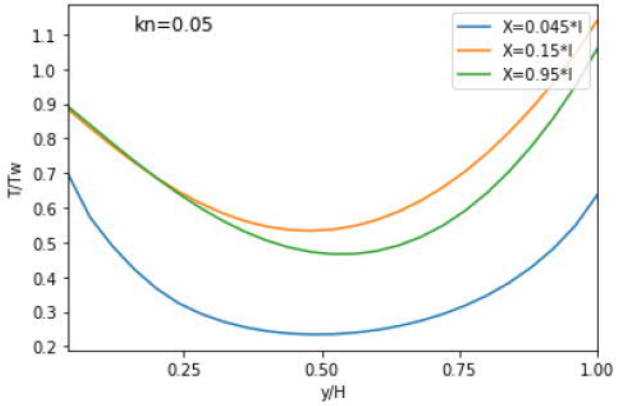

(c) $Kn = 0.05$

Figure 3.9: Evolution of the temperature according to different Kn numbers: Case with nine obstacles

From the streamline in Figure 3.10, in the case of the MC without obstacles (Figure3.10a), the temperature experiences a rapid decrease from the wall towards the neighboring layers, ultimately reaching a low value in the middle region of the MC. Compared to other obstacles, the temperature decreases slowly towards the first obstacle in the second case (Figure3.10b). However, the fluid flows more rapidly in the scenario with nine obstacles, as evidenced by the temperature profile shown in Figure 3.10c. Nevertheless, compared to the case without obstacles, the presence of obstacles causes fluctuations in the temperature of the fluid at the wall and its adjacent layers. Moreover, it leads to an overall increase in temperature in the central area of the MC.

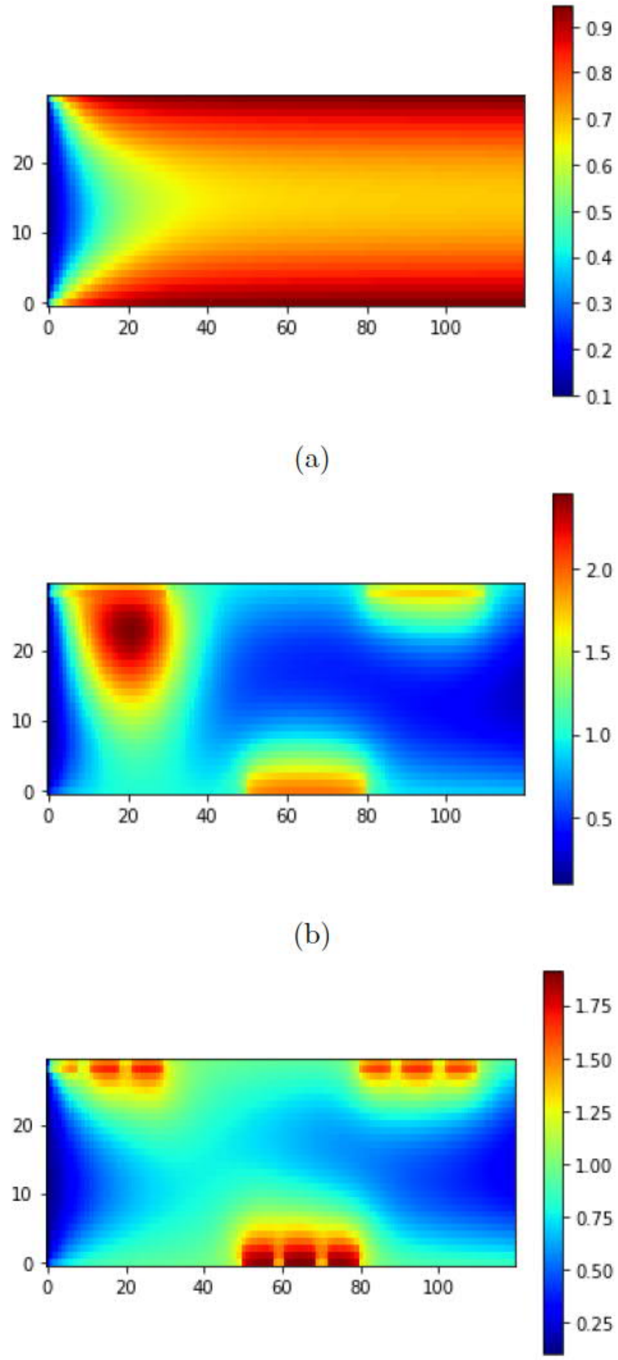

(a)

(b)

(c)

Figure 3.10: Temperature streamline for$Kn = 0.05$ a: with no obstacle, b: with three obstacles; c: with nine obstacles

The study incorporated a temperature contour to better illustrate the heat transfer improvement mechanism achieved by obstacles. Figure 3.11 displays the temperature contours for $Kn = 0.05$ along the MC. The temperature contours are notably parallel in the absence of obstacles, with their values increasing in the central region. However, the presence of obstacles creates a distinct flow structure, as depicted in the figures. Furthermore, the figures illustrate the heat transfer division among the obstacles in the other cases, Figures 3.11b and 3.11c. Furthermore, the temperature contours become distorted in the three obstacles case, and a vortex is formed near the first obstacle. However, in the nine obstacles case (Figure 3.11c), this vortex disappears. However, low values are attained at the MC exit. And an increase in the temperature values along the MC is perceived with the Kn number augmentation. These results play a critical role in assessing the overall effectiveness of the obstacles in controlling the temperature within the MC. Furthermore, utilizing TLBM with a double distribution function allows for a comprehensive investigation of the thermal performance of rarefied flow in rectangular MC's with obstacles at different Knudsen numbers. This analysis considers slip velocity and temperature jump boundary conditions.

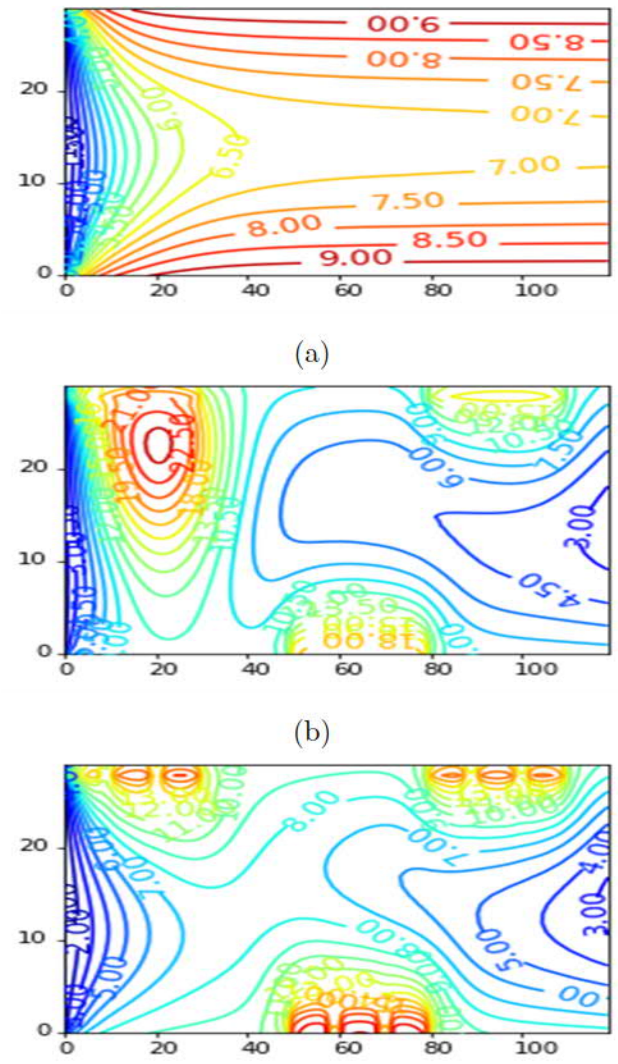

(a)

(b)

(c)

Figure 3.11: Temperature contours for Kn=0.05 a: with no obstacle, b: with three obstacles c: with nine obstacles

3.2.4 Nusselt number

The evolution of the *Nu* number according to various *Kn* numbers is shown in Figure 3.12. The *Nu* number varies from 0.05 to 0.08 along the MC for the different studied cases. The results demonstrate that the *Nu* number decreases as the *Kn* number increases. The findings demonstrate that the *Kn* number significantly influences the *Nu* number, even at low values. Additionally, the maximum value of the Nusselt number is observed at the inlet of the MC. Furthermore, due to the temperature gradient at the entrance region, the highest values were reached in the second case compared to the third one. TheNu number's higher values denote that heat transfer is more efficient. Hence, rarefaction effects can substantially impact the Nu number in rarefied flows in the slip regime. From $x = 0.6$, In the second and third cases, the temperature gradient remains nearly constant for various Knudsen numbers, indicating that the rarefaction effect is no longer predominant in these scenarios. Furthermore, theNu continues to decrease until the end of the MC [120]. Additionally, the findings show that convection reduces and conduction increases.

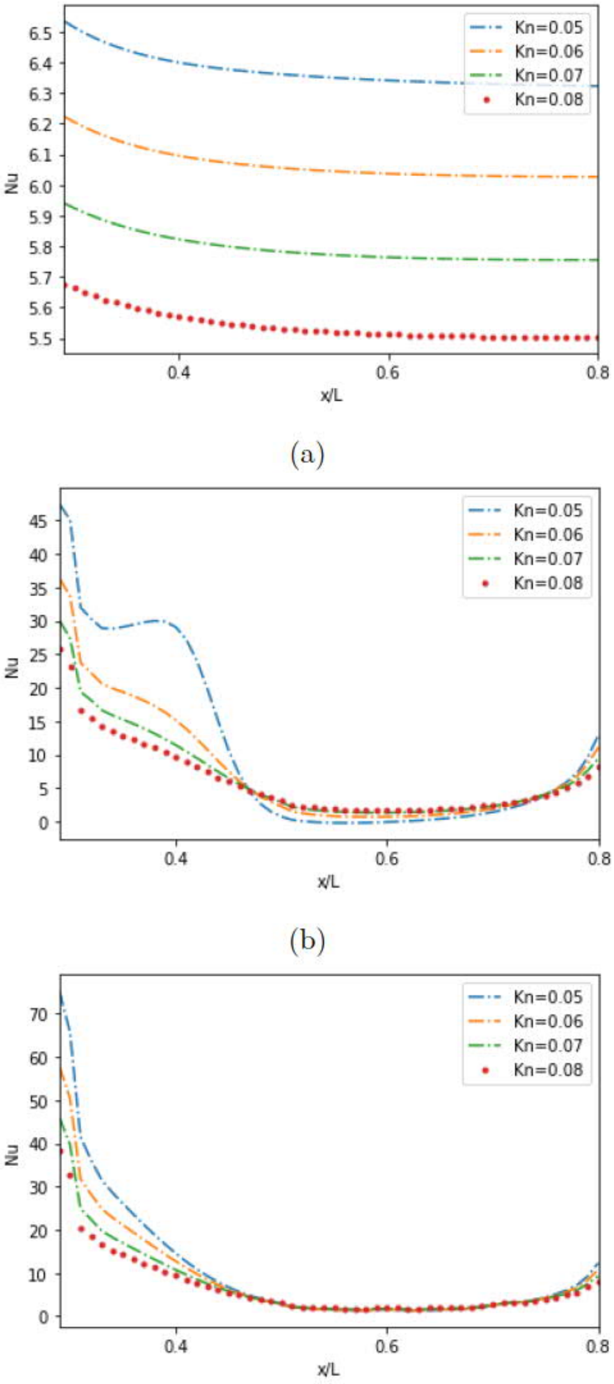

(a)

(b)

(c)

Figure 3.12: Effect of Knudsen number on Nusselt number a: with no obstacle, b: with three obstacles, c: with nine obstacles

3.2.5 Skin friction coefficient

In Figure 3.13, due to the rapid increase in velocity at the entrance zone and the subsequent reduction in velocity gradient, the results indicate a decrease in the skin friction coefficient with an increase in Kn numbers according to the slip effect similar to [67]. The rarefaction effect was notably more significant in the second and third cases compared to the scenario without obstacles. Among these cases, the third scenario with nine obstacles in the microchannel exhibited a superior reduction in the skin friction coefficient of the rarefied flow in the slip regime.

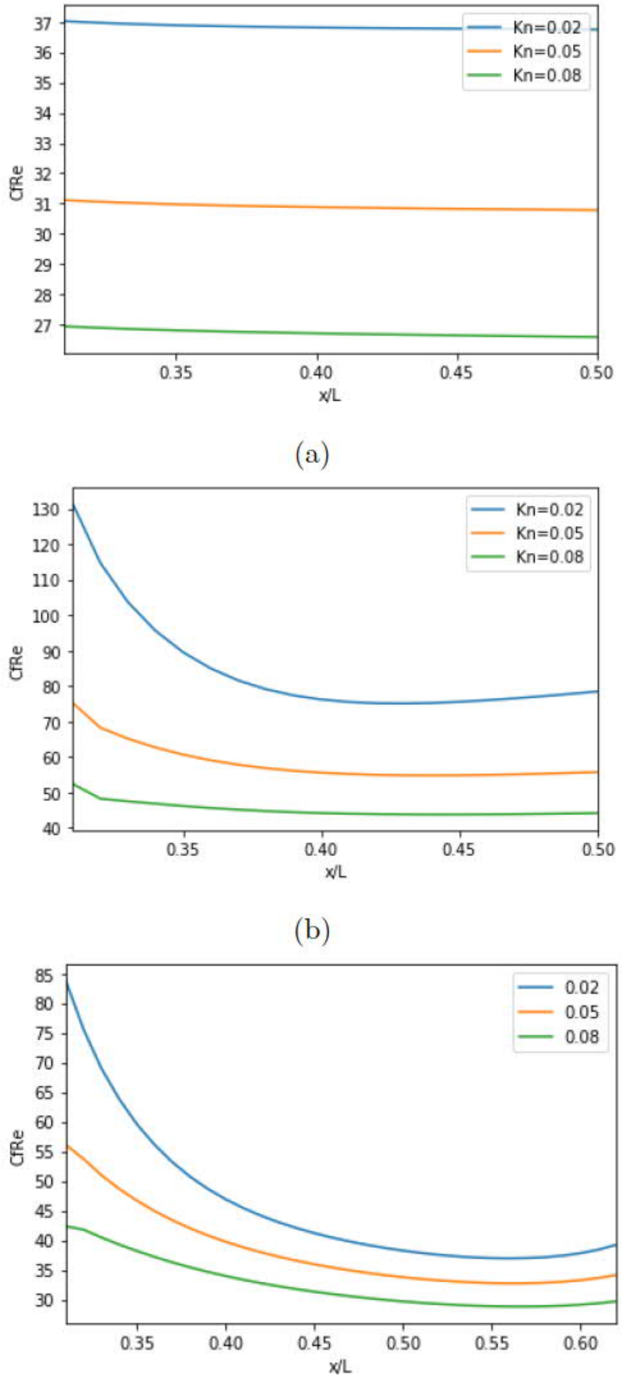

(a)

(b)

(c)

Figure 3.13: Effect of Knudsen number on the skin friction coefficient a: with no obstacle, b: with three obstacles;c: with nine obstacles

3.2.6 Slip velocity

Figures 3.14,3.15,3.16 illustrate the axial variation of velocity slip along the lower and upper wall for various Kn numbers. In the absence of obstacles, the velocity slip along the top and lower walls gradually decreases, Figure 3.14. In the presence of obstacles, the velocity slip continues to decrease and becomes divided into zones based on the obstacles presence. This decrease in velocity slip is a consequence of the reduction in velocity gradient at the wall [67] Figures 3.15 and 3.16. An augmentation in slip velocity occurs before the obstacle, followed by a dropping in slip velocity until it gets the minimal value at $x = 0.6$ for the upper wall and before $x = 0.4$ for the bottom wall in the second and third cases, Figures 3.15 and 3.16. The low value of velocity slip is associated with the second case, as depicted in Figure 3.16.

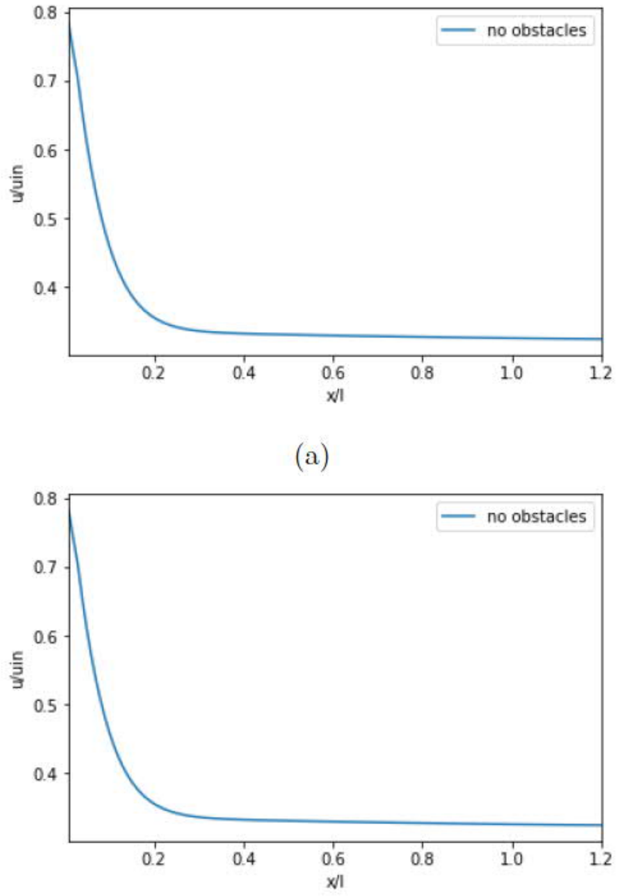

(a)

(b)

Figure 3.14: Velocity slip: Case without obstacles a: Upper wall ;b: Lower wall

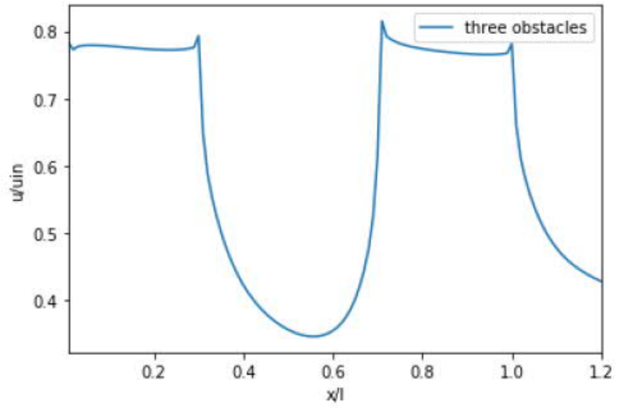

(a)

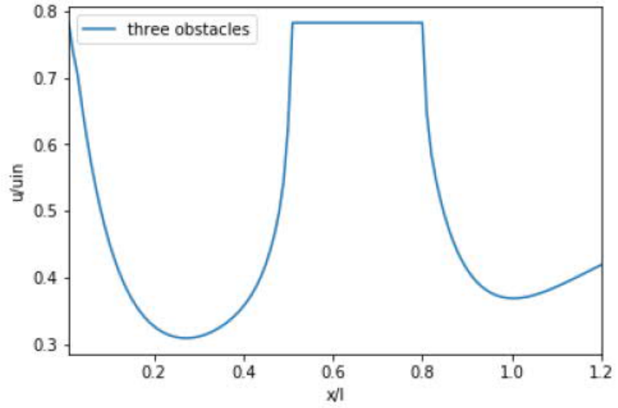

(b)

Figure 3.15: Velocity slip: Case with three obstacles a: Upper wall; b: Lower wall

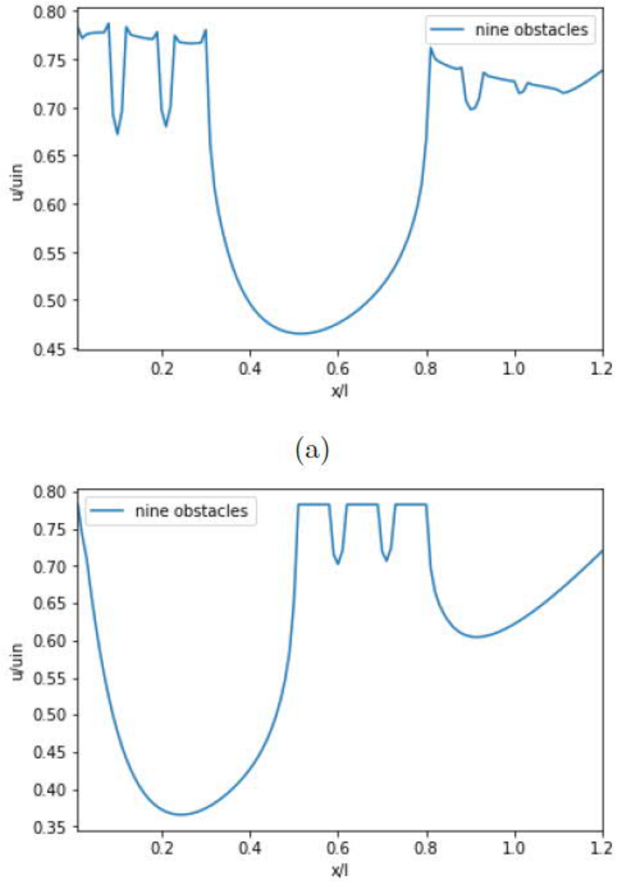

(a)

(b)

Figure 3.16: Velocity slip: Case with nine obstacles ;a: Upper wall; b: Lower wall

3.2.7 Temperature jump

Figures 3.17,3.18,3.19 show the temperature jump along the upper and lower walls of the MC as a function of the Knudsen number. In the absence of obstacles, the temperature jump increases rapidly in the developing region. Figure 3.18. In the case of obstacles, the jumping temperature decreases, and a lower temperature jump is observed next to the obstacle. It rises when passing the obstacle. Nevertheless, in both cases, with and without obstacles, the rarefaction effect does not exert any notable influence on temperature jump along the top and bottom walls of the MC for all Knudsen number values. Our study did not find any significant impact of the rarefaction effect on temperature jump in the slip regime of rarefied flow compared to other research such as [67].

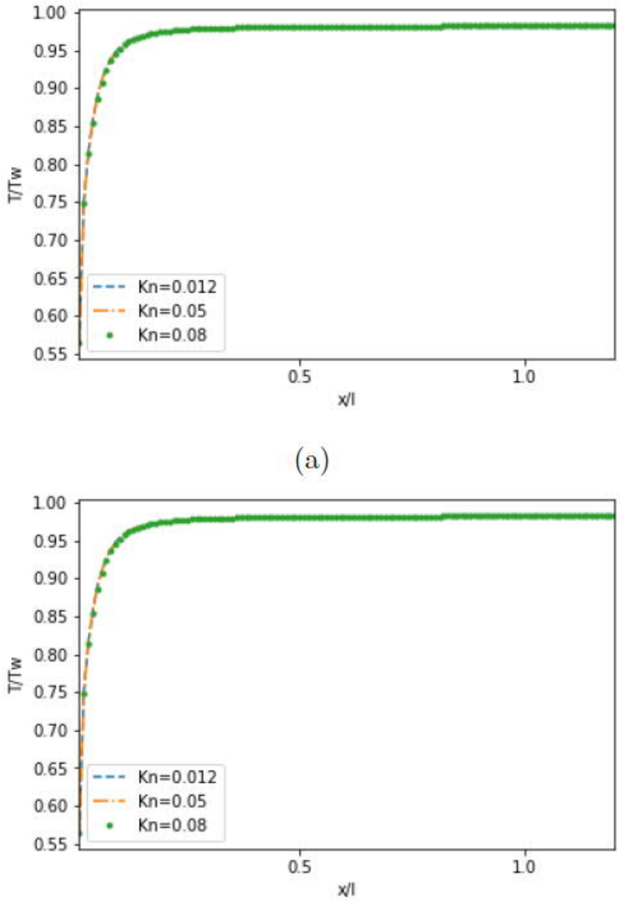

(a)

(b)

Figure 3.17: Effect of Kn number on the temperature jump: Case with no obstacles. a: Upper wall; b: Lower walll

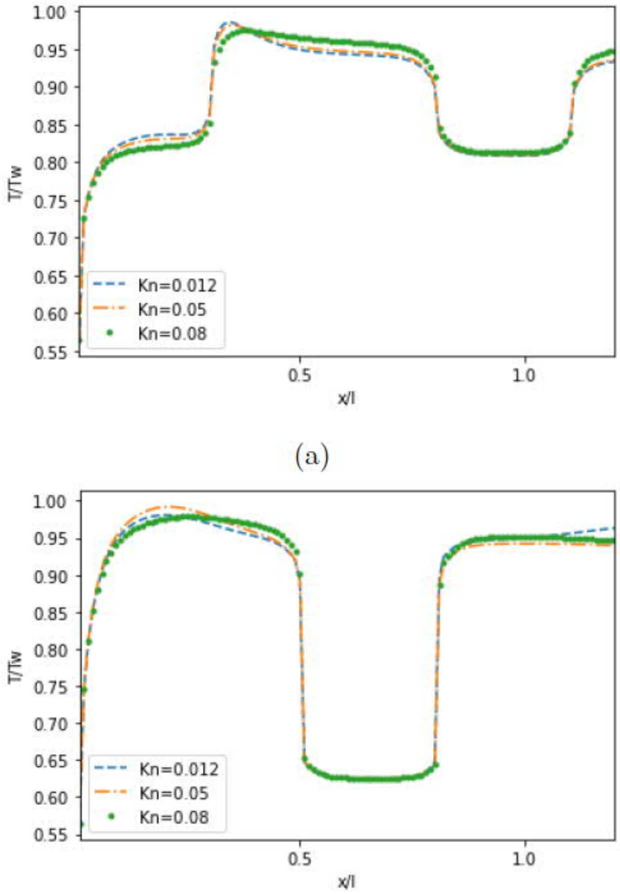

(a)

(b)

Figure 3.18: Effect of Kn number on the temperature jump: Case with three obstacles. a: Upper wall; b: Lower wall.

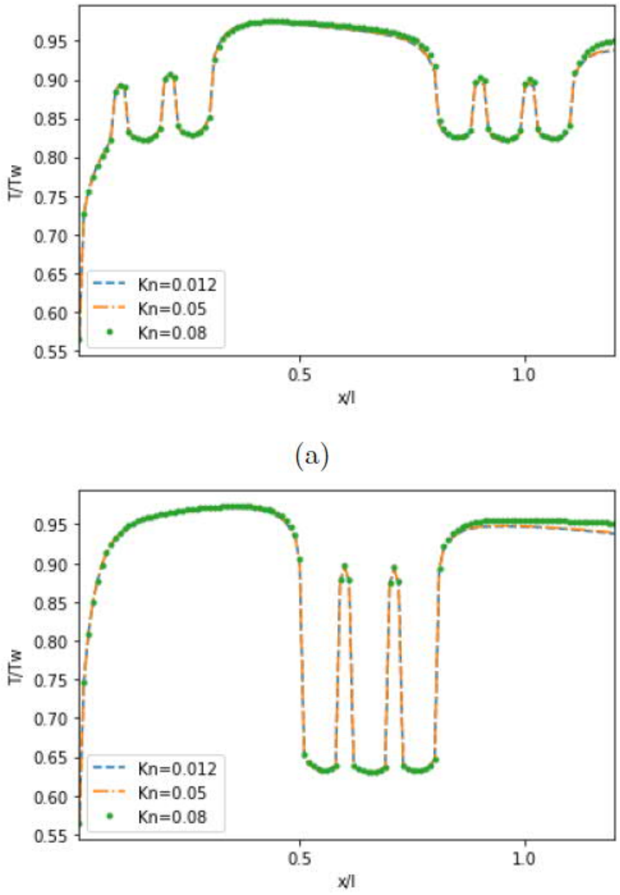

(a)

(b)

Figure 3.19: Effect of Kn number on the temperature jump: Case with nine obstacles. a: Upper wall; b: Lower wall.

3.3 Second section

3.3.1 Problem statement

This second study section focuses on analyzing the properties of convective laminar flow in a 2D MC with baffles (see Figure 3.20). In this case, the MC takes on a rectangular shape with dimensions of length L and height H. In the initial configuration, three square-shaped baffles, each measuring a length a, were strategically placed along the upper wall of the MC (as illustrated in Figure 3.20a). In the second scenario, three similar baffles were installed on the lower MC wall. (see Figure 3.20b). Lastly, in the third scenario, the study considered placing six baffles symmetrically on the microchannel's upper and lower walls, with three baffles on each side (refer to Figure 3.20c). The fluid's velocity and temperature at the MC inlet were kept constant at u_{in} and T_{in} , respectively. The walls of the MC remain stationary, and their temperature is maintained constant, equal to ten times T_{in}.

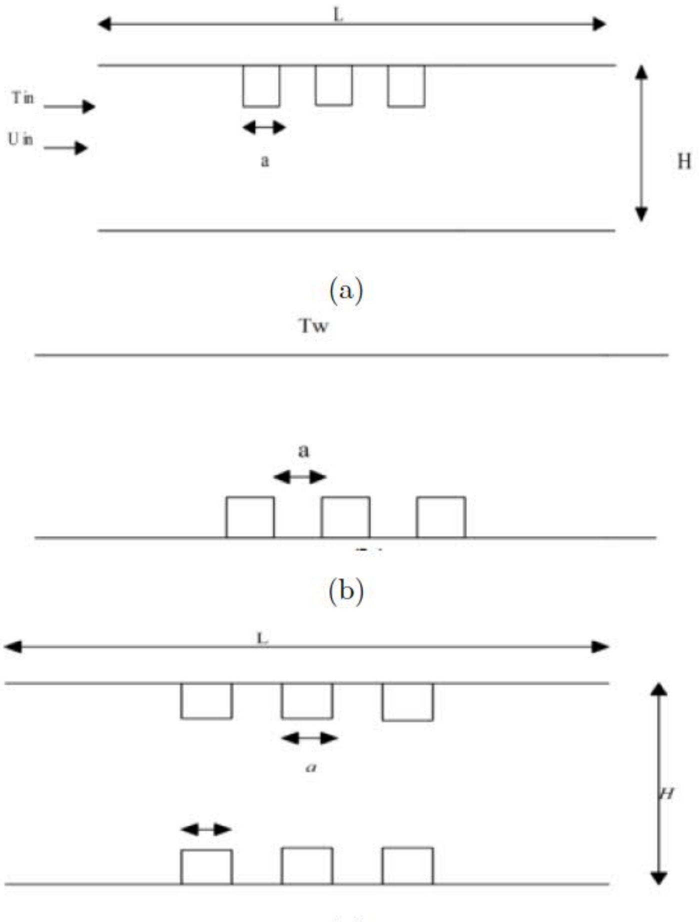

(a)

(b)

(c)

Figure 3.20: Microchannel configuration a: obstacles in top; b: obstacles in bottom; c: obstacles on two sides

3.3.2 Velocity distributions

In Figure 3.21, velocity distribution is shown for Kn numbers ranging from 0.012 and 0.08 with baffles applied in the first case. The figures illustrate that as Kn increases, there is a notable decrease in velocity, with the highest velocities observed at the center of MC at the exit. Furthermore, the findings indicate a more pronounced velocity gradient away from the sides of the MC.

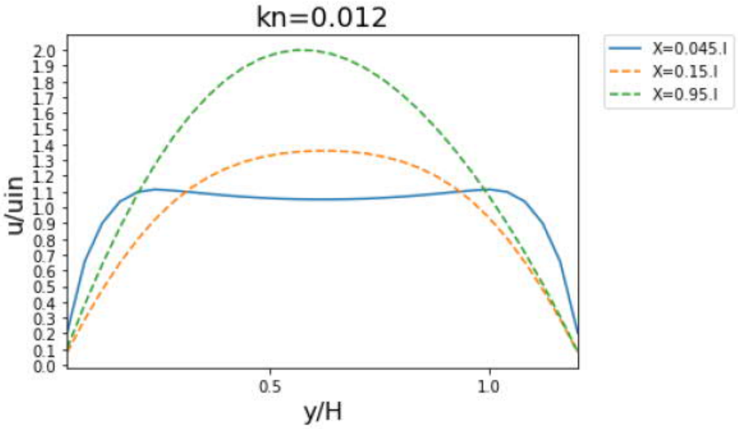

(a) $K0.012$

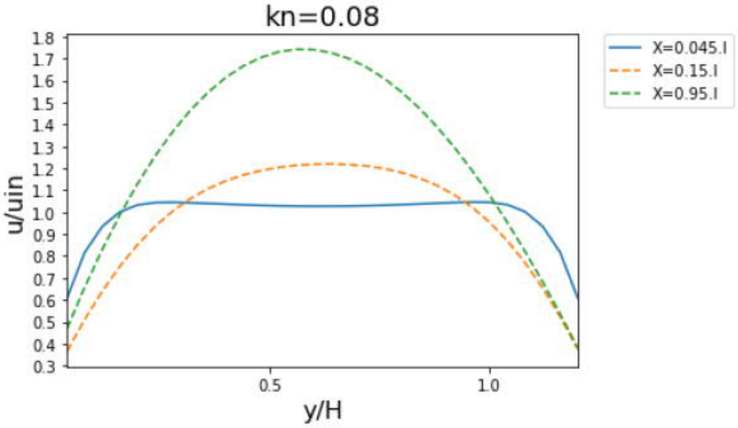

(b) $K, n = 0.08$

Figure 3.21: Velocity distribution in function of Knudsen for obstacles in a top wall

The velocity distribution in the second state with bottom baffles is presented in Figure 3.22. Compared to the first case with top baffles, velocity values show a rapid reduction with higher Kn values. The velocity profiles demonstrate that the speed consistently achieves its maximum in each MC's middle.

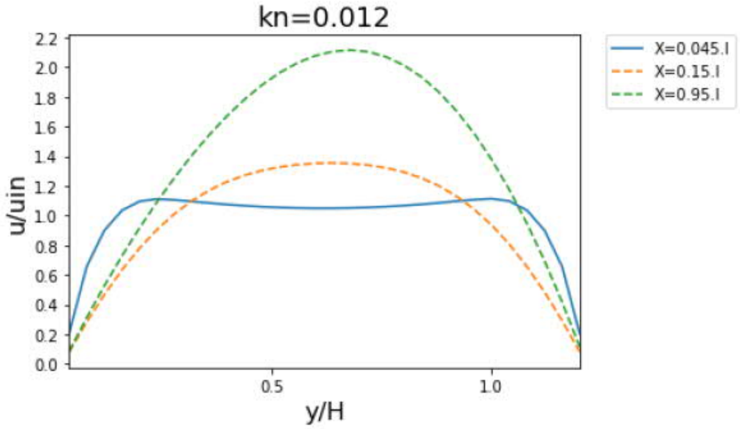

(a) $Kn = 0.012$

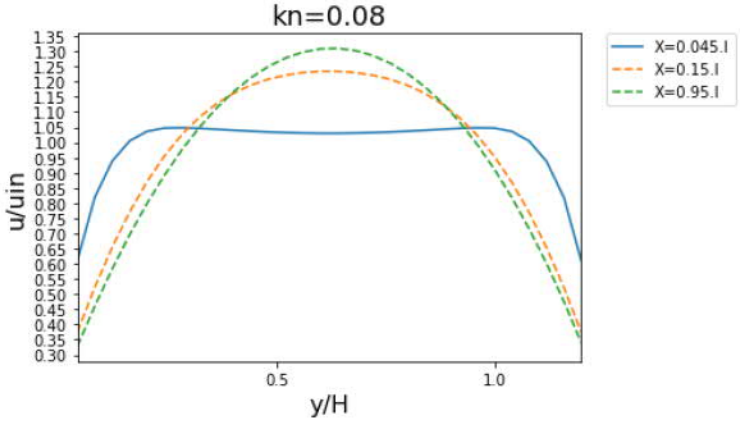

(b) $Kn = 0.08$

Figure 3.22: Velocity distribution in function of Kn for obstacles in a bottom wall.

Velocity distribution in the presence of baffles on both MC walls is displayed in Figure 3.23, indicating a velocity reduction with higher Kn values; the figures reveal the highest velocity occurring at the center of the duct, specifically at the exit, as in previous cases.

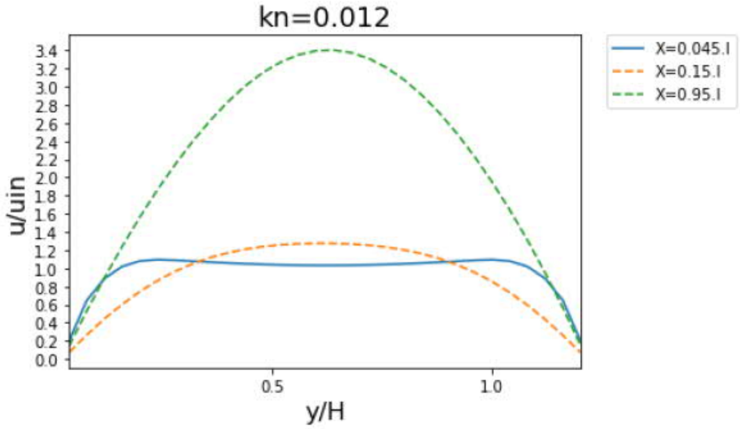

(a) $Kn = 0.012$

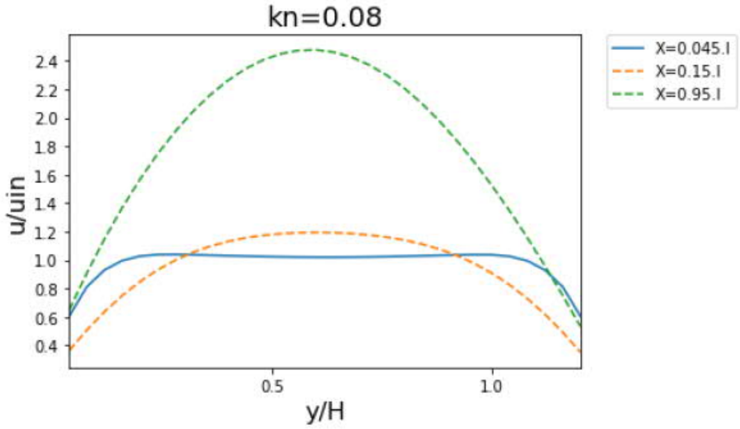

(b) $Kn = 0.08$

Figure 3.23: Velocity distribution in function of Knudsen for obstacles in both wall.

3.3.3 Temperature distribution

Figure 3.24 displays temperature distribution profiles for the same range of Kn numbers, with obstacles in the first case, including baffles on the upper wall. The results indicate a diminution in temperature values with Kn number augmentation, particularly near the walls at $x = 0.045.l$, and $x = 0.15.l$. Nevertheless, the microchannel's center shows lower temperature values.

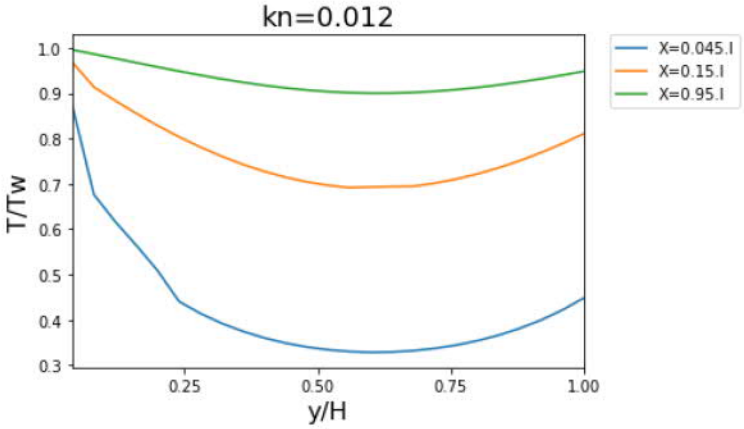

(a) $Kn = 0.012$

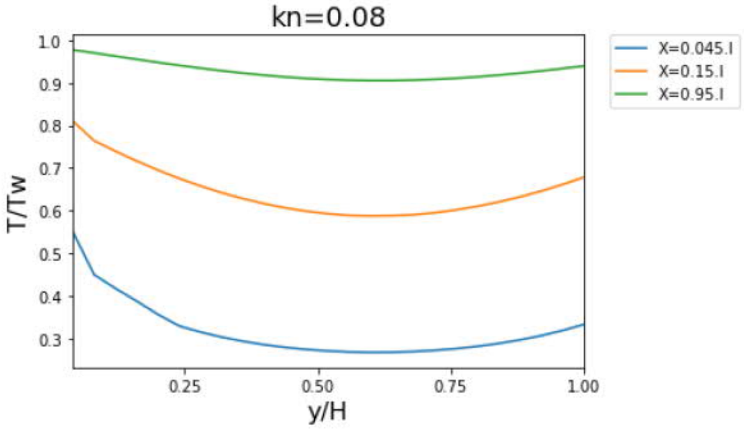

(b) $Kn = 0.08$

Figure 3.24: Temperature distribution in function of Knudsen for obstacles in a top wall.

Figure 3.25 displays the horizontal temperature distribution evaluation based on Knudsen under the conditions of lower obstacles. As the Kn increases, the temperature decreases, reaching its maximum near the wall and its minimum in the center area of the MC, as observed in the first case.

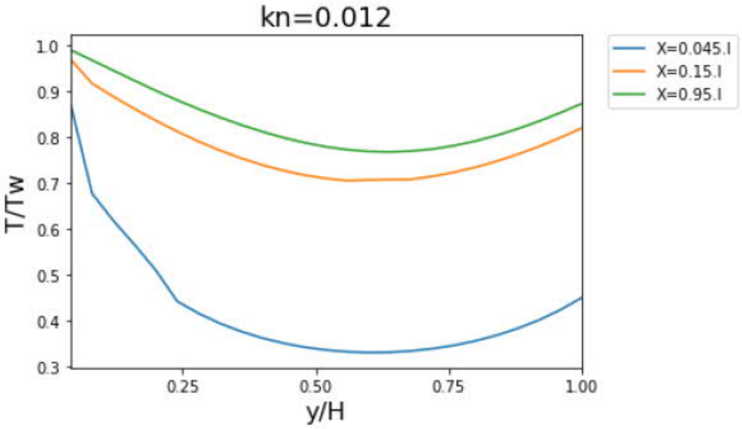

(a) $Kn = 0.012$

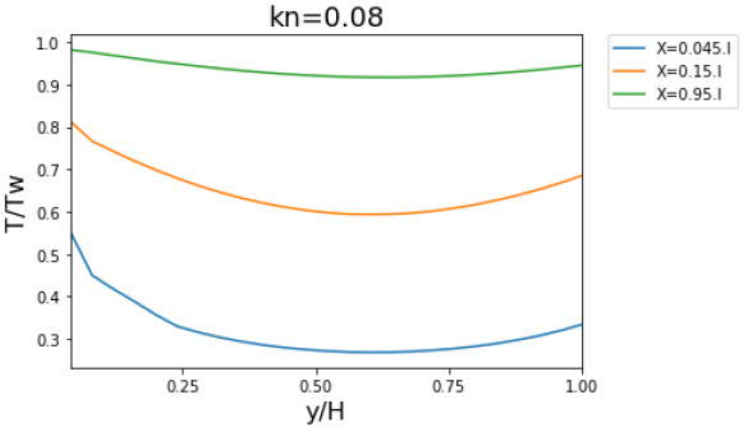

(b) $Kn = 0.08$

Figure 3.25: Temperature distribution in function of Kn for obstacles in a bottom wall.

Figure 3.26 displays the temperature plots where baffles are present on both MC walls, and the same range of Kn number changes, indicating a temperature reduction as the Kn values increase.

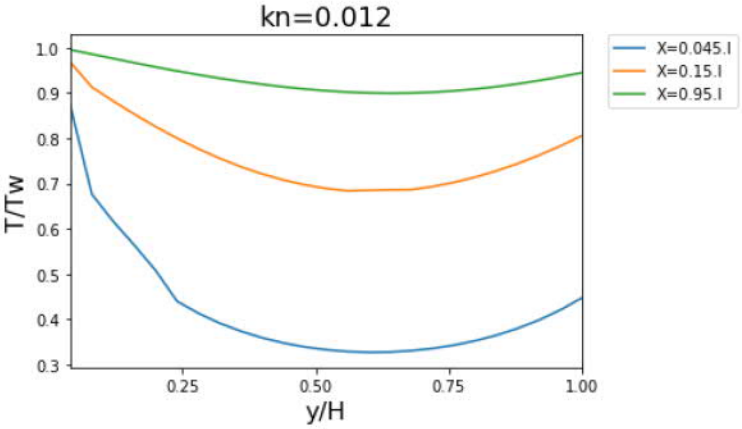

(a) $Kn = 0.012$

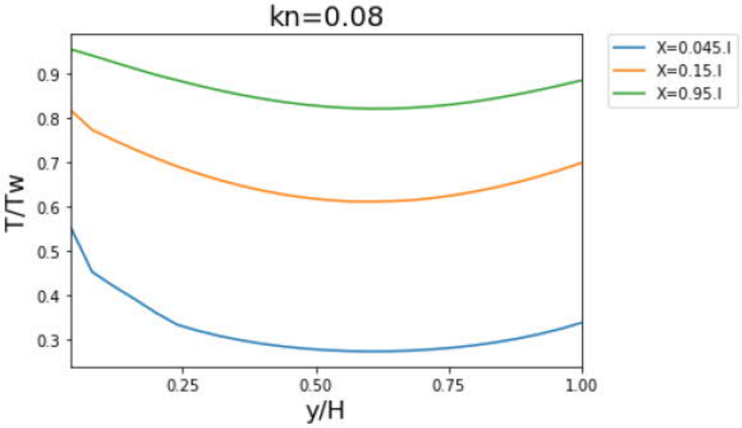

(b) $Kn = 0.08$

Figure 3.26: Temperature distribution in function of Kn for obstacles in both wall.

3.3.4 Nusselt number

Nusselt numbers are plotted against Kn values ranging from 0.02 to 0.08 in Figure 3.27; the results indicate a decrease in Nusselt profiles across all three cases as the Kn increase. Furthermore, a slight decrease in heat transfer is seen along the MC for each Kn number. The outcomes indicate that convection diminishes and conduction increases at the end of the MC.

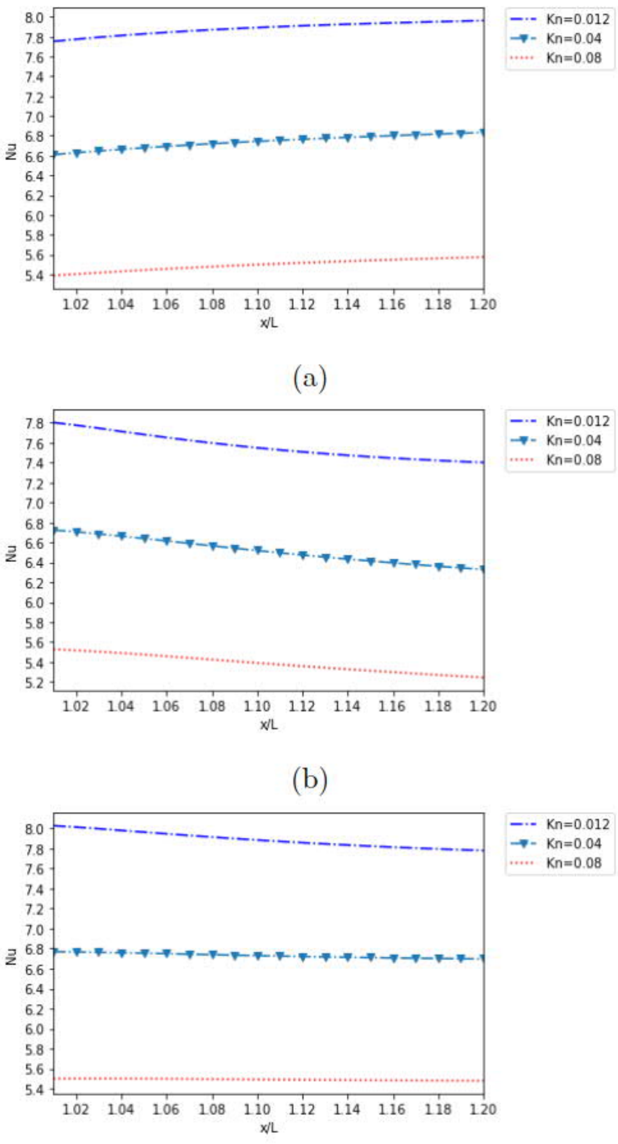

(a)

(b)

(c)

Figure 3.27: Effect of Knudsen number on Nusselt number; a: on top wall, b: On bottom wall, c: On both walls.

3.3.5 Skin friction coefficient

Figure 3.28 illustrates the variation of the skin friction coefficient C_f along the MC in Kn numbers ranging from 0.012 to 0.08, with C_f decreasing as the velocity gradient decreases. Nevertheless, the C_f attains higher values at the inlet in all cases. Additionally, the lower values of C_f are reached in scenarios where baffles are positioned on both sides of the MC with high Kn numbers.

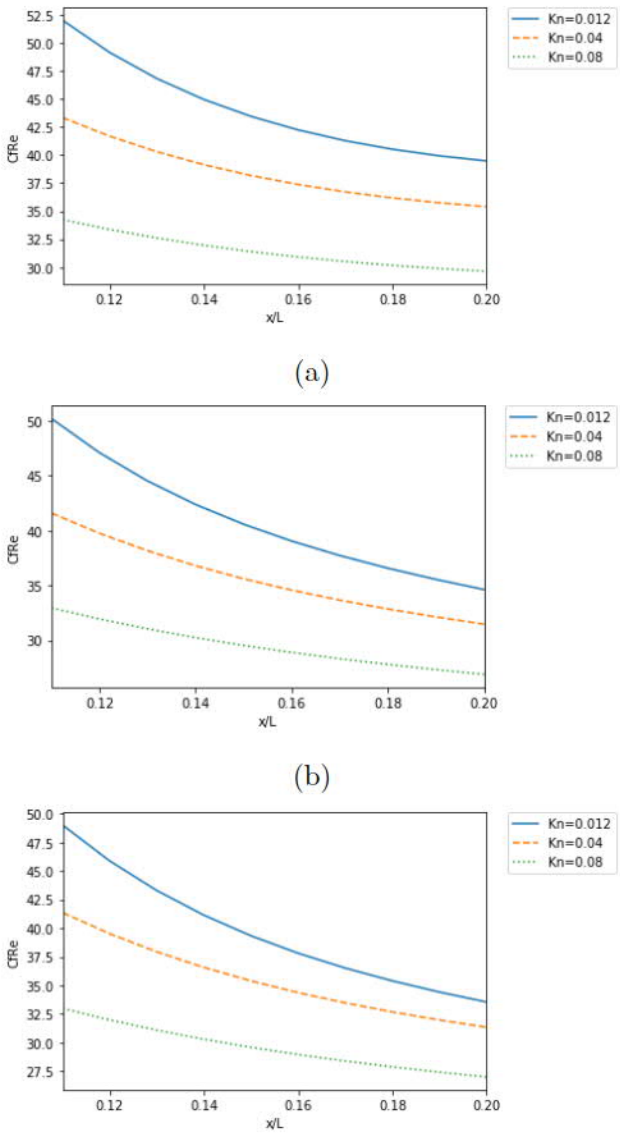

(a)

(b)

(c)

Figure 3.28: Effect of Knudsen number on Nusselt number a: with no obstacle, b: with three obstacles, c: with nine obstacles

3.3.6 Slip velocity

Figure 3.29, 3.30, and 3.31 display the variation in slip velocity in the presence of baffles in the MC under different cases with an increase in Kn numbers; there is a corresponding rise in the slip velocity. In the initial configuration, the highest slip velocity is attained at the third obstacle. On the other hand, in the second setup, the slip velocity reaches its peak at the first obstacle. In the third case, the slip velocity achieves identical results on both sides, with the third obstacle on the upper wall and the first on the lower wall. The findings show that the slip velocity is affected by the rarefaction effect. The impact of rarefaction is significant and has a noticeable effect on the slip velocity, according to the findings.

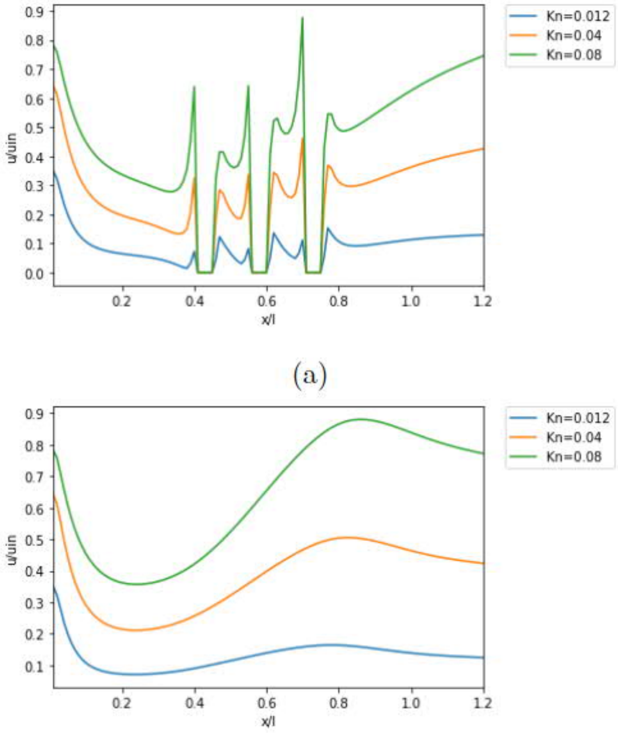

(a)

(b)

Figure 3.29: Velocity slip with obstacles at top; a: Upper wall ; b: Lower wall.

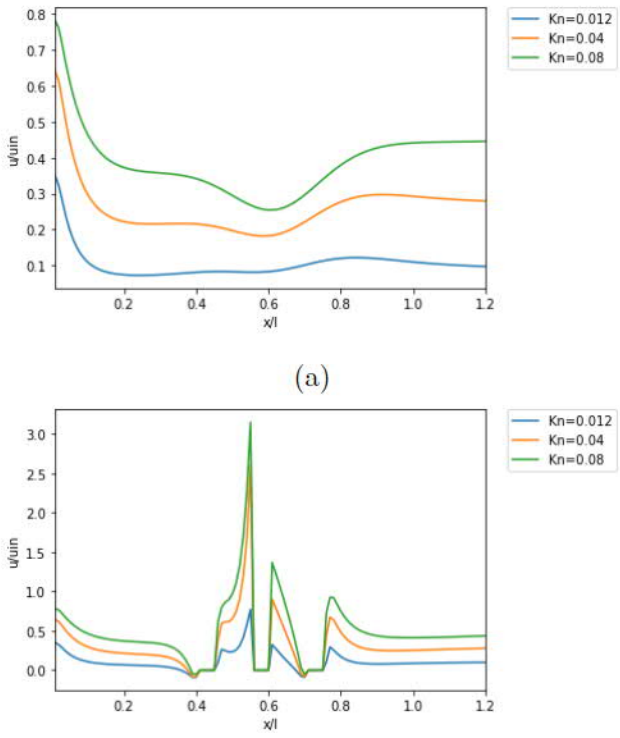

(a)

(b)

Figure 3.30: Velocity slip with obstacles in bottom; a: Upper wall; b: Lower wall.

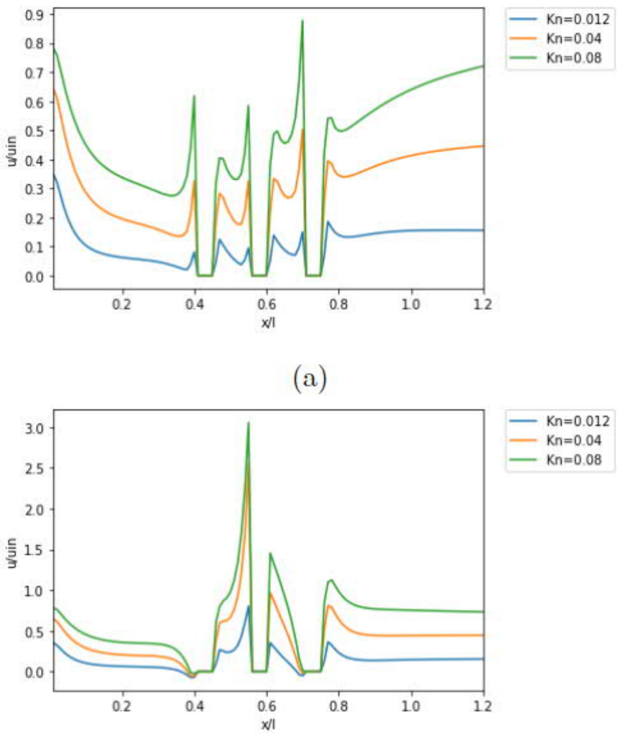

(a)

(b)

Figure 3.31: Velocity slip with obstacles on two sides; a: Upper wall ;b: Lower wall.

3.3.7 Temperature jumps

The effect of Kn numbers on temperature jumps is shown in Figures[3.32, 3.33, and 3.34]. At the microchannel inlet, there is a rapid increase in temperature jump, and remains relatively steady across the MC. In addition, temperature jump decreased with Kn numbers augmentation along the microchannel in three cases. Moreover, the results reveal that the rarefaction effect is not predominantly near the obstacle level, regardless of whether it is positioned at the top or bottom wall, compared to other MC zones where a slight variation can be observed.

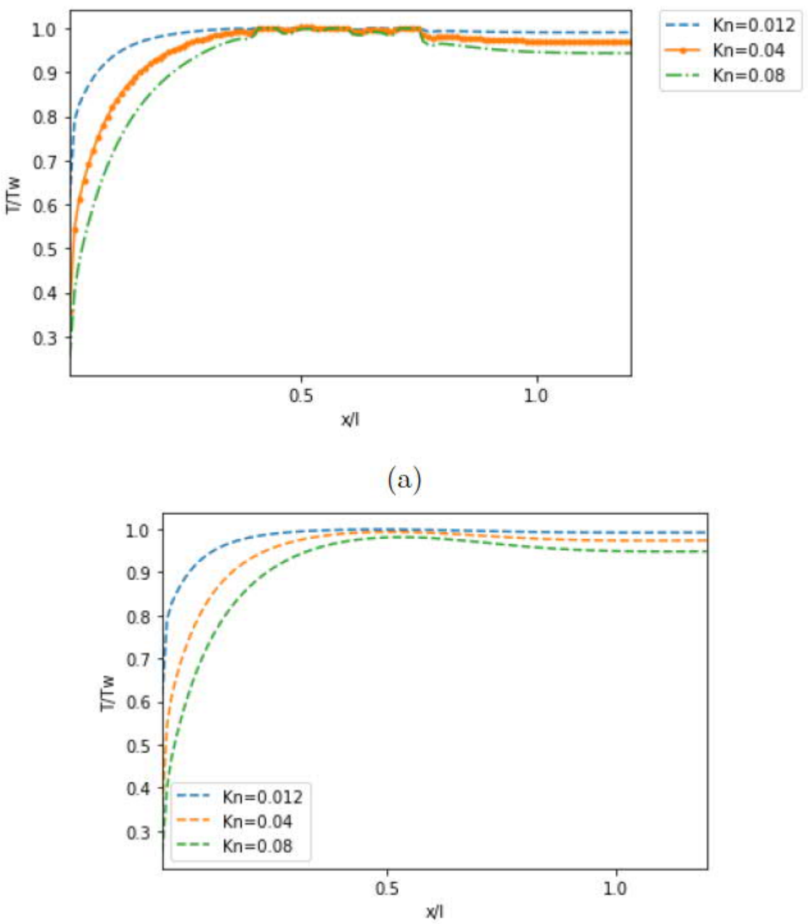

(a)

(b)

Figure 3.32: Effect of Knudsen number on the temperature jump. Obstacles in top a: Upper wall; b: Lower wall

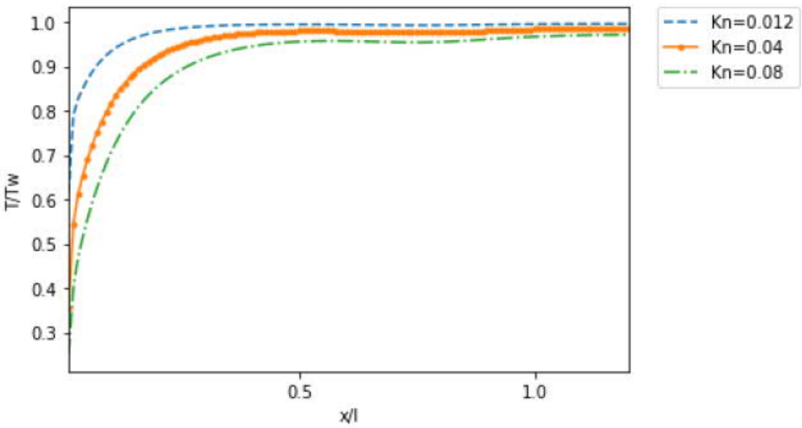

(a)

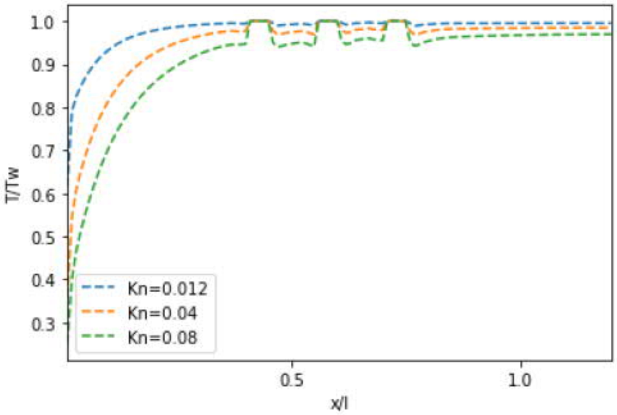

(b)

Figure 3.33: Effect of Knudsen number on the temperature jump. Obstacles in bottom; a: Upper wall; b: Lower wall.

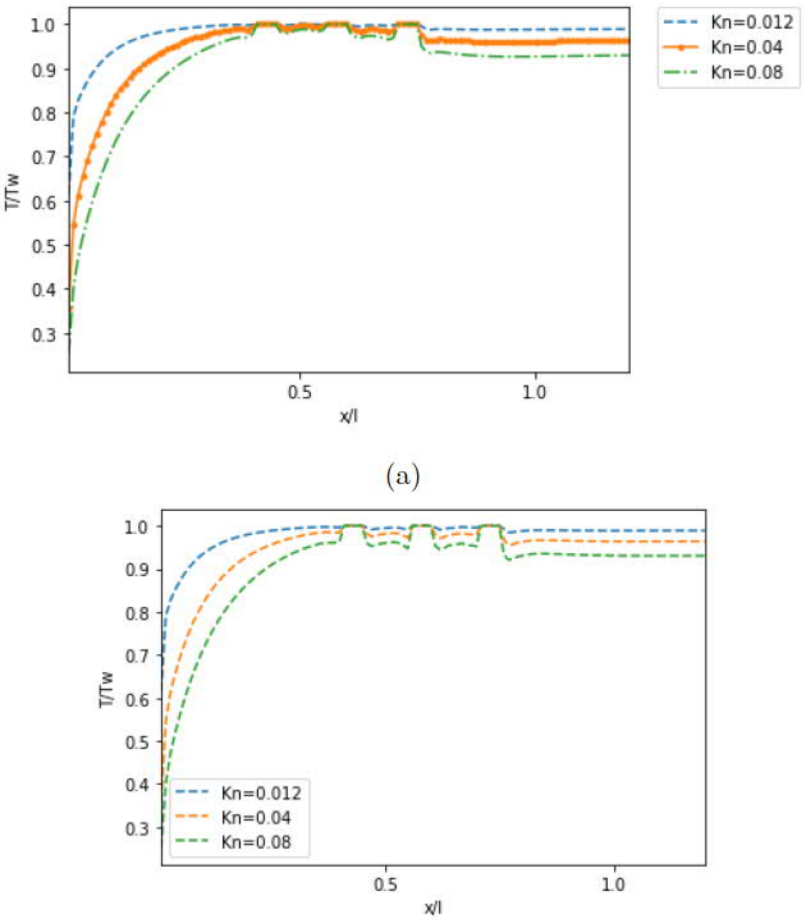

(a)

(b)

Figure 3.34: Effect of Knudsen number on the temperature jump. Obstacles on both sides a: Upper wall; b: Lower wall.

3.4 Third section

3.4.1 Problem statement

This study section examines the laminar fluid flow of forced convection heat transfer in a 2D rectangular microchannel with L length and H height employing the microchannel geometry depicted in Figure 3.35. The thermal LBM was using with a D_2Q_9 lattice to simulate the microchannel flow. The microchannel was subjected to a constant input velocity (u_{in}) and temperature (T_{in}). In contrast, the microchannel walls remained stationary and had a constant temperature (T_w) that was the same for both the upper and lower walls. In addition, the study explored the impact of introducing a nanofluid comprising copper nanoparticles dispersed in water into the microchannel flow. The thermophysical properties of the nanofluid used in the investigation are provided in Table 2.1.

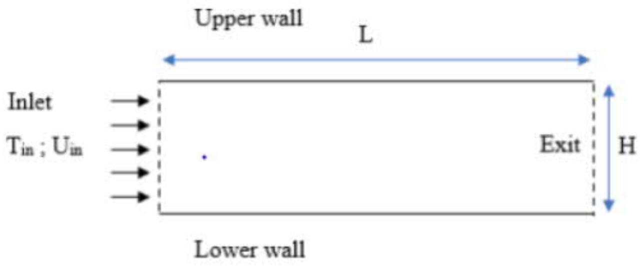

Figure 3.35: Schematic of the rectangular microchannel geometry used in the present study section.

3.4.2 The impact of Knudsen numbers on velocity and temperature distribution

The relationship between velocity and kn numbers is displayed in Figure 3.36 for values of Kn $0.02, 0.04$, and 0.08. As the kn number increases, the velocity decreases, reaching its maximum value in the center of the MC. This trend is particularly pronounced for kn numbers at or above 0.04 . The center of the MC exhibits a notably more substantial effect on the Knudsen numbers, similar to the results reported by [120], with tiny variations observed near the walls. These findings show that Knudsen numbers are critical in determining fluid behavior within the MC. Therefore, carefully considering Knudsen numbers is essential when designing microfluidic systems.

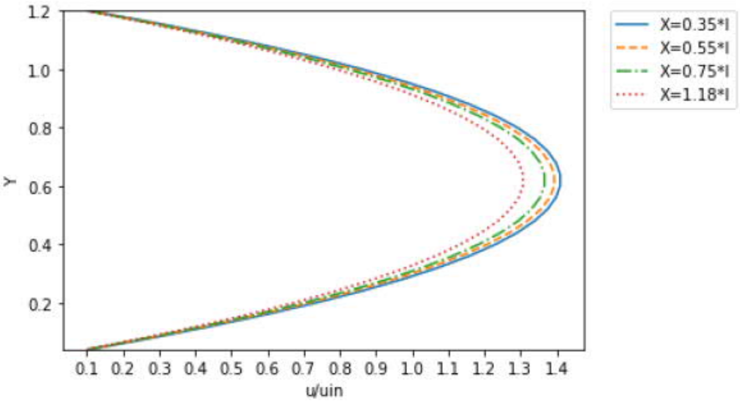

(a) $Kn = 0.02$

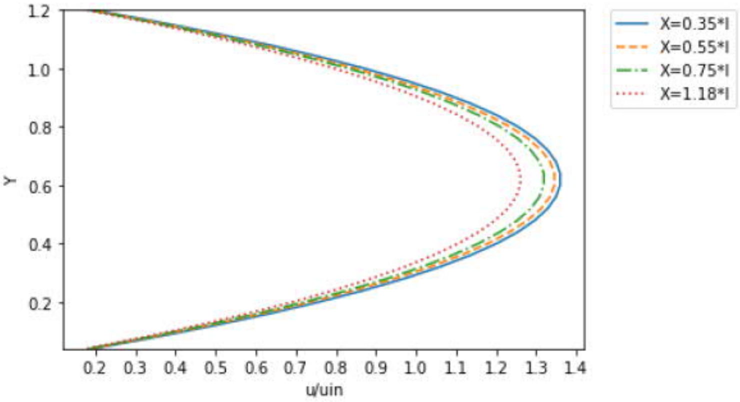

(b) $Kn = 0.04$

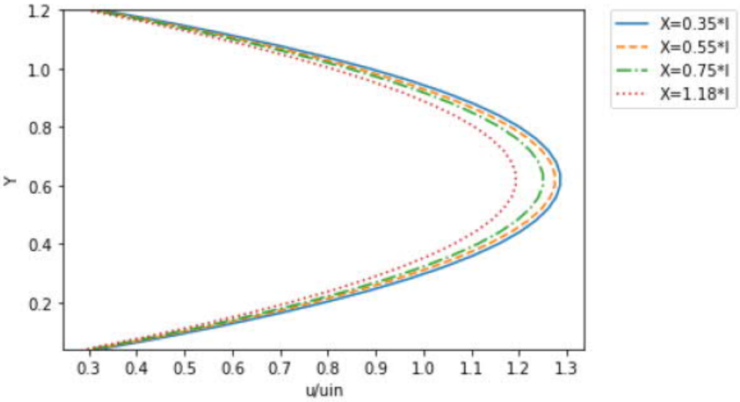

(c) $Kn = 0.08$

Figure 3.36: Visualization of the relationship between velocity and Knudsen numbers for $Re = 20$, and $\varphi = 0.02$, showcasing the velocity distribution for Kn values of (a)0.02, (b) 0.04, and (c) 0.08.

The temperature distribution in relation to Knudsen numbers is illustrated in Figure 3.37 for $Re = 20$, and $\varphi = 0.02$,. As the Kn number augments, the temperature decreases, with the most significant decrease observed near the wall. The lowest temperature value is achieved in the middle region of the microchannel. These findings suggest that Knudsen numbers notably impact microchannels' temperature distribution and should be considered when designing microfluidic systems. The results reveal a direct correlation between the dimensionless axial distance and the fluid temperature increasing as the former rises [58]. In conclusion, the findings underscore the importance of understanding how Knudsen numbers impact fluid behavior in MC's.

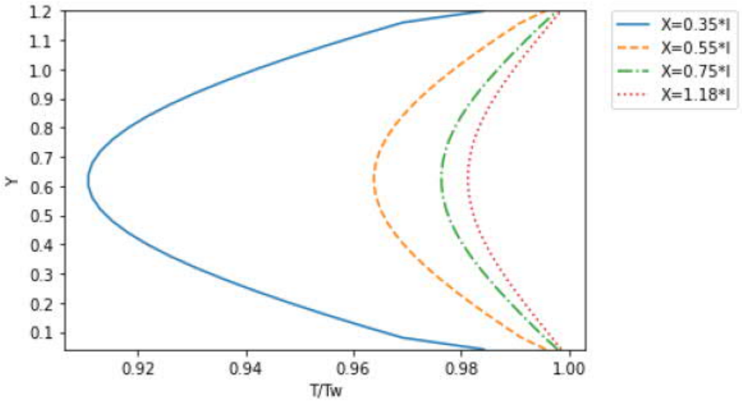

(a) $Kn = 0.02$

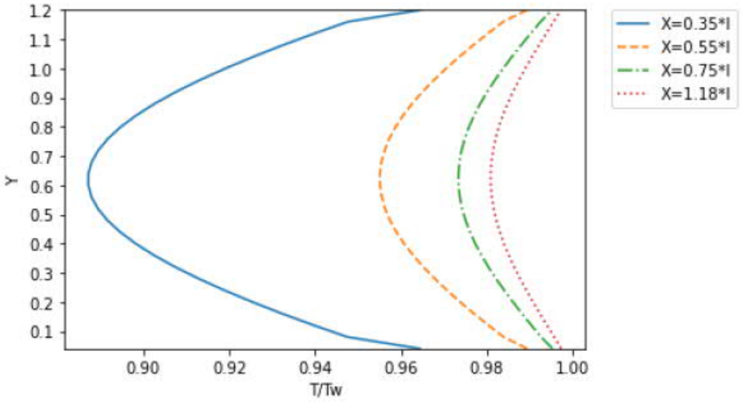

(b) $Kn = 0.04$

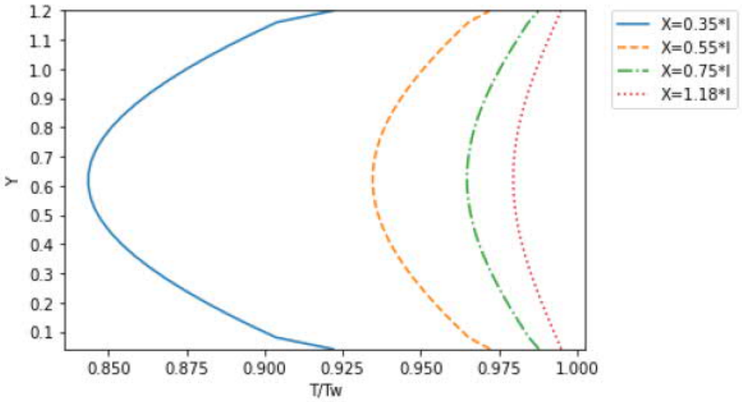

(c) $Kn = 0.08$

Figure 3.37: Visualization of the relationship between temperature and Knudsen numbers for $Re = 20$, and $\varphi = 0.02$, showcasing the temperature distribution for Kn values of (a)0.02, (b) 0.04, and (c) 0.08.

3.4.3 The influence of Reynolds numbers on fluid velocity and temperature distribution

Figure 3.38 illustrates the variation of horizontal velocity as a function of *Re* numbers at *Kn* of 0.05 and volume fraction (φ) of 0.02. The results indicate that the velocity increases along the length of the microchannel, reaching its maximum at the center. However, the velocity values decrease after reaching their peak. A slight increase in velocity is observed with the increase in *Re* numbers. Furthermore, the speed distribution profiles show an augmentation in velocity at the exit of the MC ($x = 1.18$) with an increase in Reynolds numbers. These findings underscore the significance of incorporating Reynolds numbers into the design and analysis of microfluidic systems, as they substantially impact the velocity distribution and flow behavior within the MC.

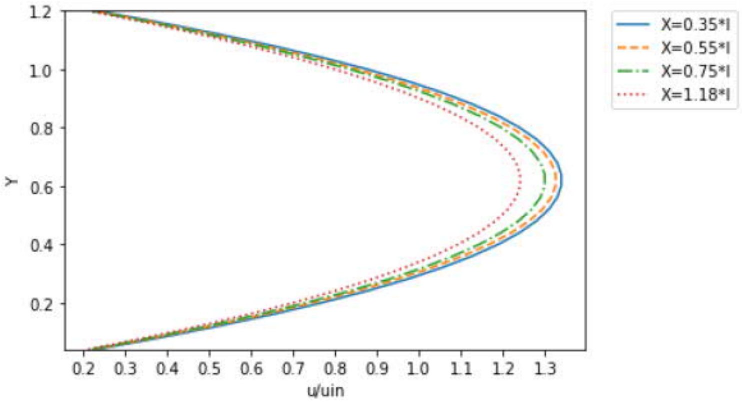

(a) $Re = 20$

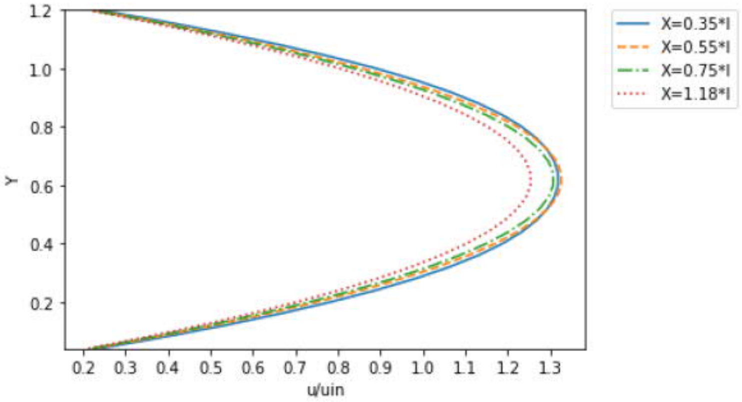

(b) $Re = 30$

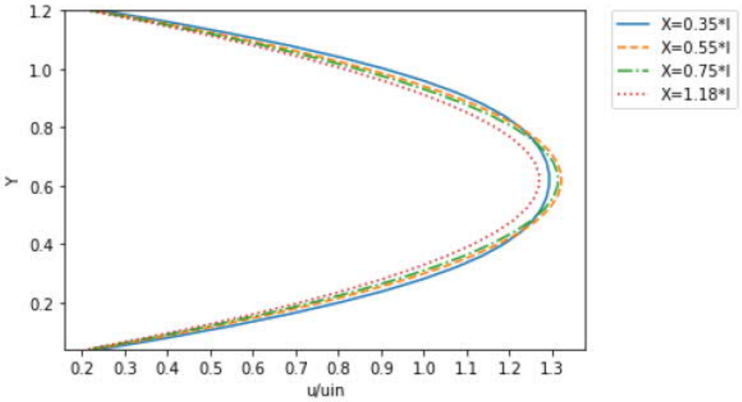

(c) $Re = 40$

Figure 3.38: Visualizing the correlation between Reynolds numbers and velocity distribution in microchannels for $Kn = 0.05$, and $\varphi = 0.02$

The temperature distribution in microchannels for different Re numbers ($Re = 20, 30$, and 40) is plotted in Figure 3.39. As the Reynolds number increases, the temperature near the walls decreases. In each curve, the lowest temperature value is observed at the center of the microchannel. The findings demonstrate that the influence of theRe is more pronounced in the center region compared to the proximity of the walls. Our results align consistently with those presented in [120], further supporting the observed relationship between the variables.

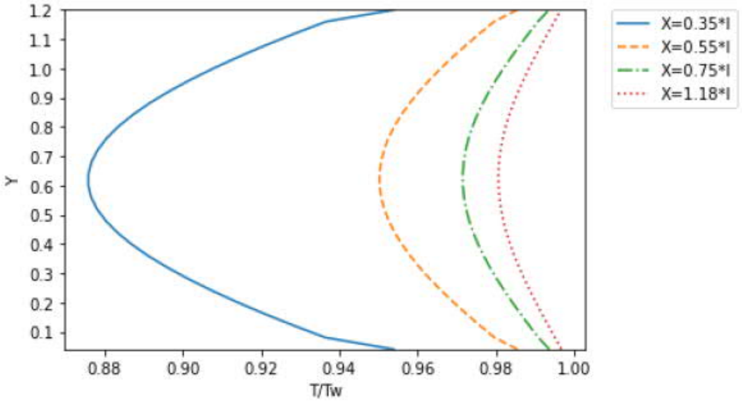

(a) $Re = 20$

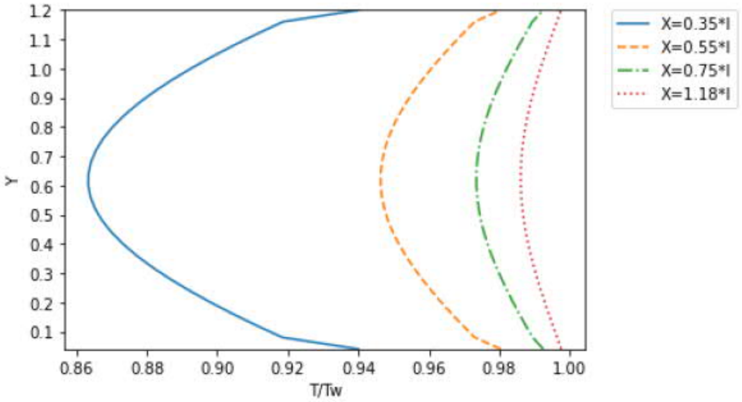

(b) $Re = 30$

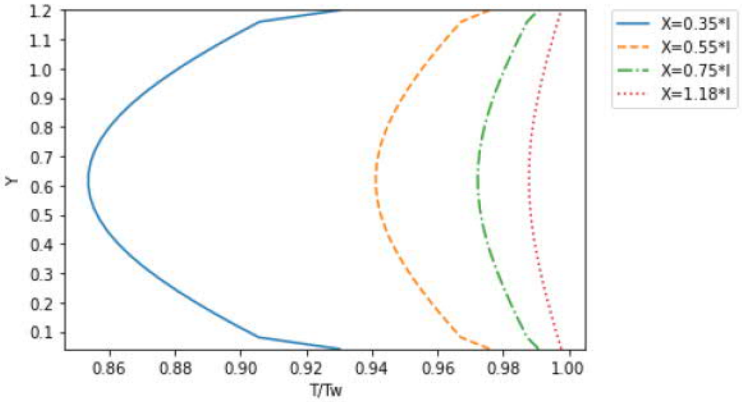

(c) $Re = 40$

Figure 3.39: Analyzing the relationship between temperature distribution and Re numbers for $Kn = 0.05$, and $\varphi = 0.02$

3.4.4 The influence of nanoparticle volume fraction on velocity and temperature distribution

Fluid velocity distribution plays a vital role in microfluidics, especially when manipulating fluid flow on a small scale. In this regard, Figure 3.40 visualizes the velocity distribution concerning the nanoparticle fraction volume. The graph illustrates that the velocity increases along the microchannel and reaches its maximum value at the middle region. Interestingly, the velocity distribution has no significant change with an increasing nanoparticle fraction volume. While this finding suggests that the nanoparticle volume fraction effect is not prominent in the velocity distribution, it is essential to note that other factors, such as particle size, shape, and surface properties, may have a more significant impact on the fluid flow behavior. These results offer valuable insights into the intricate interplay between fluid dynamics and nanoparticle properties within microfluidic systems. They emphasize the importance of conducting further investigations to understand these phenomena comprehensively.

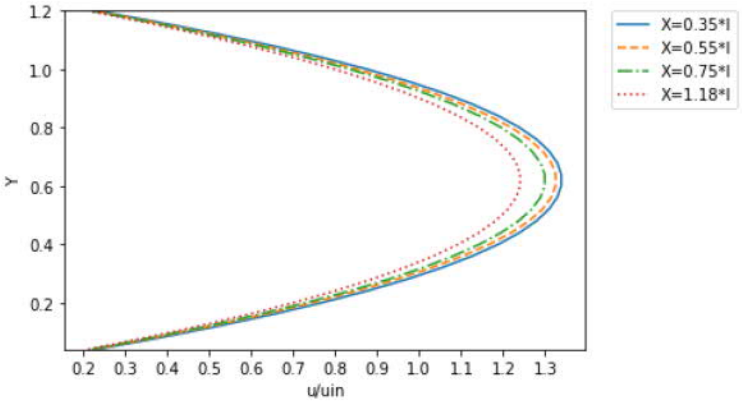

(a) $\varphi = 0.02$

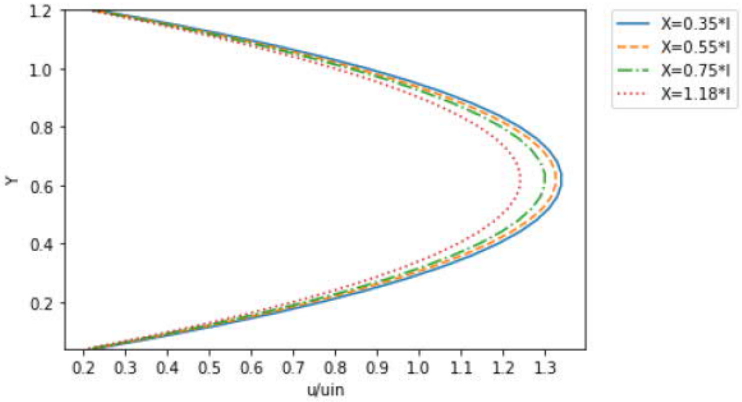

(b) $\varphi = 0.04$

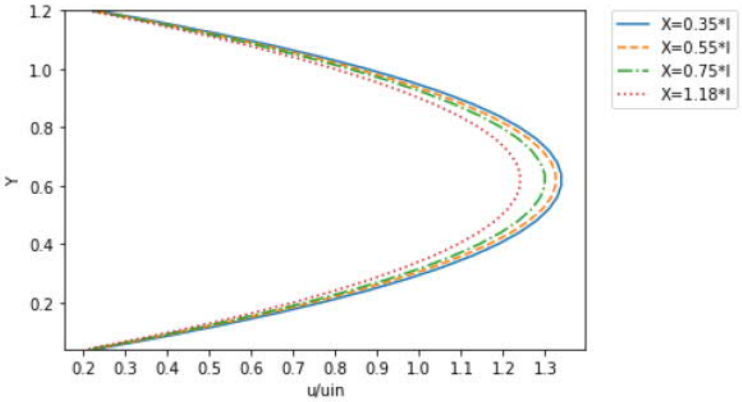

(c) $\varphi = 0.06$

Figure 3.40: Relationship between velocity distribution and nanoparticle fraction volume shown for $Re = 20$, and Kn=0.05.

Understanding the temperature distribution in microfluidic systems is crucial for various applications, including micro-electronics cooling, microreactors, and micro-nanofluidic devices. Figure3.41 illustrates the temperature distribution as a function of φ fraction at

$\varphi = 0.02, 0.04$, and 0.06. According to the illustration, heat is transferred from the fluid to the surroundings as the temperature drops down the microchannel and reaches its lowest value in the middle area. Interestingly, there is no significant variation in the temperature profile with an increasing φ fraction, similar to the velocity distribution. This finding indicates that the influence of the φ on the temperature distribution is insignificant, which could be attributed to the lower thermal conductivity of the nanoparticles compared to the fluid. However, it is crucial to acknowledge that the size and surface properties of the nanoparticles might also impact the heat transfer behavior in microfluidic systems. Therefore, further studies are necessary to explore and understand these factors in greater detail. To conclude, these findings provide essential insights into the complex interplay between fluid dynamics and heat exchange within microfluidic setups. These insights can be a valuable foundation for developing highly productive and proficient microfluidic instruments.

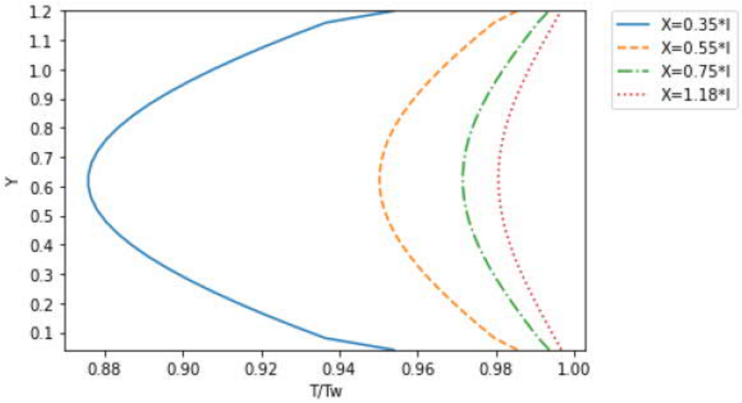

(a) $\varphi = 0.02$

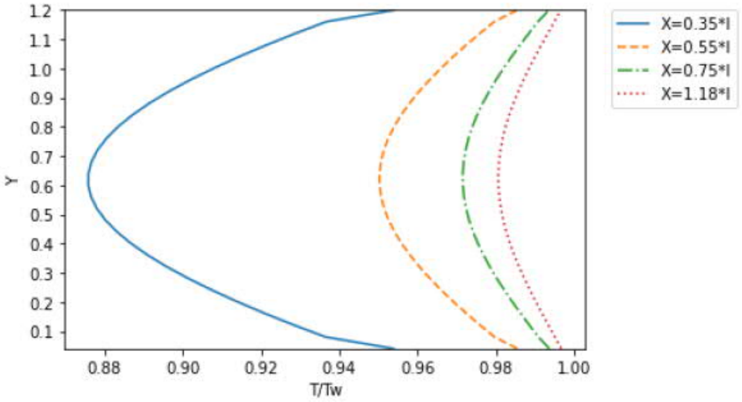

(b) $\varphi = 0.04$

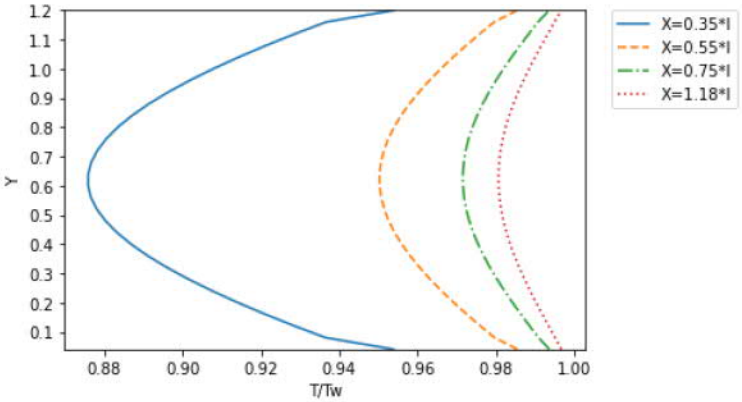

(c) $\varphi = 0.06$

Figure 3.41: Temperature distribution as a function of nanoparticle fraction volume, illustrated for $Re = 20$, and Kn=0.05.

3.4.5 Nusselt number

Figure 3.42 presents a comprehensive analysis of the impact of *Re* number, Kn number, and φ fraction on *Nu* numbers. The figure provides valuable insights into the intricate interplay among these essential parameters and facilitates a deeper understanding of heat transfer mechanisms in micro/nanoscale flows. These findings offer practical knowledge for designing and improving microfluidic devices to cater to a diverse range of technical applications. The variation of Nusselt numbers concerning Reynolds numbers of $20, 30$, and 40, at Knudsen number of 0.05 and nanoparticle volume fraction of 0.02, is illustrated along the microchannel as shown in Figure 3.42a. The findings show a decline in *Nu* number along the MC's developing region. The *Nu* numbers also increased, peaking near the inlet of the MC, as a result of the rising Reynolds numbers.

Figure 3.42b provides valuable insights into the relationship between *Kn* number and Nu numbers at a fixed *Re* number of 20 and a φ fraction of 0.02. The results demonstrate a clear and significant decrease in *Nu* numbers as *Kn* numbers increase along the length of the MC. Notably, the maximum *Nu* number is observed at a low Knudsen number of 0.02, with the peak value attained at the inlet of the MC.

In Figure 3.42c, the variation of Nusselt numbers with respect to nanoparticle volume fraction is presented along the microchannel at a fixed *Re* number of 20 and Knudsen number of 0.05. The *Nu* numbers drop along the microchannel while increasing with increasing fraction volume fraction due to thermal conductivity enhancement. This suggests that the inclusion of nanoparticles improves heat transfer performance, leading to higher Nusselt numbers

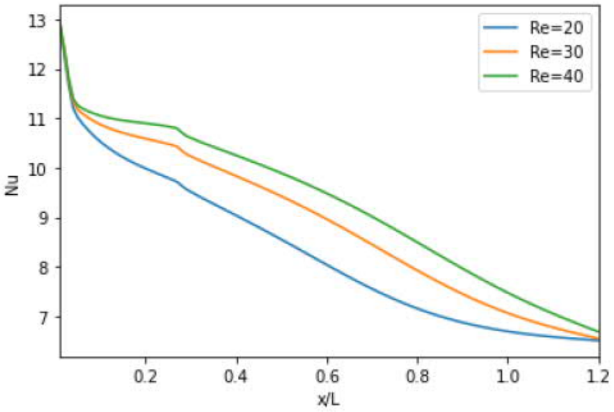

(a) for $Kn = 0.05$ and $\varphi = 0.02$

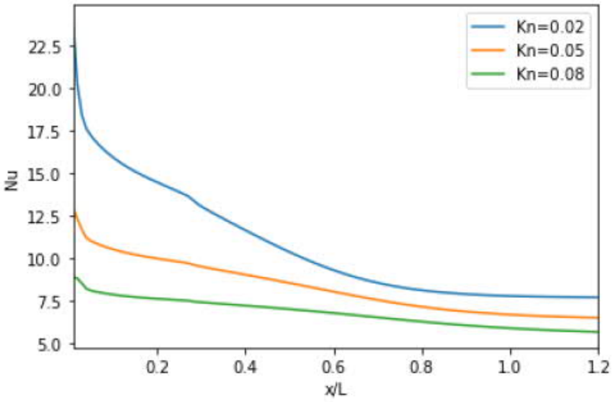

(b) for $Re = 20$ and $\varphi = 0.02$

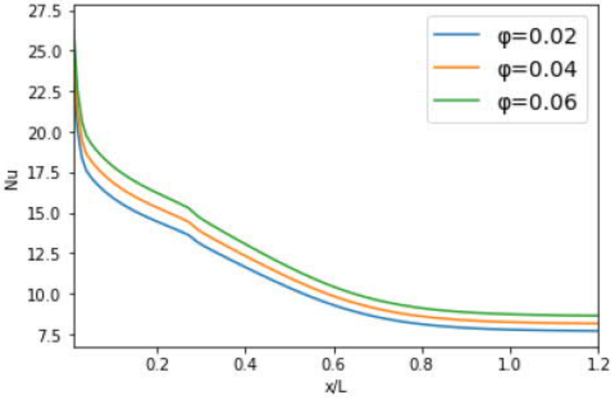

(c) for $Re = 20$ and $Kn = 0.05$

Figure 3.42: Nusselt numbers in function of (a) Reynold number, (b) Knudsen number, and (c) nanoparticle volume fraction.

3.4.6 Skin Friction coefficient

The relation between skin friction coefficient Cf and Re numbers is represented in Figure 3.43a, The Cf exhibits the highest value in the entrance region of the MC, and it gradually decreases along the length of the MC as the Re increase. For Knudsen numbers of $0.02, 0.05$, and 0.08, Figure 3.43b shows the fluctuation of the Cf coefficient along the MC. As the Knudsen numbers increase, there is a noticeable decline in the coefficient of friction (Cf) value. This decrease is a consequence of the reduction in the velocity gradient [67]. Figure 3.43c shows how the Cf coefficient changes with nanoparticle volume fractions (φ) of $0.02, 0.04$, and 0.08. As the rises, it can be seen that the Cf coefficient droping. The decline in the Cf continues until it reaches a point where it remains nearly constant along the rest of the MC. Additionally, it is noteworthy that the maximum skin friction coefficient value is consistently attained at the inlet of the MC.

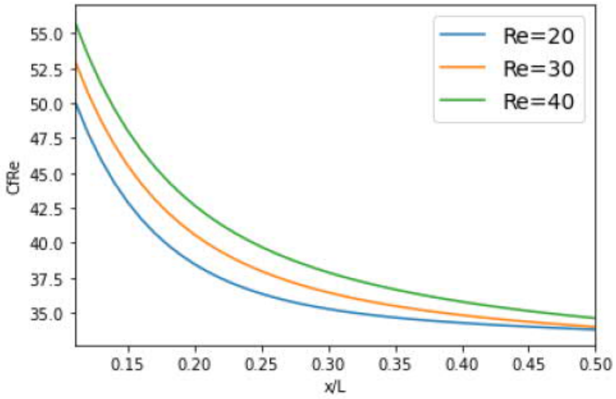

(a) for $Kn = 0.05$ and $\varphi = 0.02$

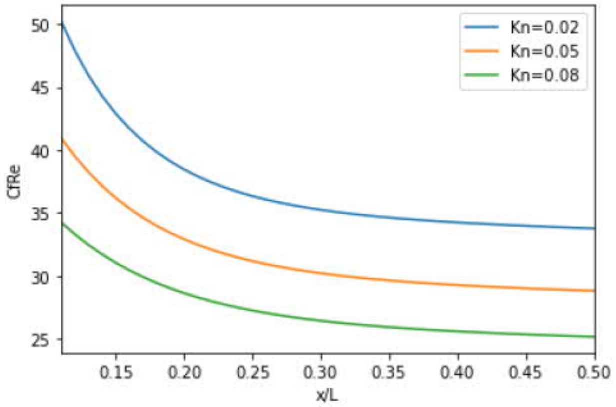

(b) for $Re = 20$ and $\varphi = 0.02$

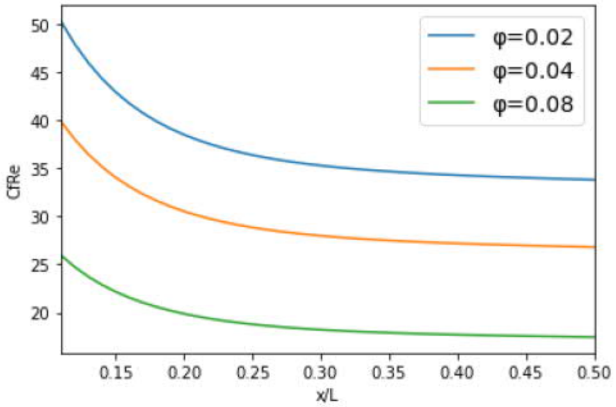

(c) for $Re = 20$ and $Kn = 0.05$

Figure 3.43: Skin friction coefficients in function of (a) Reynold number, (b) Knudsen number, and (c) nanoparticle volume fraction.

3.4.7 Velocity slip

Figure 3.44a presents the axial variation of slip velocity for $Re = 20, 30$, and 40 at $Kn = 0.02$ and $\varphi = 0.02$ on the upper MC wall. The slip velocity shows a rapid decrease in the entrance region and then maintains nearly constant throughout the length of the MC. Figure 3.44b demonstrates the slip velocity change along the MC for $Kn = 0.02, 0.04$, and 0.08 at $Re = 20$ and $\varphi = 0.02$ for the upper wall. In the entrance region, the slip velocity sharply decreases before remaining steady throughout the MC. Additionally, as Knudsen numbers increase, the slip velocity increases.

Figure 3.44c displays the velocity slip variation with nanoparticle volume fraction function for the top wall at $Re = 20$ and $Kn = 0.02$. The investigation's findings reveal a reduction in slip velocity as it progresses through the MC, confirming the effect of the slip boundary condition. This decrease in slip velocity results from the fluid's interactions with the MC walls. The results indicate that the decline in slip velocity can be attributed to the reduction in velocity gradient near the wall[67]. According to the outcomes, nanoparticle volume fraction in top MC walls does not impact the slip velocity.

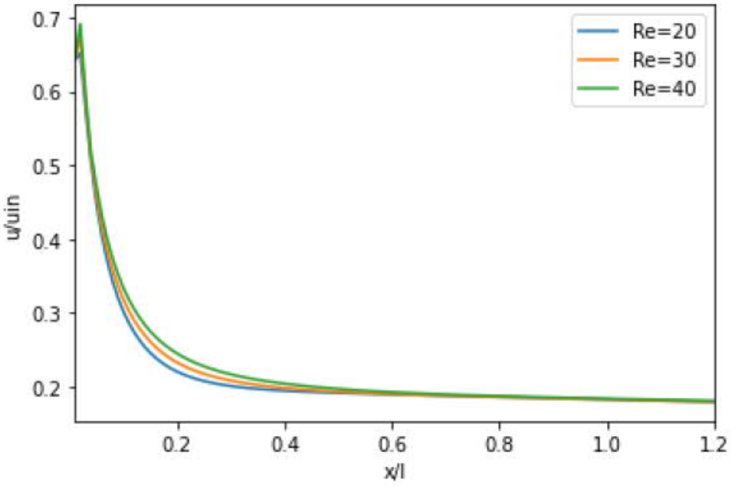

(a) for $Kn = 0.05$ and $\varphi = 0.02$

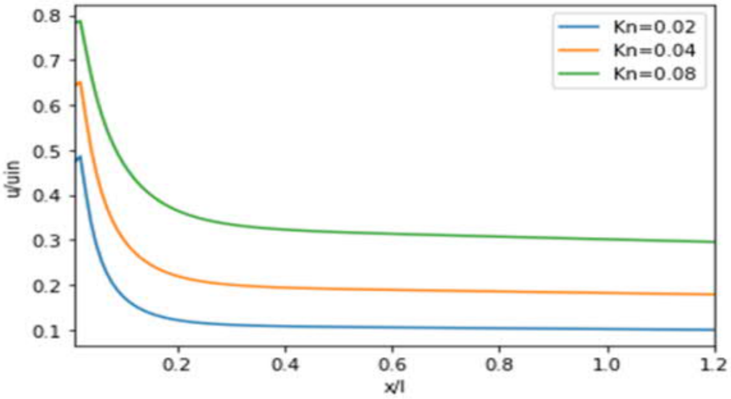

(b) for $Re = 20$ and $\varphi = 0.02$

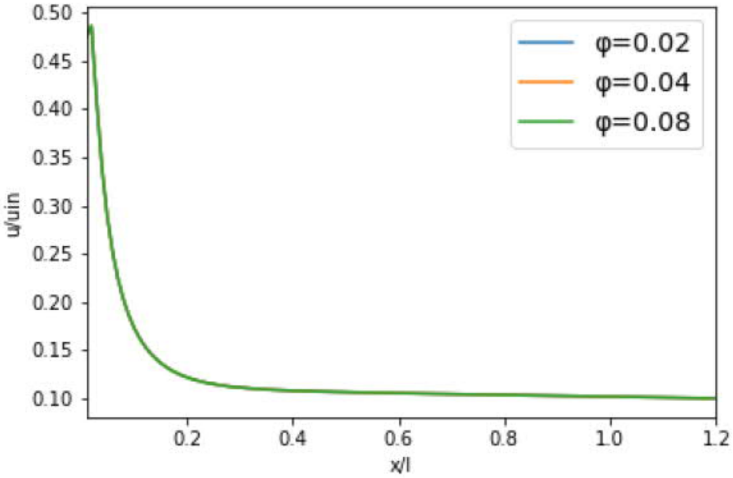

(c) for $Re = 20$ and $Kn = 0.02$

Figure 3.44: Velocity slip profiles in function of (a) Reynold number, (b) Knudsen number, and (c) nanoparticle volume fraction.

3.4.8 Temperature jump

Figure 3.45a shows the axial variation of temperature jump for $Re = 20, 30$, and 40. the temperature jump increases rapidly after the inlet, suggesting the presence of a significant thermal boundary layer. In the developing region, there is a slight reduction in the temperature jump with increasing Re number. However, the Reynolds number has minimal to no impact on the temperature jump behavior, as the temperature jump value remains constant throughout the rest of the MC. From these findings, we can conclude that the thermal boundary layer primarily regulates the temperature jump behavior in the MC. Furthermore, the effect of the Reynolds number on the temperature jump is mainly limited to the developing region. As a result, the findings of this study carry important implications for various microfluidic applications involving heat transfer. The insights gained into the behavior of temperature jump in microchannels under different flow conditions.

As a function of Knudsen numbers, Figure 3.45b depicts the change of temperature jump along the MC wall. The findings show a rapid increase in temperature jump in the entrance region near the wall. Interestingly, as the Kn number increases at the entrance region, the temperature jump decreases, suggesting a diminishing impact of the rarefaction effect on temperature jump. Furthermore, the temperature jump remains nearly constant along the developing area until the end of the MC, indicating that the rarefaction effect becomes no longer significant at the wall. The findings offer valuable insights into the behavior of temperature jump in microchannels with varying Knudsen numbers. They suggest that the rarefaction effect is more pronounced in the entrance region and diminishes as the flow develops along the microchannel. These insights hold important implications for various microfluidic applications involving heat transfer, as they help identify the areas where the rarefaction effect is significant. This knowledge can guide the design of more efficient microfluidic devices.

Figure 3.45c presents the variation of the temperature jump variation of the MC for different nanoparticle fractions. The results demonstrate a rapid increase in temperature jump in the entrance region, and this is followed by a nearly constant temperature jump along the developing area until reaching the exit of the MC. These observations suggest that the thermal boundary layer thickness is established at the entrance region, and the heat transfer behavior becomes fully developed as the flow progresses downstream. Additionally, the findings suggest that the nanoparticle volume fraction does not influence the temperature jump in the MC wall.

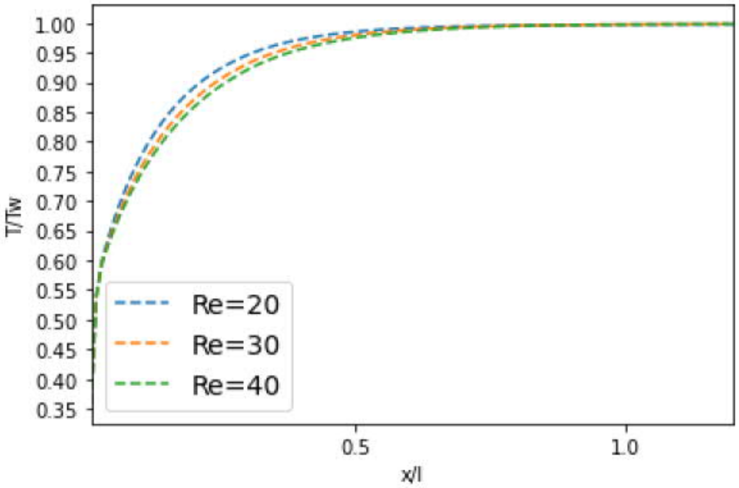

(a) for $Kn = 0.02$ and $\varphi = 0.02$

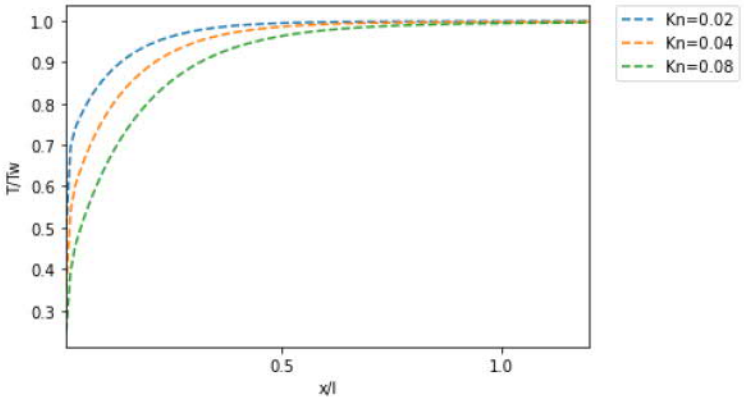

(b) for $Re = 20$ and $\varphi = 0.02$

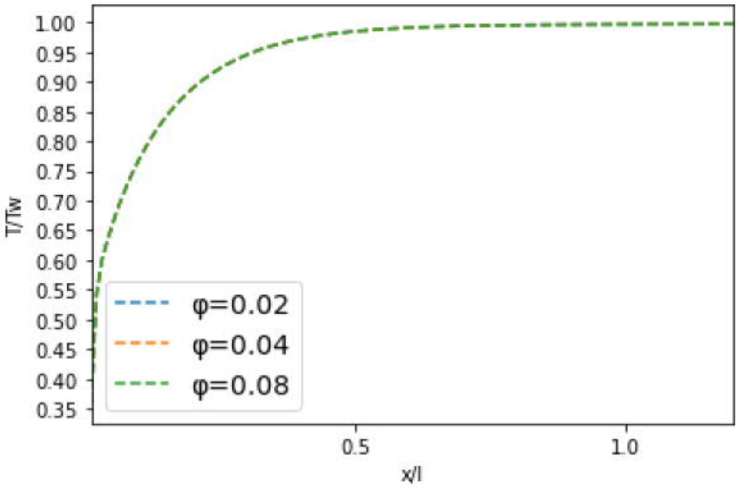

(c) for $Re = 20$ and $Kn = 0.02$

Figure 3.45: Temperature jump profiles in function of (a) Reynold number, (b) Knudsen number, and (c) nanoparticle volume fraction.

General Conclusion

The advancements in microsystem technology have been driven by multifaceted reasons, including its wide range of applications and efficient utilization of energy and materials. Additionally, the study of flows within microchannels has gained significant importance, driven by its fundamental scientific complexities and practical implications across various fields.

Microfluidics is a field that focuses on controlling flow and heat transfer in microchannels, where conventional no-slip boundary conditions are not applicable. Simulation of rarefied fluid flow is crucial for studying this phenomenon. Microchannels are popular due to their compact design and effective heat dissipation potential, which is essential for maintaining the quality and reliability of electronic devices. The use of gases and liquids as working fluids facilitates slip flow in microscopic devices.

The lattice Boltzmann method (LBM) is a computational approach for fluid dynamics, based on the Boltzmann transport equation and kinetic theory. Its kinetic nature provides advantages such as compatibility with parallel computation and ease in handling complex boundary conditions. LBM is particularly useful for addressing fluid flow and heat transfer challenges in micro-scale regimes. Researchers are refining its algorithm to simulate functional models and introducing new approaches to demonstrate its effectiveness in solving various issues.

This thesis numerically simulated rarefied flow and heat transfer using the thermal lattice Boltzmann method with a double distribution function and BGK approximation. At the microscale, the heightened impact of surface effects renders the traditional no-slip boundary condition inapplicable. Consequently, slip velocity and temperature jump are considered along fluid-solid interfaces, extending these effects to the obstacle level. A computer program was developed and evaluated using Python software throughout the study sections. The study consists of three sections, each focusing on different aspects of microchannel analysis. The first section investigates obstacles within microchannels, aiming to understand their impact on fluid flow characteristics and channel performance. The second section focuses on baffle placement within microchannel walls, identifying optimal locations for obstacles. The third section explores the thermophysical properties of fluids within microchannels, introducing nanofluids (copper and water) to improve the thermal conductivity coefficient and enhance heat transfer capabilities without altering channel geometry. The study explores the potential benefits of nanofluids in microchannels.

The first chapter explores the relationship between Micro-Electro-Mechanical Systems (MEMS) and heat transfer in microchannels, discussing techniques to improve heat transfer and the classification of rarefied flow. Also, the chapter explains the theoretical basis and governing equations of the Lattice Boltzmann Method (LBM), including boundary conditions. And presents a simulation workflow that connects rarefied flow and microchannels using the Thermal Lattice Boltzmann Model. Chapter 2 details the boundary conditions for investigation, algorithm construction, and results. Chapter 3 presents and discusses the findings. The thesis concludes with a summary of the findings and potential avenues for future research.

The study found that fluid in a microchannel configuration with nine obstacles exhibited decelerated motion and acceleration at the main outlet. It suggests strategically placing obstacles at the bottom or both sides to effectively reduce velocity. Two approaches were identified for achieving lower temperatures at the microchannel exit: implementing cooling measures on both sides or cooling only at the top, the latter resulting in reduced material consumption.

The study reveals that an increase in nanoparticle volume fraction leads to an increase in the Nusselt number, and that rarefaction and Reynolds numbers impact velocity and temperature. A higher rarefaction effect decreases both. The proposed configurations can enhance microchannel geometry and use microelectromechanical systems as advanced cooling techniques. These findings contribute to fluid dynamics and heat transfer, providing insights into rarefied flow and paving the way for further research. Based on the findings of this thesis, we propose several potential future research directions. Firstly, fluid flow and heat transfer in the current geometry could be enhanced by utilizing various shapes of obstacles within the microchannel. Secondly, further investigation into rarefied flow in the transition regime would be valuable. Additionally, exploring the use of multiple relaxation times instead of the BGK approximation for the collision operator could improve the study of thermal flow in the microchannel.

Bibliography

[1] Felix Sharipov. *Rarefied gas dynamics: fundamentals for research and practice*. John Wiley & Sons, 2015.

[2] Carlo Cercignani. *Slow rarefied flows: theory and application to micro-electro-mechanical systems*, volume 41. Springer Science & Business Media, 2006.

[3] Saeed J Almalowi, Alparslan Oztekin, et al. Flow simulations using two dimensional thermal lattice boltzmann method. *Journal of Applied Mathematics*, 2012, 2012.

[4] Ching Shen. *Rarefied gas dynamics: fundamentals, simulations and micro flows*. Springer Science & Business Media, 2006.

[5] Yudong Yuan and Sheik Rahman. Extended application of lattice boltzmann method to rarefied gas flow in micro-channels. *Physica A: Statistical Mechanics and its Applications*, 463:25–36, 2016.

[6] Sona Ghadirzadeh and Mohammad Kalteh. Lattice boltzmann simulation of temperature jump effect on the nanofluid heat transfer in an annulus microchannel. *International Journal of Mechanical Sciences*, 133:524–534, 2017.

[7] A Sohankar, A Joulaei, and M Mahmoodi. Fluid flow and convective heat transfer in a rotating rectangular microchannel with various aspect ratios. *International Journal of Thermal Sciences*, 172:107259, 2022.

[8] Yassine Kabar, Rachid Bessaïh, and Mourad Rebay. Conjugate heat transfer with rarefaction in parallel plates microchannel. *Superlattices and Microstructures*, 60:370–388, 2013.

[9] Dariush Bahrami, Salman Abbasian-Naghneh, Aliakbar Karimipour, and Arash Karimipour. Efficacy of injectable rib height on the heat transfer and entropy generation in

the microchannel by affecting slip flow. *Mathematical Methods in the Applied Sciences*, 2020.

[10] Alexander S Lobasov, Andrey V Minakov, and Valeri Y Rudyak. The investigation of the velocity slip and the temperature jump effect on the heat transfer characteristics in a microchannel. *Case Studies in Thermal Engineering*, 31:101791, 2022.

[11] Jie Gao, Zhuohuan Hu, Qiguo Yang, Xing Liang, and Hongwei Wu. Fluid flow and heat transfer in microchannel heat sinks: Modelling review and recent progress. *Thermal Science and Engineering Progress*, 29:101203, 2022.

[12] Zhipeng Duan, Hao Ma, Boshu He, Liangbin Su, and Xin Zhang. Pressure drop of microchannel plate fin heat sinks. *Micromachines*, 10(2):80, 2019.

[13] Jingtan Chen, Shakeel Ahmad, Wei Deng, Junjie Cai, and Jiyun Zhao. Micro/nanoscale surface on enhancing the microchannel flow boiling performance: A lattice boltzmann simulation. *Applied Thermal Engineering*, 205:118036, 2022.

[14] Davood Toghraie, Arash Karimipour, Mohammad Reza Safaei, Marjan Goodarzi, Habibollah Alipour, Mahidzal Dahari, et al. Investigation of rib's height effect on heat transfer and flow parameters of laminar water–al2o3 nanofluid in a rib-microchannelauthorname: Akbari, omid ali. *Applied Mathematics and Computation*, 290(C):135–153, 2016.

[15] M Kmiotek and A Kucaba-Piętal. Influence of slim obstacle geometry on the flow and heat transfer in microchannels. *Bulletin of the Polish Academy of Sciences: Technical Sciences*, (2), 2018.

[16] Zahra Abdelmalek, Annunziata D'Orazio, and Arash Karimipour. The effect of nanoparticle shape and microchannel geometry on fluid flow and heat transfer in a porous microchannel. *Symmetry*, 12(4):591, 2020.

[17] WA Khan, N Anjum, M Waqas, SZ Abbas, M Irfan, and Taseer Muhammad. Impact of stratification phenomena on a nonlinear radiative flow of sutterby nanofluid. *Journal of Materials Research and Technology*, 15:306–314, 2021.

[18] M Waqas, WA Khan, Amjad Ali Pasha, Nazrul Islam, and Mustafa Mutiur Rahman. Dynamics of bioconvective casson nanoliquid from a moving surface capturing gyrotactic microorganisms, magnetohydrodynamics and stratifications. *Thermal Science and Engineering Progress*, 36:101492, 2022.

[19] Waqar Azeem Khan. Dynamics of gyrotactic microorganisms for modified eyring powell nanofluid flow with bioconvection and nonlinear radiation aspects. *Waves in Random and Complex Media*, pages 1–11, 2023.

[20] Nazash Anjum, WA Khan, A Hobiny, M Azam, M Waqas, and M Irfan. Numerical analysis for thermal performance of modified eyring powell nanofluid flow subject to activation energy and bioconvection dynamic. *Case Studies in Thermal Engineering*, 39:102427, 2022.

[21] Baoli Shao, Shuyan Wang, Xi Chen, Lei Xie, and Lili Liu. Effect of surface structure on flow and heat transfer using lattice boltzmann method in a microchannel exchanger. *Applied Thermal Engineering*, 220:119787, 2023.

[22] WA Khan, A Ahmad, N Anjum, SZ Abbas, W Chammam, A Riahi, H Rebei, and M Zaway. Impact of nanoparticles and radiation phenomenon on viscoelastic fluid. *International Journal of Modern Physics B*, 36(05):2250049, 2022.

[23] Waqar Azeem Khan. Impact of time-dependent heat and mass transfer phenomenon for magnetized sutterby nanofluid flow. *Waves in random and complex media*, pages 1–15, 2022.

[24] Meng Wang, Phillip S Dobson, and Manosh C Paul. Numerical investigation of nanofluid deposition in a microchannel cooling system. *Powder Technology*, 425:118582, 2023.

[25] M Tabrez and Waqar Azeem Khan. Exploring physical aspects of viscous dissipation and magnetic dipole for ferromagnetic polymer nanofluid flow. *Waves in random and complex media*, pages 1–20, 2022.

[26] Z Hussain and Waqar Azeem Khan. Impact of thermal-solutal stratifications and activation energy aspects on time-dependent polymer nanoliquid. *Waves in random and complex media*, pages 1–11, 2022.

[27] WA Khan, Z Arshad, A Hobiny, S Saleem, A Al-Zubaidi, and M Irfan. Impact of magnetized radiative flow of sutterby nanofluid subjected to convectively heated wedge. *International Journal of Modern Physics B*, 36(16):2250079, 2022.

[28] Liangbin Su, Boshu He, Gang Wang, Renzheng Xiao, and Wan Yu. Simultaneously developing flow and heat transfer in circular and parallel-plates microchannels with veloc-

ity slip and temperature jump. *International Journal of Thermal Sciences*, 177:107590, 2022.

[29] Turgay Coskun and Erdal Cetkin. A review of heat and fluid flow characteristics in microchannel heat sinks. *Heat Transfer*, 49(8):4109–4133, 2020.

[30] Arash Karimipour, Alireza Hossein Nezhad, Annunziata D'Orazio, Mohammad Hemmat Esfe, Mohammad Reza Safaei, and Ebrahim Shirani. Simulation of copper–water nanofluid in a microchannel in slip flow regime using the lattice boltzmann method. *European Journal of Mechanics-B/Fluids*, 49:89–99, 2015.

[31] Lincheng Xu, Xu Yu, and Klaus Regenauer-Lieb. An immersed boundary-lattice boltzmann method for gaseous slip flow. *Physics of Fluids*, 32(1), 2020.

[32] Mojtaba Balaj, Ehsan Roohi, and Alireza Mohammadzadeh. Regulation of anti-fourier heat transfer for non-equilibrium gas flows through micro/nanochannels. *International Journal of Thermal Sciences*, 118:24–39, 2017.

[33] C Shu, XD Niu, and YT Chew. A lattice boltzmann kinetic model for microflow and heat transfer. *Journal of statistical physics*, 121:239–255, 2005.

[34] Ehsan Kamali Ahangar, Mohammad Bagher Ayani, and Javad Abolfazli Esfahani. Simulation of rarefied gas flow in a microchannel with backward facing step by two relaxation times using lattice boltzmann method–slip and transient flow regimes. *International Journal of Mechanical Sciences*, 157:802–815, 2019.

[35] Frederik Verhaeghe, Li-Shi Luo, and Bart Blanpain. Lattice boltzmann modeling of microchannel flow in slip flow regime. *Journal of Computational Physics*, 228(1):147–157, 2009.

[36] Xuewen Yin and Junfeng Zhang. An improved bounce-back scheme for complex boundary conditions in lattice boltzmann method. *Journal of Computational Physics*, 231(11):4295–4303, 2012.

[37] Kai Wang, Zhenhua Chai, Guoxiang Hou, Wei Chen, and Sheng Xu. Slip boundary condition for lattice boltzmann modeling of liquid flows. *Computers & Fluids*, 161:60–73, 2018.

[38] Alireza Shahriari, Hamid Reza Ashorynejad, and Ioan Pop. Entropy generation of mhd nanofluid inside an inclined wavy cavity by lattice boltzmann method. *Journal of Thermal Analysis and Calorimetry*, 135:283–303, 2019.

[39] Yanhong Liu. A lattice boltzmann model for blood flows. *Applied Mathematical Modelling*, 36(7):2890–2899, 2012.

[40] Yingchun Zhang, Gongnan Xie, and Arash Karimipour. Comprehensive analysis on the effect of asymmetric heat fluxes on microchannel slip flow and heat transfer via a lattice boltzmann method. *International Communications in Heat and Mass Transfer*, 118:104856, 2020.

[41] Mahdi Abaszadeh, Ali Safavinejad, Hossein Amiri, and Amin Amiri Delouei. A direct-forcing ib-lbm implementation for thermal radiation in irregular geometries. *Journal of Thermal Analysis and Calorimetry*, 147(20):11169–11181, 2022.

[42] Like Li, Renwei Mei, and James F Klausner. Boundary conditions for thermal lattice boltzmann equation method. *Journal of Computational Physics*, 237:366–395, 2013.

[43] Chyung Ay, Chao-Wang Young, and Chuen-Fu Young. Application of lattice boltzmann method to the fluid analysis in a rectangular microchannel. *Computers & Mathematics with Applications*, 64(5):1065–1083, 2012.

[44] Shi Tao, Liang Wang, Qing He, Jiechao Chen, and Jiahong Luo. Lattice boltzmann simulation of complex thermal flows via a simplified immersed boundary method. *Journal of Computational Science*, 65:101878, 2022.

[45] Hamid Hassanzadeh Afrouzi, Majid Ahmadian, Mirollah Hosseini, Hossein Arasteh, Davood Toghraie, and Sara Rostami. Simulation of blood flow in arteries with aneurysm: Lattice boltzmann approach (lbm). *Computer methods and programs in biomedicine*, 187:105312, 2020.

[46] Masoud Mozaffari, Annunziata D'Orazio, Arash Karimipour, Ali Abdollahi, and Mohammad Reza Safaei. Lattice boltzmann method to simulate convection heat transfer in a microchannel under heat flux: gravity and inclination angle on slip-velocity. *International Journal of Numerical Methods for Heat & Fluid Flow*, 30(6):3371–3398, 2020.

[47] Liuming Yang, Yang Yu, Huijie Pei, Yuan Gao, and Guoxiang Hou. Lattice boltzmann simulations of liquid flows in microchannel with an improved slip boundary condition. *Chemical Engineering Science*, 202:105–117, 2019.

[48] Bappa Mondal, Sumit Kumar Mehta, Sukumar Pati, and Promod Kumar Patowari. Numerical analysis of electroosmotic mixing in a heterogeneous charged micromixer with obstacles. *Chemical Engineering and Processing-Process Intensification*, 168:108585, 2021.

[49] S Rahbarshahlan, E Esmaeilzadeh, Alireza Rostamzadeh Khosroshahi, and A Ghaffarzadeh Bakhshayesh. Numerical simulation of fluid flow and heat transfer in microchannels with patterns of hydrophobic/hydrophilic walls. *The European Physical Journal Plus*, 135(2):157, 2020.

[50] Arsalan Taassob, Reza Kamali, and Alireza Bordbar. Investigation of rarefied gas flow through bended microchannels. *Vacuum*, 151:197–204, 2018.

[51] Ali Amiri-Jaghargh, Ehsan Roohi, Hamid Niazmand, and Stefan Stefanov. Dsmc simulation of low knudsen micro/nanoflows using small number of particles per cells. *Journal of Heat Transfer*, 135(10):101008, 2013.

[52] Ehsan Roohi and Masoud Darbandi. Recommendations on performance of parallel dsmc algorithm in solving subsonic nanoflows. *Applied Mathematical Modelling*, 36(5):2314–2321, 2012.

[53] Annunziata D'Orazio and Arash Karimipour. A useful case study to develop lattice boltzmann method performance: gravity effects on slip velocity and temperature profiles of an air flow inside a microchannel under a constant heat flux boundary condition. *International Journal of Heat and Mass Transfer*, 136:1017–1029, 2019.

[54] Cristina Chircov and Alexandru Mihai Grumezescu. Microelectromechanical systems (mems) for biomedical applications. *Micromachines*, 13(2):164, 2022.

[55] Hussam Sadique, Qasim Murtaza, et al. Heat transfer augmentation in microchannel heat sink using secondary flows: A review. *International Journal of Heat and Mass Transfer*, 194:123063, 2022.

[56] Fei Li, Qingming Ma, Gongming Xin, Jingchao Zhang, and Xinyu Wang. Heat transfer and flow characteristics of microchannels with solid and porous ribs. *Applied Thermal Engineering*, 178:115639, 2020.

[57] Ngoctan Tran, Yaw-Jen Chang, and Chi-Chuan Wang. Optimization of thermal performance of multi-nozzle trapezoidal microchannel heat sinks by using nanofluids of al2o3 and tio2. *International Journal of Heat and Mass Transfer*, 117:787–798, 2018.

[58] Hao Ma, Zhipeng Duan, Xiaoru Ning, and Liangbin Su. Numerical investigation on heat transfer behavior of thermally developing flow inside rectangular microchannels. *Case Studies in Thermal Engineering*, 24:100856, 2021.

[59] Lin Liu, Ziyong Cao, Chao Xu, Ling Zhang, and Te Sun. Investigation of fluid flow and heat transfer characteristics in a microchannel heat sink with double-layered staggered cavities. *International Journal of Heat and Mass Transfer*, 187:122535, 2022.

[60] V Murali Krishna, M Sandeep Kumar, R Muthalagu, P Senthil Kumar, and R Mounika. Numerical study of fluid flow and heat transfer for flow of cu-al2o3-water hybrid nanofluid in a microchannel heat sink. *Materials Today: Proceedings*, 49:1298–1302, 2022.

[61] Wan Mohd Arif Aziz Japar, Nor Azwadi Che Sidik, Rahman Saidur, Yutaka Asako, and Siti Nurul Akmal Yusof. A review of passive methods in microchannel heat sink application through advanced geometric structure and nanofluids: Current advancements and challenges. *Nanotechnology Reviews*, 9(1):1192–1216, 2020.

[62] Li Sun, Juan Li, Hao Xu, Jie Ma, and Hao Peng. Numerical study on heat transfer and flow characteristics of novel microchannel heat sinks. *International Journal of Thermal Sciences*, 176:107535, 2022.

[63] Rasul Mohebbi, Hassan Lakzayi, Nor Azwadi Che Sidik, and Wan Mohd Arif Aziz Japar. Lattice boltzmann method based study of the heat transfer augmentation associated with cu/water nanofluid in a channel with surface mounted blocks. *International Journal of Heat and Mass Transfer*, 117:425–435, 2018.

[64] Baoli Shao, Shuyan Wang, Xi Chen, Lei Xie, and Lili Liu. Effect of surface structure on flow and heat transfer using lattice boltzmann method in a microchannel exchanger. *Applied Thermal Engineering*, 220:119787, 2023.

[65] Nilankush Acharya. Buoyancy driven magnetohydrodynamic hybrid nanofluid flow within a circular enclosure fitted with fins. *International Communications in Heat and Mass Transfer*, 133:105980, 2022.

[66] Mokhtar Ferhi and RIDHA Djebali. Heat transfer appraising and second law analysis of cu-water nanoliquid filled microchannel: Slip flow regime. *Romanian Journal of Physics*, 67:605, 2022.

[67] Rahouadja Zarita and Madjid Hachemi. Numerical investigation and analysis of heat transfer enhancement in a microchannel using nanofluids by the lattice boltzmann method. *Frontiers in Heat and Mass Transfer (FHMT)*, 12, 2018.

[68] Hudong Chen, Satheesh Kandasamy, Steven Orszag, Rick Shock, Sauro Succi, and Victor Yakhot. Extended boltzmann kinetic equation for turbulent flows. *Science*, 301(5633):633–636, 2003.

[69] Ehsan Kamali Ahangar, Morteza Izanlu, Masoud Jabbari, Goodarz Ahmadi, and Aliakbar Karimipour. Thermal microscale gas flow simulation using wall function and bounce-back scheme: Modified lattice boltzmann method. *International Communications in Heat and Mass Transfer*, 119:104993, 2020.

[70] Xiuliang Liu and Zhaoli Guo. A lattice boltzmann study of gas flows in a long microchannel. *Computers & Mathematics with Applications*, 65(2):186–193, 2013.

[71] Chia Hung Wang and Ru Yang. A numerical study for slip flow heat transfer. *Applied mathematics and computation*, 173(2):1246–1264, 2006.

[72] Khair Eddine ZAHOUANI et al. Etude de la convection de rayleigh bénard par la méthode lattice boltzman. 2017.

[73] Y Liu, J Cui, YX Jiang, and WZ Li. A numerical study on heat transfer performance of microchannels with different surface microstructures. *Applied Thermal Engineering*, 31(5):921–931, 2011.

[74] Leila Jahanshaloo, Nor Azwadi Che Sidik, Alireza Fazeli, and Mahmoud Pesaran HA. An overview of boundary implementation in lattice boltzmann method for computational heat and mass transfer. *International Communications in Heat and Mass Transfer*, 78:1–12, 2016.

[75] D Arumuga Perumal and Anoop K Dass. A review on the development of lattice boltzmann computation of macro fluid flows and heat transfer. *Alexandria Engineering Journal*, 54(4):955–971, 2015.

[76] Pierre Lallemand, Li-shi Luo, Manfred Krafczyk, and Wen-An Yong. The lattice boltzmann method for nearly incompressible flows. *Journal of Computational Physics*, 431:109713, 2021.

[77] Zhaoli Guo and Chang Shu. *Lattice Boltzmann method and its application in engineering*, volume 3. World Scientific, 2013.

[78] Sauro Succi. *The lattice Boltzmann equation: for fluid dynamics and beyond.* Oxford university press, 2001.

[79] Cha'o-Kuang Chen, Shing-Cheng Chang, Szu-Yu Sun, et al. Lattice boltzmann method simulation of channel flow with square pillars inside by the field synergy principle. *Computer Modeling in Engineering and Sciences*, 22(3):203–215, 2007.

[80] AA Mohamad and AA Mohamad. The boltzmann equation. *Lattice Boltzmann Method: Fundamentals and Engineering Applications with Computer Codes*, pages 25–39, 2019.

[81] Timm Krüger, Halim Kusumaatmaja, Alexandr Kuzmin, Orest Shardt, Goncalo Silva, and Erlend Magnus Viggen. The lattice boltzmann method. *Springer International Publishing*, 10(978-3):4–15, 2017.

[82] Runa Samanta, Himadri Chattopadhyay, and Chandan Guha. A review on the application of lattice boltzmann method for melting and solidification problems. *Computational Materials Science*, 206:111288, 2022.

[83] Yue-Hong Qian, Dominique d'Humières, and Pierre Lallemand. Lattice bgk models for navier-stokes equation. *Europhysics letters*, 17(6):479, 1992.

[84] Rasul Mohebbi, Amin Amiri Delouei, Amin Jamali, Mohsen Izadi, and Abdulmajeed A Mohamad. Pore-scale simulation of non-newtonian power-law fluid flow and forced convection in partially porous media: thermal lattice boltzmann method. *Physica A: Statistical Mechanics and Its Applications*, 525:642–656, 2019.

[85] Nicolas Delbosc. *Real-time simulation of indoor air flow using the lattice boltzmann method on graphics processing unit.* PhD thesis, University of Leeds, 2015.

[86] Albert Puig Arànega et al. Review of boundary conditions and investigation towards the development of a growth model: a lattice boltzmann method approach. 2016.

[87] AA Mohamad and AA Mohamad. Multi-relaxation schemes. *Lattice Boltzmann Method: Fundamentals and Engineering Applications with Computer Codes*, pages 145–149, 2019.

[88] CY Lim, C Shu, XD Niu, and YT Chew. Application of lattice boltzmann method to simulate microchannel flows. *Physics of fluids*, 14(7):2299–2308, 2002.

[89] Jun Cai, Xiulan Huai, Bin Liu, and Zhendong Cui. Numerical prediction of thin liquid film near the solid wall for hydraulic cavitating flow in microchannel by a multiphase lattice boltzmann model. *International Journal of Heat and Mass Transfer*, 127:107–115, 2018.

[90] AA Mohamad. The diffusion equation. In *Lattice Boltzmann Method: Fundamentals and Engineering Applications with Computer Codes*, pages 53–80. Springer, 2019.

[91] Zhi-Wei Tian, Chun Zou, Hong-Juan Liu, Zhao-Li Guo, Zhao-Hui Liu, and Chu-Guang Zheng. Lattice boltzmann scheme for simulating thermal micro-flow. *Physica A: Statistical Mechanics and its Applications*, 385(1):59–68, 2007.

[92] Sheng Chen and Zhiwei Tian. Simulation of thermal micro-flow using lattice boltzmann method with langmuir slip model. *International journal of heat and fluid flow*, 31(2):227–235, 2010.

[93] H Shokouhmand and AH Meghdadi Isfahani. An improved thermal lattice boltzmann model for rarefied gas flows in wide range of knudsen number. *International communications in heat and mass transfer*, 38(10):1463–1469, 2011.

[94] XD Niu, C Shu, and YT Chew. A thermal lattice boltzmann model with diffuse scattering boundary condition for micro thermal flows. *Computers & Fluids*, 36(2):273–281, 2007.

[95] Amine Abdellah-El-Hadj. *Lattice Boltzmann Method for Fluid Flow*. PhD thesis, UC Irvine, 2014.

[96] Xiaoyi He, Shiyi Chen, and Gary D Doolen. A novel thermal model for the lattice boltzmann method in incompressible limit. *Journal of computational physics*, 146(1):282–300, 1998.

[97] Sıtkı Berat Çelik. Analysis of single phase fluid flow and heat transfer in slip flow regime by parallel implementation of lattice boltzmann method on gpus. Master's thesis, Middle East Technical University, 2012.

[98] Keerti Vardhan Sharma, Robert Straka, and Frederico Wanderley Tavares. Current status of lattice boltzmann methods applied to aerodynamic, aeroacoustic, and thermal flows. *Progress in Aerospace Sciences*, 115:100616, 2020.

[99] Nishanth Dongari, Ashutosh Sharma, and Franz Durst. Pressure-driven diffusive gas flows in micro-channels: from the knudsen to the continuum regimes. *Microfluidics and nanofluidics*, 6:679–692, 2009.

[100] Alexander S Lobasov, Andrey V Minakov, and Valeri Y Rudyak. The investigation of the velocity slip and the temperature jump effect on the heat transfer characteristics in a microchannel. *Case Studies in Thermal Engineering*, 31:101791, 2022.

[101] Arash Karimipour. New correlation for nusselt number of nanofluid with ag/al2o3/cu nanoparticles in a microchannel considering slip velocity and temperature jump by using lattice boltzmann method. *International Journal of Thermal Sciences*, 91:146–156, 2015.

[102] Huijin Xu, Changying Zhao, and Kambiz Vafai. Analysis of double slip model for a partially filled porous microchannel—an exact solution. *European Journal of Mechanics-B/Fluids*, 68:1–9, 2018.

[103] Shujit Kumar Bala, Litan Kumar Saha, and M Anwar Hossain. Simulation of forced convection in a channel containing three obstacles over backward and forward facing steps by lbm. *International Journal of Applied and Computational Mathematics*, 5:1–19, 2019.

[104] Qifeng Zhu, Yangyang Jin, Junjie Chen, Ruirui Su, Feiyue Zhu, Haixia Li, Jianfeng Wan, Hongwei Zhang, Haolei Sun, Yang Cui, et al. Computational study of rib shape and configuration for heat transfer and fluid flow characteristics of microchannel heat sinks with fan-shaped cavities. *Applied Thermal Engineering*, 195:117171, 2021.

[105] Kourosh Javaherdeh, Habib Karimi, and Touraj Azarbarzin. Lattice boltzmann simulation of fluid flow and heat transfer in a micro channel with heat sources located on the walls. *Superlattices and Microstructures*, 160:107069, 2021.

[106] Shams-Ul Islam, Naqib Ullah, and Chao Ying Zhou. Numerical analysis of blockage effects on the flow between parallel plates by using lattice boltzmann method. *Canadian Journal of Physics*, 99(6):399–411, 2021.

[107] Lei Zhang, V Puneeth, Muhammad Ijaz Khan, Essam Roshdy El-Zahar, N Manjunath, Nehad Ali Shah, Jae Dong Chung, Sami Ullah Khan, and M Imran Khan. Applications of bioconvection for tiny particles due to two concentric cylinders when role of lorentz force is significant. *Plos one*, 17(5):e0265026, 2022.

[108] Javad Rostami. Optimization of convective heat transfer in microchannels equipped by porous ribs. *Transport in Porous Media*, 141(2):439–468, 2022.

[109] Chun-Sheng Wang, Po-Yi Shen, and Tong-Miin Liou. Evaluation of porous rib and flow pulsation on microchannel thermal performance using a novel thermal lattice boltzmann method. *International Journal of Thermal Sciences*, 172:107345, 2022.

[110] Mohammad Shamsoddini Lori and Kambiz Vafai. Heat transfer and fluid flow analysis of microchannel heat sinks with periodic vertical porous ribs. *Applied Thermal Engineering*, 205:118059, 2022.

[111] Siham Hammid, Khatir Naima, Younes Menni, Cheikh Kezrane, Abdelkrim Liazid, Ayad Qasim Al-Dujaili, Ahmed Ibraheem Abdulkareem, Amjad Jaleel Humaidi, and Sarah Jawad Shoja. Advanced numerical analysis of convective rarefied flows in microchannels: Studying the impact of multiple obstacle arrangements through lbm modeling. *Modern Physics Letters B*, 37(27):2350099, 2023.

[112] Qisu Zou and Xiaoyi He. On pressure and velocity boundary conditions for the lattice boltzmann bgk model. *Physics of fluids*, 9(6):1591–1598, 1997.

[113] AA Mohamad and AA Mohamad. Isothermal incompressible fluid flow. *Lattice Boltzmann Method: Fundamentals and Engineering Applications with Computer Codes*, pages 105–131, 2019.

[114] Siham Hammid, Khatir Naima, Omolayo M Ikumapayi, Cheikh Kezrane, Abdelkrim Liazid, Jihad Asad, Mokdad Hayawi Rahman, Farhan Lafta Rashid, Naseer Ali Hussien, and Younes Menni. Overall assessment of heat transfer for a rarefied flow in a microchannel with obstacles using lattice boltzmann method. *Comput. Model. Eng. Sci*, 138:273–299, 2024.

[115] AA Mohamad and AA Mohamad. Similarities and scaling. *Lattice Boltzmann Method: Fundamentals and Engineering Applications with Computer Codes*, pages 41–45, 2019.

[116] Siham Hammid, Khatir Naima, Sultan Alqahtani, Sultan Alshehery, Khulood H Oudah, Omolayo M Ikumapayi, and Younes Menni. Laminar rarefied flow analysis in a microchannel with h2o-cu nanofluid: A thermal lattice boltzmann study. *Modern Physics Letters B*, 38(03):2450006, 2024.

[117] W Yu and SUS Choi. The role of interfacial layers in the enhanced thermal conductivity of nanofluids: a renovated maxwell model. *Journal of nanoparticle research*, 5:167–171, 2003.

[118] Mohammad Reza Safaei, Marjan Gooarzi, Omid Ali Akbari, Mostafa Safdari Shadloo, and Mahidzal Dahari. Performance evaluation of nanofluids in an inclined ribbed microchannel for electronic cooling applications. *Electronics cooling*, 832, 2016.

[119] Ehsan Roohi and Masoud Darbandi. Extending the navier–stokes solutions to transition regime in two-dimensional micro-and nanochannel flows using information preservation scheme. *Physics of fluids*, 21(8), 2009.

[120] Kourosh Javaherdeh, Habib Karimi, and Touraj Azarbarzin. Lattice boltzmann simulation of fluid flow and heat transfer in a micro channel with heat sources located on the walls. *Superlattices and Microstructures*, 160:107069, 2021.

Appendix A

Appendix A

A.1 Flow boundary conditions

The input velocity is known for the inlet boundary condition, but the density is unknown and necessitates determination. Zou and He correlations can be utilized to assess inlet density and unknown distribution functions. The unknown distribution functions on the left boundary of MC and the density can be expressed as [67, 112]:

$$\begin{aligned}
\rho_{in} &= \frac{1}{(1-u_{in})}\left[f_0+f_2+f_4+2\left(f_3+f_6+f_7\right)\right] \\
f_1 &= f_3+\frac{2}{3}\rho_{in}u_{in} \\
f_5 &= f_7-\frac{1}{2}\left(f_2-f_4\right)+\frac{1}{6}\rho_{in}u_{in} \\
f_8 &= f_6-\frac{1}{2}\left(f_4-f_2\right)+\frac{1}{6}\rho_{in}u_{in}
\end{aligned} \tag{A.1}$$

The outlet velocity is unknown. Extrapolation is commonly used to calculate unknown distribution functions at the east boundary, as illustrated by the equations below [113, 114] :

$$\begin{aligned}
f_{3,n} &= 2\cdot f_{3,n-1}-f_{3,n-2} \\
f_{6,n} &= 2\cdot f_{6,n-1}-f_{6,n-2} \\
f_{7,n} &= 2\cdot f_{7,n-1}-f_{7,n-2}
\end{aligned} \tag{A.2}$$

In the slip flow regime, the fluid velocity near the wall differs from the wall velocity. The slip boundary condition for a bottom wall is given as follows [6]:

$$\begin{aligned}
\rho_w &= [f_0 + f_1 + f_3 + 2(f_7 + f_4 + f_8)] \\
f_2 &= f_4 \\
f_5 &= \frac{\rho_w(1 + u_x) - f_0 + f_2 + f_4}{2} - (f_1 + f_8) \\
f_6 &= \frac{\rho_w(1 - u_x) - f_0 + f_2 + f_4}{2} - (f_3 + f_7) \\
u_x &= \frac{kn\,(4u_{x,1} - u_{x,2})}{2 + 3kn}
\end{aligned} \tag{A.3}$$

Where $u_{x,1}, u_{x,2}$ are the velocities of the initial two network nodes following the fluid's speed on MC's wall [101].

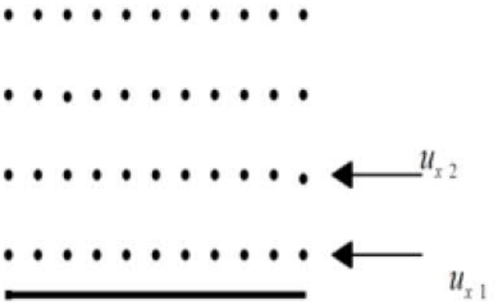

Figure A.1: Rows of velocities

Similarly, for the top wall, it is possible to write:

$$\begin{aligned}
\rho_w &= f_0 + f_1 + f_3 + 2(f_2 + f_5 + f_6) \\
f_4 &= f_2 \\
f_7 &= \frac{\rho_w(1 - u_x) - (f_0 + f_2 + f_4)}{2} - (f_3 + f_6) \\
f_8 &= \frac{\rho_w(1 + u_x) - (f_0 + f_2 + f_4)}{2} - (f_1 + f_5) \\
u_x &= \frac{kn\,(4u_{x,H-1} - u_{x,H-2})}{2 + 3kn}
\end{aligned} \tag{A.4}$$

A.2 Temperature boundary conditions

The inlet temperature distribution function are given as [67]:

$$\begin{aligned} g_1 &= \frac{1}{9}T_{in}(3+6u_x^2) - g_3 \\ g_5 &= \frac{1}{36}T_{in}(6+6u_x^2) - g_7 \\ g_8 &= \frac{1}{36}T_{in}(6+6u_x^2) - g_6 \end{aligned} \tag{A.5}$$

The outlet temperature boundary condition can be determined by employing an extrapolation method [113, 114]:

$$\begin{aligned} g_{3,n} &= 2 \cdot g_{3,n-1} - g_{3,n-2} \\ g_{6,n} &= 2 \cdot g_{6,n-1} - g_{6,n-2} \\ g_{7,n} &= 2 \cdot g_{7,n-1} - g_{7,n-2} \end{aligned} \tag{A.6}$$

For a top wall, the equations of temperature jump are given as below [67]:

$$\begin{aligned} T_{y=H} &= \frac{C_{\text{jump}}\left(4T_{H-1} - T_{H-2}\right) + 2T_w}{\left(2 + 3C_{\text{jump}}\right)} \\ g_4 &= 1.5T_{y=H}(\omega(2)+\omega(4)) - g_2 \\ g_7 &= 3T_{y=H}(\omega(5)+\omega(7)) - g_5 \\ g_8 &= 3T_{y=H}(\omega(6)+\omega(8)) - g_6 \end{aligned} \tag{A.7}$$

For the bottom wall, the following temperature jump equations are applicable [67]:

$$\begin{aligned} T_{y=0} &= \frac{C_{\text{jump}}\left(4T_1 - T_2\right) + 2T_w}{\left(2 + 3C_{\text{jump}}\right)} \\ g_2 &= 1.5T_{y=0}(\omega(2)+\omega(4)) - g_4 \\ g_5 &= 3T_{y=0}(\omega(5)+\omega(7)) - g_7 \\ g_6 &= 3T_{y=0}(\omega(6)+\omega(8)) - g_8 \end{aligned} \tag{A.8}$$

Where C_jump indicated the temperature jump coefficient and defined as :

$$C_{\text{jump}} = B\lambda = \phi\left(\frac{2\gamma}{(\gamma+1)P_r}\right)\lambda = BKnH \tag{A.9}$$